Photoinduced processes in hybrid perovskite for optoelectronics

Valentin Ianis Emmanuel QUELOZ

Abstract

Hybrids organic-inorganic perovskite(HOP) solar cells have unequivocally the potential for being a new generation of solar panels with a lower cost and a greater efficiency than well-known silicon solar panels. Today, even if HOPs are seen as one of the best ways to overcome climate change, they still have drawbacks to overcome, such as limited stability, especially in humid conditions. The more stable 2D perovskites, a low-dimension subfamily of the HOP is a good candidate to protect the 3D HOP while keeping a good efficiency. The understanding of the interaction between the 2D and the 3D perovskite is crucial to push the HOP cell toward the next step.

Chapter 2 introduces the state-of-the-art methods used throughout the work presented. Those optical techniques, steady state and time resolve, make it possible to reveal the intimate photophysics of new materials and interfaces.

Chapter 3 continues with an in-depth study of different 2D perovskites containing heavily fluorinated cations for an improve water repellent property. These cations show a large tunability of optical and dielectric properties according to their structure. We show that despite no direct contribution to the electronic structure, the cation size does have a large indirect influence. 2D perovskites made with longer cations show a smaller bandgap and exciton binding energy. This phenomenon comes from the strains induced by the cation in the perovskite structure and thus the orbital overlap, yielding a larger dispersion and a red shift of the bandgap. Finally, we demonstrated the excellent water stability of the different material with samples being stable for more than one month in ambient

conditions. To follow, we have focused on one cation named A43. The $(A43)_2PbI_4$ perovskite was extensively studied by means of ultrafast spectroscopy and electro-absorption, revealing the presence of long-lasting correlated electron–hole pairs. Such states have a marked charge- transfer character, as revealed by the persistent Stark effect in the form of a second derivative in electro-absorption. This effect is the result of the unique fluorinated cation electrostatic effect as well as the steric hindrance of the later. The stark effect in $(A43)_2PbI_2$ perovskite is at the core of this chapter and of this thesis.

After studying the 2D perovskite alone, chapter 4 describes the photophysics of the merged interface of the 2D and 3D perovskites in a bilayer system. Combining these two materials yields an improved performance of perovskite solar cells thanks to the synergistic properties of the 2D, more stable, and 3D perovskite, more efficient. However the interface was not well characterized. The crystal growth of the 2D layer as well as the carrier transfer properties between the 2D and 3D perovskite are still open questions. In this work, we reveal the impact of 2D/3D crystal alignment in driving interface charge-recombination dynamics. The 2D crystal growth and orientation are manipulated by specific fluorination of phenethylammonium (PEA), used here as the organic cation backbone of the 2D component. By means of time-resolved optoelectronic analysis from the femto- to microsecond regions, we demonstrate a static function of the 2D layer as an electron barrier and homogeneous surface passivant, together with a dynamic role in retarding back charge recombination. Our results reveal a crucial dependence of such beneficial effects with the 2D layer, leading to an enhanced open-circuit voltage (Voc), mostly attributed to the 2D phase which orients parallel to the 3D layer.

In addition, we studied the long-term evolution of the interface and the effect on a device. We revealed that the small cation from the 3D layer can migrate to the 2D top layer and altering its structure over time. By playing with the 2D perovskite material, we show that this migration can be blocked improving the cell lifetime.

Lastly, we studied the thermal stress on the 2D-3D interface in cells, knowing that it is one of the factors in the cell instability. Using X-ray scattering and by thermally

cycling the cells, we revealed that the 2D perovskite crystal layer undergoes a structural transformation toward a higher dimensionality. At the same time, it protects the 3D layer underneath as it does not show any changes. Indeed, the lead iodide leakage, the cause of the 3D perovskite degradation, is blocked by the top 2D layer. Such findings provide a deep understanding and delineate precise guidelines for the smart design of multidimensional perovskite interfaces for advanced PVs and beyond.

Finally, chapter 5 explores the excited state dynamics of MoS_2, a member of the 2D layer transition metal dichalcogenides(TMDC), very similar in structure to the 2D perovskite. MoS_2 has been explored as an HTM for perovskite cell as well as a buffer layer between the HTM and the perovskite layer for an improved stability. The excited state of MoS_2 is already well studied, but only until a few nanoseconds. Free carrier dynamics, living much longer than a few nanoseconds, is crucial for using this material in the previously mentioned role, were not studied so far. We have uncovered the entire excited state dynamics, from picoseconds up to the complete decay of carriers 10 microseconds later. This enables the smart use of this material in application where the free carrier dominates.

Keywords

Photovoltaic, perovskite, solar cells, spectroscopy, 2D perovskite, interface, 2D/3D, bilayer, low-dimensional, characterisation, optical,excited state,MoS_2, stability

Resumé

Les cellules solaires hybrides pérovskite organique-inorganique (HOP) ont sans conteste le potentiel d'être une nouvelle génération de panneaux solaires avec un coût inférieur et un rendement supérieur aux panneaux solaires en silicium bien connus. Aujourd'hui, même si les HOP sont considérées comme l'un des meilleurs moyens de lutter contre le changement climatique, elles présentent encore des inconvénients à surmonter, comme une stabilité limitée, notamment dans des conditions humides. Les pérovskites 2D, plus stables, une sous-famille de faible dimension des HOP, sont un bon candidat pour protéger les HOP 3D tout en conservant une bonne efficacité. La compréhension de l'interaction entre les pérovskites 2D et 3D est cruciale pour faire avancer la cellule HOP vers la prochaine étape.

Le chapitre 2 présente les méthodes de pointe utilisées tout au long du travail présenté. Ces techniques optiques, en régime permanent et à résolution temporelle, permettent de révéler la photophysique intime de nouveaux matériaux et interfaces.

Le chapitre 3 continue avec une étude approfondie de différentes perovskites 2D contenant des cations fortement fluorés pour améliorer la propriété hydrofuge. Ces cations montrent une grande accordabilité des propriétés optiques et diélectriques en fonction de leur structure. Nous montrons que malgré l'absence de contribution directe à la structure électronique, la taille du cation a une grande influence indirecte. Les pérovskites 2D fabriquées avec des cations plus longs montrent une bande interdite et une énergie de liaison des excitons plus petites. Ce phénomène provient des contraintes induites par le cation

dans la structure de la pérovskite et donc du recouvrement des orbitales, ce qui entraîne une plus grande dispersion et un décalage vers le rouge de la bande interdite. Enfin, nous avons démontré l'excellente stabilité à l'eau des différents matériaux, les échantillons étant stables pendant plus d'un mois dans des conditions ambiantes. Pour la suite, nous nous sommes concentrés sur un cation nommé A43. La pérovskite $(A43)_2PbI_2$ a été étudiée de manière approfondie par spectroscopie ultrarapide et électro-absorption, révélant la présence de paires électron-trou corrélées de longue durée. Ces états ont un caractère de transfert de charge marqué, comme le révèle l'effet Stark persistant sous la forme d'une dérivée seconde en électro-absorption. Cet effet est le résultat de l'effet électrostatique unique du cation fluoré ainsi que de l'encombrement stérique de ce dernier. L'effet Stark dans la pérovskite $(A43)_2PbI_2$ est au coeur de ce chapitre et de cette thèse.

Après avoir étudié la pérovskite 2D seule, le chapitre 4 décrit la photophysique de l'interface fusionnée des pérovskites 2D et 3D dans un système bicouche. La combinaison de ces deux matériaux permet d'améliorer les performances des cellules solaires à pérovskite grâce aux propriétés synergiques de la pérovskite 2D, plus stable, et de la pérovskite 3D, plus efficace. Cependant, l'interface n'a pas été bien caractérisée. La croissance cristalline de la couche 2D ainsi que les propriétés de transfert des porteurs entre la pérovskite 2D et 3D restent des questions ouvertes. Dans ce travail, nous révélons l'impact de l'alignement cristallin 2D/3D sur la dynamique de recombinaison des charges à l'interface. La croissance et l'orientation des cristaux 2D sont manipulées par une fluoration spécifique du phénéthylammonium (PEA), utilisé ici comme squelette cationique organique du composant 2D. Au moyen d'une analyse optoélectronique résolue dans le temps, de la femto- à la microseconde, nous démontrons une fonction statique de la couche 2D comme barrière électronique et passivant de surface homogène, ainsi qu'un rôle dynamique dans le retardement de la recombinaison de la charge arrière. Nos résultats révèlent une dépendance cruciale de ces effets bénéfiques avec la couche 2D, conduisant à une tension en circuit ouvert (Voc) améliorée, principalement attribuée à la phase 2D qui s'oriente parallèlement à la couche 3D.

De plus, nous avons étudié l'évolution à long terme de l'interface et son effet sur un dispositif. Nous avons révélé que le petit cation de la couche 3D peut migrer vers la couche supérieure 2D et modifier sa structure au fil du temps. En jouant avec le matériau pérovskite 2D, nous montrons que cette migration peut être bloquée améliorant ainsi la durée de vie de la cellule.

Enfin, nous avons étudié le stress thermique sur les cellules 2D-3D, sachant qu'il est l'un des facteurs de l'instabilité de la cellule. En utilisant la diffusion des rayons X et en effectuant un cycle thermique des cellules, nous avons révélé que la couche cristalline de pérovskite 2D subit une transformation structurelle vers une dimension supérieure. En même temps, elle protège la couche 3D située en dessous car elle ne présente aucune modification. En effet, la fuite d'iodure de plomb, cause de la dégradation de la pérovskite 3D, est bloquée par la couche 2D supérieure. Ces résultats permettent de mieux comprendre et de définir des lignes directrices précises pour la conception intelligente d'interfaces multidimensionnelles en pérovskite pour les systèmes photovoltaïques avancés et au-delà.

Enfin, le chapitre 5 explore la dynamique de l'état excité du MoS_2, un membre des dichalcogénures de métaux de transition 2D (TMDC), dont la structure est très similaire à celle de la pérovskite 2D. Le MoS_2 a été exploré en tant que HTM pour la cellule pérovskite ainsi qu'en tant que couche tampon entre le HTM et la couche pérovskite pour une meilleure stabilité. L'état excité du MoS_2 est déjà bien étudié, mais seulement jusqu'à quelques nanosecondes. La dynamique des porteurs de charge, dont la durée de vie est bien supérieure à quelques nanosecondes et qui est cruciale pour utiliser ce matériau dans le rôle mentionné précédemment, n'a pas été étudiée jusqu'à présent. Nous avons découvert toute la dynamique de l'état excité, depuis les picosecondes jusqu'à la désintégration complète des charge libre 10 microsecondes plus tard. Ceci permet l'utilisation intelligente de ce matériau dans des applications où les charges libres dominent.

Mots-clés

Photovoltaïque, pérovskite, cellules solaires, spectroscopie, pérovskite 2D, interface, 2D/3D, bicouche, basse dimension, caractérisation, optique, état excité, MoS_2, stabilité

Contents

CHAPTER 1

Introduction

Within the many challenges our generation has to face, to most important, is climate change. Its impact is already clearly felt though increases frequency of violent climatic events such as storms and hurricanes, forest fire and many others. Today, it is clear that the problem of climate change has to be tackled and it is reflected in most country's environmental policy. Many international protocols have been set up to protect our climate such as the ban on CFCs to protect the ozone layer or the Paris agreement to decrease the global warming. The question of CO_2 is, however, still a debated issue between countries that tries to balance economic growth and environmental protection . However, to reduce global warming the production of CO_2 has to be diminished. Throughout the different industries, the energy production sector is one of the major contributors of CO_2 emission. According to the IPCC Fifth Assessment Report and the OCDE the energy sector is responsible for $1/3$ of the global CO_2 production on its own.[1] This is the direct result of using fossil fuel as an energy source. More than 60% of the global energy production comes from fossil sources (coal, gaz, oil). Coal being the major player. The global energy consumption is steadily increasing and will continue to do so. By 2040 it is forecast that be Energy demand will increase by 50% from 28 TWh in 2018 to 43 TWh in 2040 (Figure 1.0-1B).
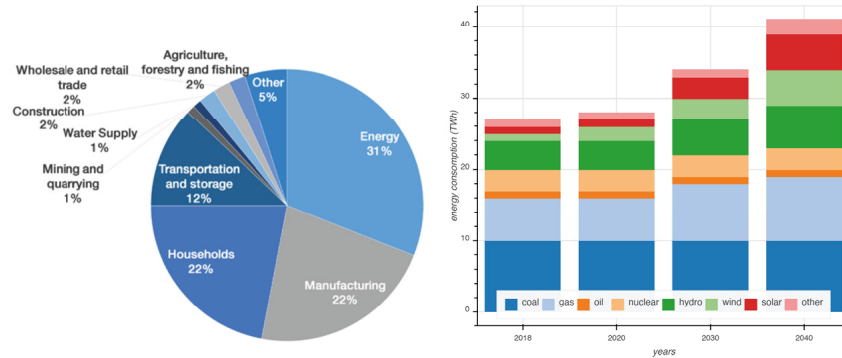
Figure 1.0-1: (a) Energy production by sector*. (b) Projection of energy consumption[†]

For the world to meet the objective of limiting climate changes, most of fossil fuel plant needs to be phased out and replaced by alternative energy sources that are carbon free, not to produce more CO_2, and renewable. Many countries have started an energetic transition toward renewable. These renewable means of production are the following: hydro, wind, solar and nuclear. Each one of them has the advantage and downside. We can divide them into two groups. The first group requires large infrastructure, such as hydro, wind and nuclear power plants. The second does not. Only solar energy fits in this group. Solar energy is the only one that can be set up without requiring centralised plant, as solar panels can be fitted in most rooftops. In addition, solar power doesn't have landscape requirements as the other three have. It only requires sunlight. Solar energy also brings challenges. More specifically on the production and demand miss mach due to the day-night and summer-winter cycles. Some solution exists for this problem. Such as in Australia where massive batteries station has been built by the Tesla company acting as a buffer between the energy production and consumption peaks. This system has even been proven cost effective as the low off-peak energy is stored and sold back to the grid when the price is higher in peak demand. But scaling this solution to the entire planet is impossible. The true solution will, of course, be a mix of everything, with a different distribution in according to the opportunities the landscape provides in each country. But it is difficult

---

*OCED, Paris,France

[†]IEA, Paris,France

to argue against the use of solar energy in the increasing global energy production as it is one of the easiest, and probably applicable in most countries, means to reduce our dependence on fossil fuel. Today the most common solar cell type is Silicon based. It is a proven technology that is becoming more and more affordable thank to the economy of scale driven by China. It has a power conversion efficiency (PCE) around 20% for commercially available panel.The record for lab scale cells being 26.1%. The production process of such panel is energy intensive. It requires very high temperature and very clean environment. The energy payback time(EPBT), the time needed for a solar panel to generate the energy required for its production, for a 2020 mono-crystalline silicon solar cell is around 1 year and 4 months thanks to improved processing methods.[2] But this is still too much. Moreover, silicon panels are rigid and quite heavy. In this optic several
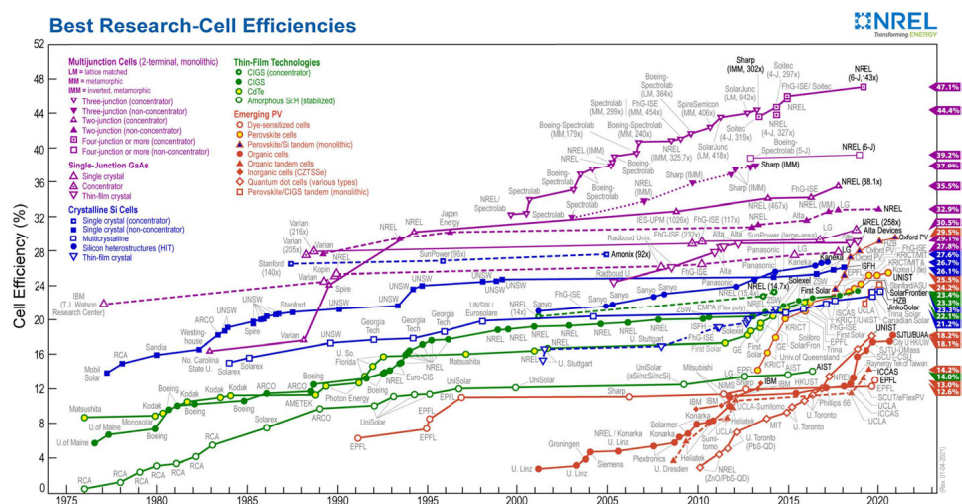
Figure 1.0-2: NREL Best Research-Cell Efficiency Chart 2021[3]

new technology of solar panels have been developed to assess these downsides. One can mention organic photovoltaic (OPV), thin film CdTe and CIGS which has the advantage of being flexible but less efficient. Dye sensitised solar cells(DSSC) which use pigment, mimicking the natural photosynthesis. It is not very efficient(13%) and necessitating a liquid electrolyte, but has the advantage to be colored as pleased and works on low light conditions. The last technology to rise is the hybrid organic-inorganic perovskite(HOP).

It is very easy and cheap to make solar cells with this technology resulting in very efficient device. Since 2013 the efficiency almost doubled from 14% up to 25.5%, in only 8 years(see red and yellow circle on figure 1.0-2). In comparison, it took more crystalline silicon cell 40 years to reach a similar efficiency(blue square on figure 1.0-2). Thanks to its different processing method HOP's EPBT has been calculated to be only 4 months,[4] between half and a quarter of the EPBT of silicon cells. At this moment, This new technology brings challenges that will have to be overcome. The material is not stable over multiple years and all the light-induced processes happening inside the cell is not fully understood yet. This is the motivation behind my work. Trying to understand the inner working of this new technology of solar cells, in the hope of making it a viable new competitor on the solar generation market.

1.1   Light to mater interaction

Before going any further into the subject, we need to understand how does light interact with mater. Formally, the *absorption*, in electromagnetism, stands for the physical phenomenon by which an electromagnetic wave is transformed into another kind of energy. For light to be absorbed in matter, a transition between to electronic state has to occur. This is only possible if the two following requirements are fulfilled:

- The transition between the two states is allowed by the quantum selection rules (transition dipole moment is non-zero).

- The incoming photon energy match the energy gap between the two states.

In molecular systems, such transition occurs between two distinct states, each holding two electrons at most because of the Pauli exclusion principle. When molecules(or atoms) start to pack, their respective states start to interacts, as in figure 1.1-3, but are still distinct from each other. When the number of molecules(or atoms) increase to become virtually infinite in 3 dimensions, as in solids, the levels become degenerate and blends together
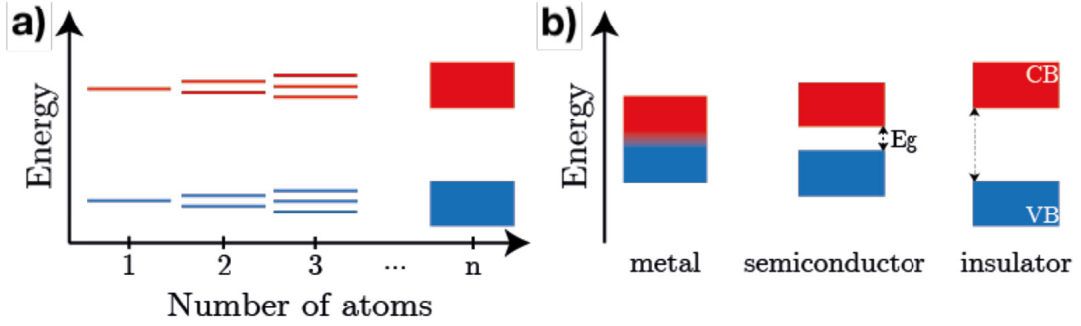
Figure 1.1-3: **A)** From molecular states to bands. **B)** Band diagram of a metal, semiconductor and insulator

to form continuous bands where electrons can live and are separated by a forbidden gap. The highest occupied band is called the valance band(VB) and the lowest unoccupied band is called the conduction band(CB). The energy difference between the two bands is called the band gap (E_g) and it is an important characteristic of solids as it determines the optoelectronic properties of the material. Solids can be classified according to their electronic properties, which is linked to how their band arranges. If the lowest occupied band is partially filled, or the CB and VB overlap, the material will conduct electricity. This is a metal. If there is a band gap smaller than 3 $k_B T$, where k_B is the Boltzmann constant and T the temperature, it is a semiconductor. And if the gap is bigger it is an insulator. Solar devices are made from semiconducting material.

1.2   Semiconductors

In semiconductor physics a useful notion to define it the Fermi level(E_F). The Fermi level is the energy, given a Fermi-Dirac distribution, where there is a 50% chance of finding an electron.[5,6] We can denote three types of semiconductors according to their fermi level:

- Intrinsic

- p-type

- n-type

For intrinsic semiconductors, E_F is in the middle of the gap. For a p-type semiconductor, E_F will be in the gap but close enough to the valence band to be thermally populated due to an excess holes on the band. Similarly, in the case of a n-type semiconductor, E_F is close to the conduction band due to an excess of electrons in the band (figure 1.2-4). To make a p- ot n-type semiconductor, one has to introduce a very small amount, in the order of 1 to 100ppm, of electron rich or electron poor impurity into the material. For example, for silicon, Boron is used as electron poor doping agent and Phosphorus as electron rich resulting in a p- and n-type semiconductor respectively. By tuning the doping agent concentration the Fermi level can be tuned and thus the optoelectrical properties of the material.
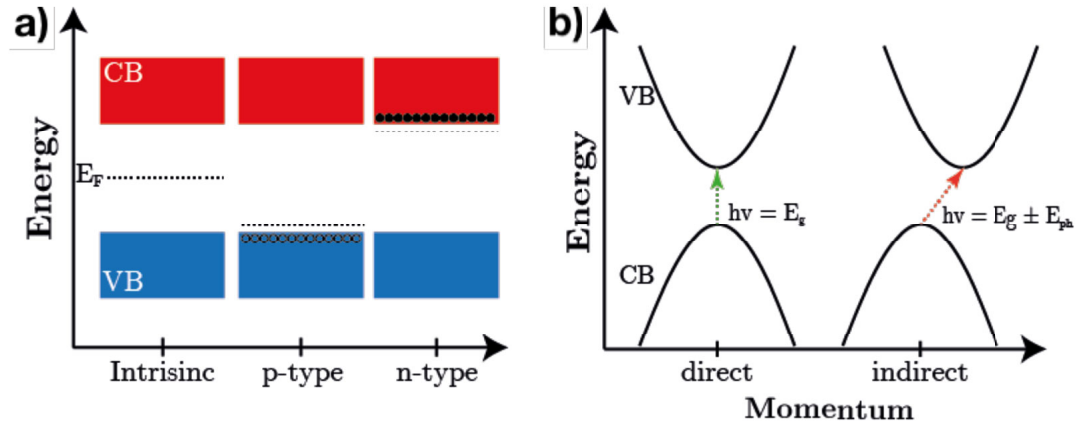
Figure 1.2-4: **A)** Semiconductor types. The Fermi level is represented by the dash line, electrons by filled circles and holes by empty circle. **B)** K-space band diagram for indirect and direct band gap semiconductors. $h\nu$ represent the incoming photon energy, E_g the band gap and E_{ph} the phonon energy.

To describe light absorption in semiconductors it is the convention to work in *k-space*, also called *momentum space* because of the periodic nature of the crystal structure. In such convention the abscissa represents the momentum of the electron and the ordinate the energy and the valence and conduction band are parabolic curves. For light to be absorbed (electronic transition) in a semiconductor, the energy of the incoming photon has to be equal or greater than the band gap. In k -space, such transitions are vertical

for direct band gap semiconductors, or non-vertical for indirect band gap. A transition is labeled *direct* if it fulfills all selection rules, resulting in a very strong absorption. An indirect transition can only occur by coupling the incoming photon with a phonon(lattice vibration) resulting in a weaker absorption, a 1000 fold compared to a direct transition.

1.2.1   Photo-carriers

When light is absorbed in a semiconductor an electron from the valence band is promoted in the conduction band. We call this electron a photo-carrier. The nature of such carrier can vary a lot depending mainly on the dielectric constant (ϵ_r) of the material. It can remain more of less correlated to electronic vacancies it left behind, called a hole. In short the dielectric constant of a material represents how easy a material can polarize in an electric field and thus how easily it can sustain a displaced charge. The amount of coupling between the electron and the holes will determine the characteristic of the photo-carrier. No coupling, and we have a free electron. If there is a coupling, we have an exciton. More in detail, an exciton is a quasi-particle found in semiconductors that can be seen as electron-hole pair linked by Coulomb forces where the electron orbit around the hole. By analogy with the hydrogen atom. The orbiting radius of the exciton is called the Bohr radius and its length classify an exciton in 2 categories:

- Wannier-Mott exciton

- Frenkel exciton

Wannier-Mott(WM) excitons are characterized by a large Bohr radius, much larger than the crystal lattice parameter.[7,8] They are typical of large dielectric material where the electron-hole interact is partially screened resulting is small Coulomb interactions in the order of 0.01-0.1 eV. A Frenkel(F) exciton, on the other hand, has a much smaller Bohr radius,[9] smaller than the lattice parameter as in figure 1.2-5. This kind of exciton is typically found in molecular system or in material with a small dielectric constant giving rise to a large coulomb interaction,0.1-1 eV, keeping the electron and hole close. There

is a third, intermediate, exciton called charge-transfer exciton. It is characterized by a Bohr radius between the two others, has a dipole moment and generally occurs across an interface typically between a donor and acceptor.

Wannier-Mott   **Frenkel**
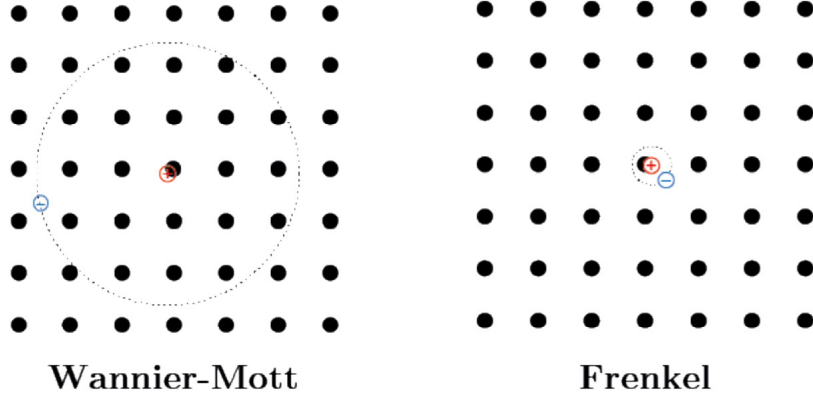
Figure 1.2-5: Wannier-Mott and Frenkel exciton models. The lattice is represented by black circles, electrons and holes by blue and red circle respectively and the exciton Bohr radius by a dashed circle.

Energetically speaking, excitons are mid-gap state meaning that their energy level is within the bandgap of the material, while free electrons will reside in the conduction band. The energy difference between the conduction band minimum and the excitonic state is called the exciton binding energy (E_b). Both types of excitons is optically active. They appear as a very defined peak within or below the absorption edge of the material (figure 1.4-11). The hydrogen atom models use as an analogy to describe the exciton describes the different electronic transitions well as they follow a similar spectral series(eq 1.1).[10]

$$E(n) = -\frac{\frac{\mu}{m_0 \epsilon_r^2} R_H}{n^2} \tag{1.1}$$

Where $E(n)$ is the spectral energy of the nth level, R_H the Rydberg constant, μ the reduced mass of the electron and hole, m_0 the electron mass and ϵ_r the relative permittivity. Following the hydrogen atom analogy we will name the different electronic transition of an exciton $1s$, $2s$, etc, for respectively the first transition, second transition and so on. Considering the band gap absorption and the exciton absorption in semiconductors, a model,

not expanded here, has been developed by Elliott to describe the optical absorption of semiconductors.[11]

At this point all the main notions concerning the excitation, light absorption, in semiconductors has been described. We miss what followed, the desexcitation, where the material relaxes back to ground state.

1.2.2 Recombination processes

The "death" of photo carriers is called the recombination as it involves an excited electron recombining with the hole it left behind in the valence bande. Such process can be *radiative* or *non-radiative*. In the first case, as the electron recombines with a hole, a photon is emitted with the energy match the energy gap. In the second case, the energy is dissipated in the lattice as heat. The recombination is a dynamic process. And as such, the change in the population of the excited state can be expressed by the general rate equation.

$$- \frac{dn(t)}{dt} = k_1 n + k_2 n^2 + k_3 n^3 + ... \tag{1.2}$$

Where $n(t)$ is the population of the excited state and k_i the rate constant associated to the pathway of order i. The different orders are associated with the different recombination process. Only the three main recombination pathways are presented :

- The Shockley–Read–Hall (SRH) recombination, 1st order (n)

- The band to band recombination (or bimolecular recombination), 2nd order (n^2)

- The Auger recombination, 3rd order (n^3)

The first process, SRH recombination, consists of a trap assisted recombination usually caused by lattice defects.[12,13] Traps are a energy stat that is below the conduction band where free carrier can "fall in" and get stock. In semiconductor this process is usually happening at low excitation density where the density of photo carriers is lower than the density of traps. The second recombination process is simply an excited electron in

the conduction band recombining with its hole in the valence band. This is the main radiative pathway. Finally, the last process, The Auger recombination occurs at a very high carrier density where one cannot neglect carrier interaction. This pathway is a three body interaction where and excited electron is transferring its energy to another excited electron that will be promoter higher(in terms of energy) in the band. The three main pathways are exemplified in figure 1.2-6
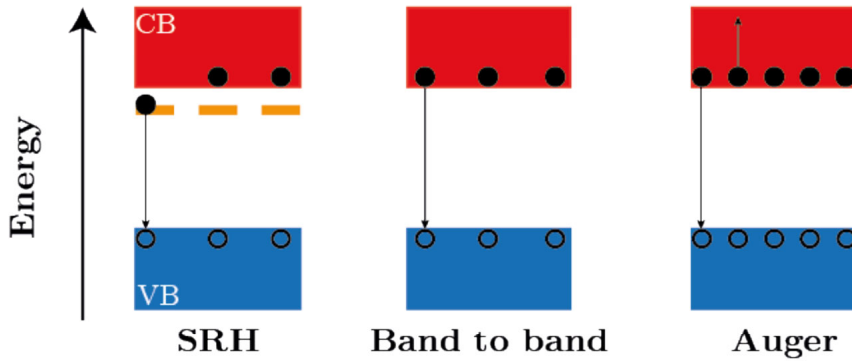
Figure 1.2-6: Main recombination mechanism: SHG, band to band and Auger recombination. The conduction and valence bands are represented in red and blue respectively. Traps are represented in orange

The solution of equation 1.2 will be a sum of exponential decay. Each recombination channel will thus have an associated time constant(τ). As both radiative and non radiative recombination happens at the same time, we define the quantum yield as being the ratio if the time-constants relative to the radiative and non-radiatives processes.

$$\eta = \frac{\tau_r}{\tau_r + \sum \tau_n} \leq 1 \tag{1.3}$$

Where τ_r is the time constant associated to the radiative process and τ_n the non-radiative ones (SHR and Auger). A material quantum yield close to 1 means that most photos absorbed will be reemitted. The material will have a very bright fluorescence and $\tau_r >> \tau_n$. The fluorescence time constant is an important parameter for the study of optoelectronic

material as it is usually a signature of low trap density and a direct band gap two desired properties.[14,15]

1.2.3 Quantum confinement

Most semiconducting materials are bulk three-dimensional(3D) crystals. In the 70s, a subgenre of semiconductor which aren't three dimensional was created.[16,17] This opened the door to new materials: quantum wells/sheet(2D), quantum rods(1D) and quantum dots(0D), all with peculiar optoelectronic properties due to quantum confinement.

To comprehend what is and how does quantum confinement work, let's take the quantum dots example. Quantum dots are nanometer sized, typically in the order of 100nm, mostly spherical semiconductor particles. They do absorb light as their bulk counterpart but as the size of the particle decreases there will be a point where the diameter will start to get smaller than the exciton Bohr radius. From that point we can see the problem as quantum particles in a box. As the box, here the quantum dot, shrinks the energy level of the particle will spread resulting in a shift of the optical properties to the blue(higher energy). Carriers in quantum confine systems are not free to move in all direction, but will be restricted in a 2D plane, 1D rod or a 0D dot. In addition to physical confinement. Carriers can be dielectrics confined. This method was used by Tsu et al. in the 1970 experiment.[17] Typically used for quantum wells, it consists of sandwiching a very thin layer of a material with another one having a different dielectric constant or band gap. Carriers will be confined in the higher dielectric material, the second one acting as a barrier, confining carrier in a plane(2D) as in figure 1.2-7. There is different type of quantum well according to the way the valence and conduction band of the two materials aligned with each other. In the case of figure 1.2-7 the two maxima and the two minima are aligned, it is thus a type I. If the minima if material A is aligned with the maxima of material B, meaning that the valence band of A is lower the B one and the conduction band of A is also lower than the B one, it will result in a type II.
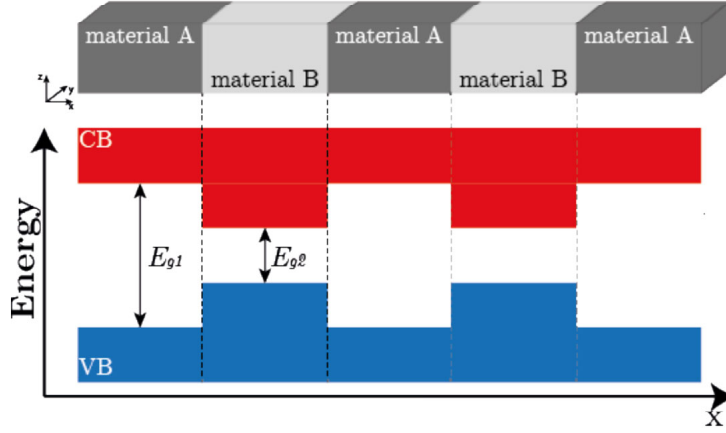
Figure 1.2-7: Band diagram of a type I quantum well created by sandwiching two semiconductor with different bandgap: E_{g1} and E_{g2}.

1.3 Solar cell

So far we have described the physic of semiconductors and the phenomenon impacting the photo carriers. Here we will have a look at how we can take advantage of the semiconductors properties to extract current and make a solar cell.

1.3.1 Working principle and characteristics

In an abstract way, a solar cell works by preventing the photo-carrier recombination within the material, by extracting them out of it through electod and put them back in the material at the other side. To do that we need to create a so-called p-n junction by putting together a n-doped and a p-doped semiconductor. When in contact their different Fermi level will join creating a slop. When a junction is excited with light the excited electron in the conduction band in the p-doped material will drift through the junction in the n-doped region toward a collection electrode to be extracted as exemplified in figure 1.3-8A. The collected electron will then be funneled though a circuit back to the other side of the junction, completing the circuit creating a current(I_{sc}). If the circuit is open, a potential can be measured between the two sides, called the open circuit voltage(V_{oc}).

The open circuit voltage and short circuit current are two important parameters that
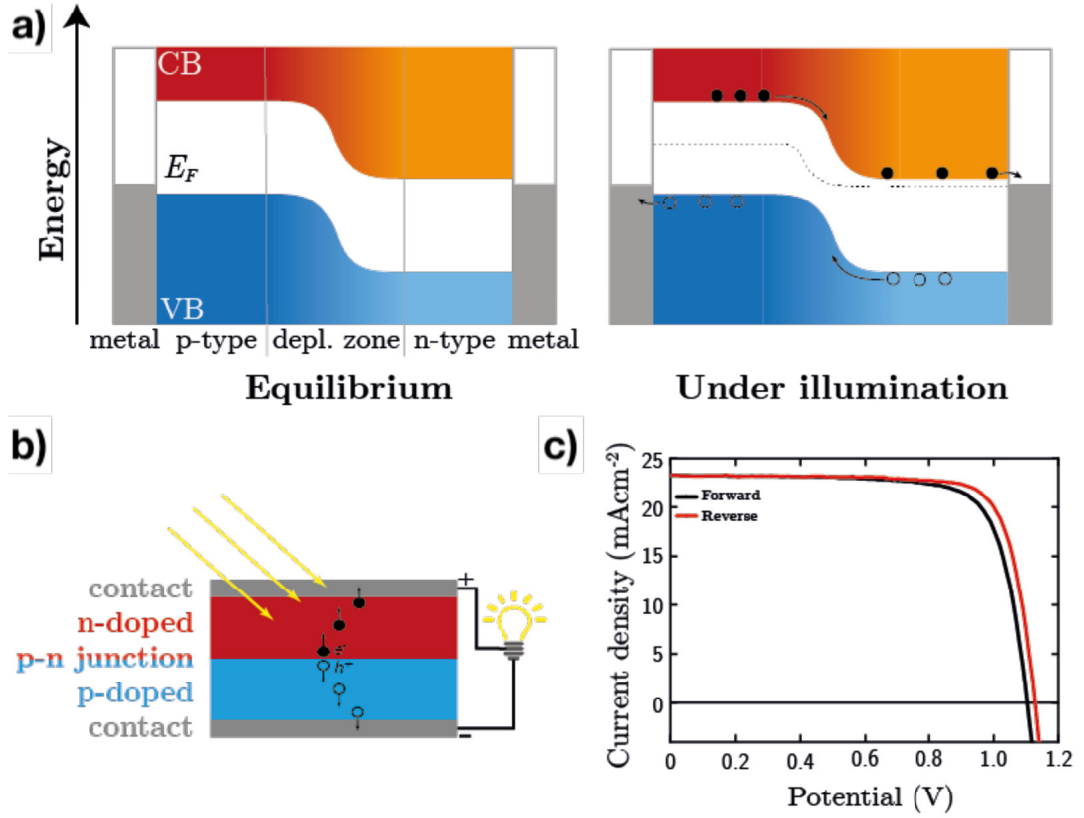
Figure 1.3-8: **A)** Band diagram of a pn-junction at equilibrium and under illumination.**B)** Silicon solar cell schematic **C)** IV scan, forward and backward

characterizes a solar cell. To measure them a current-voltage(IV) scan which consists in applying a voltage to a cell under light an measuring the current output is performend. The I_{sc} can be normalized by the cell area giving rise to the current density J_{sc} which is the conventionally used. The I_{sc} is read at 0 potential and the V_{oc} at 0 current. Figure 1.3-8C present an IV scan. The scan can be done in both directions. The miss mach between the forward and reverse scan is called the hysteresis. It can be quantified by the hysteresis index (H_i):[18]

$$H_i = \frac{PCE_{\text{reverse}} - PCE_{\text{forward}}}{PCE_{\text{reverse}}}$$

Where the PCE is the power conversion efficiency.

$$PCE = \frac{P_{out}}{P_{in}} = \frac{J_{sc}V_{oc}FF}{P_{in}} \tag{1.4}$$

In addition to these parameters there is: the maximum power point(MPP) which is the point on the J-V graph where the cell will output the most power. The fill factor(FF) which is an ideality factor comparing the maximum theoretical power output given at J_{sc} and V_{oc} and the effective one J_{MPP} and V_{MPP}.

$$FF = \frac{J_{MPP}V_{MPP}}{J_{sc}V_{oc}} \tag{1.5}$$

A single pn-junction solar cell will not absorb the full solar spectrum efficiently. Indeed all the low energy photo(lower that the band gap) will not be absorbed and are thus lost. The higher energy one will be absorbed but because of intra-band relaxation all excess energy with respect to the band gap will be lost. As a result, with a small band gap most of the spectrum is absorbed giving rise to a high J_{sc} but they V_{oc} will be low due to the small energy difference between the bands. In the opposite case, with a high band gap, only the blue part of the spectrum is absorbed resulting in a low J_{sc} but a high V_{oc}. On this principle and factoring in geometrical constraints and the solar spectrum William Shockley and Hans-Joachim Queisser calculated a theoretical maximum for a single bandgap solar cell of 32%.[19] This maximum can be surpassed if multiple absorbers are used to create a so call multi-junction solar cell with four or more different band gaps are used to minimise as much as possible losses and achieves close to 50% efficiency*NREL chart. Such solar cells are theoretically ideal, but practically very challenging. Most need a concentrator to illuminate all the layers enough to reach the maximum efficiency. In addition, the engineering of such multilayered system mad from single-crystalline semiconductor material is not at all trivial.

---

*.

1.3.2 Solar cell technologies

Today there are many types of solar cell using different base material and or architecture. The first generation, more crystalline wafer based such as silicon are by far the most used commercially and GaAs(Gallium Arsenide) solar cell used in satellite usually in a multi-junction configuration, more expensive but also more efficient than silicon. This generation is made in majority by epitaxial growth. The second generation, thin film based, with CIGS(copper indium gallium selenide) and CdTe(cadmium telluride) solar cells as the advantage of being flexible. All of the above are pn-junction semiconductor based technologies and differs mainly by the material used. As mentioned above, multi-junction cells is a category onto itself. The 2d generation is usually made by CVD(chemical vapor deposition) deposition technique. Beside that there is the emerging PV, 3rd generation, mostly still confined to labs like dye sensitised solar cell (DSSC) based on colored dyes as light absorbers, organic cells (OPV) based on conducting polymers, and the latest and, according to some, the most promising technology, the hybrid perovskite solar cell(PSC).[20,21] All of those are solution-processed. Being the studied material at the center of this work, let us have a close look at what are hybrid perovskite(HP) and how a PSC is made.

1.4 Hybrid organic-inorganic perovskites

Perovskite, originally designated a mineral, $CaTiO_2$, discovered in the 19th century and named after a Russian mineralogist Lev Perovski. Today all compounds of structure ABX_3, where A is a monovalent cation, B a divalent cation and X an anion, are called perovskite. The perovskite family is numerous with many practical applications such as piezoelectric driver,laser medium, scintillators, photovoltaic,etc. The hybrid perovskite is a subgroup with a small organic molecule use as A site cation, typically methylammonium(MA), resulting in a organic-inorganic hybrid material. This latter group is the one

of interest regarding photovoltaic applications since Kijoma et al. used it to make the first PSC.[22]

1.4.1 Structure and properties

The prototypical composition for photovoltaic is methylammonium(MA) lead(Pb) iodide(I) for the A site,B site and anion respectively, call MAPI. Organic-inorganic perovskite are semiconductor with a direct band gap, for MAPI of 1.58 eV. The band structure is mainly dictated by the halide and lead. Gradually substituting the iodine by bromine or chlorine will result in a wider and wider band gap. As a result, hybrid perovskites are a highly tunable material, opening a wide window of opportunities as it allows a very easy application specific material design, with specific structure and optoelectronic property requirements.[23]

For solar cells, one needs a perovskite with a cubic structure as it is the one with the required semiconducting properties with the optimum bandgap. The B cation is coordinated to six X anions disposed in an octahedral pattern around B. Each octahedron is corner sharing, forming a three-dimensional structure. The A cation fills the void between the octahedron. Figure 1.4-9 on the left illustrates the perovskite structure. One cannot used any element to form a perovskite structure. Indeed, the B site cation need to have a 6-fold coordination allowed. Furthermore, the requirement on the relative size between A, B and X to form a cubic structure is strict.Wwe can use the Goldsmith tolerance factor[24] to predict if the chosen elements will result in a cubic structure:

$$t = \frac{r_A + r_X}{\sqrt{2}(r_B + r_X)} \tag{1.6}$$

where r_a, r_B and r_X are the ionic radius of the A and B cation, and the X anion respectively. This index, if between 0.9 ad 1, predict a preferred cubic arrangement. If less the preferred structure will not be cubic but orthorhombic, If greater than 1, tetragonal or hexagonal. The electronic structure of the material is mainly dictated by the inorganic
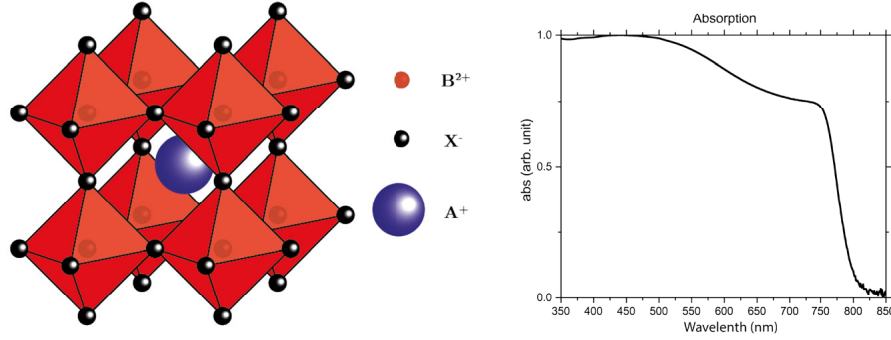
Figure 1.4-9: Hybrid perovskite crystal structure(left), MAPbI$_3$ absorption spectra(right)

octahedron. The valence band is being constructed mostly by, in the case of MAPI, the Pb 6p orbital and the conduction band by the I 5s orbital. This can be extended to other perovskite blends, the B-site p-orbital will be responsible for the valence band, and the X-site s orbital for the conduction band.[25] The A-site cation involvement in the electronic structure is more subtle. It is not directly involved in the structure but does influence it via H-bonding and steric deformation of the lattice by inducing tilting. The A-site tuning was shown to change the bandgap and electronic properties of the resulting perovskite expending, furthermore, the tunability of perovskite devices.[26–28]

The optical and electronic properties of perovskite for solar devices are a high absorption coefficient, as any direct semiconductor with the addition of long-lived carriers which is usually linked to an indirect semiconductor. This paradox can be explained by the effect the heavy atom in the B-site generated. The spin-orbit coupling induced by the lead atoms in addition to a non-centrosymetric structure is believed to be the origin of a Rashba splitting of the conduction band minimum. This creates two minima separated by 50meV in k-space. The first minimum is aligned with the valence band maximum and the other one is shifted by 50mev and supposed to be slightly lower in energy. From this arises a direct bandgap to the first minimum with the related absorption properties. The second minimum being the source of the slow recombination.[29–31]

The electronic structure of hybrid perovskite is indeed more complex than standard

semiconductors such as GaAs. In addition, semiconductor characteristics such as exciton binding energy and carrier mobility and diffusion length are difficult to characterise precisely. Many reports of such parameters differ in values ranging up to an order of magnitude difference in exciton binding energy(Eb) from 2meV up to 150meV depending on the method used. The ionic and quite soft constitution of the perovskite render the classical semiconducting properties difficult to assess.[32,33] As expected, as the composition of the material changes, the exciton properties change with it. However, trend can be seen whereas the iodide is replaced by a smaller halide, the binding energy increases. The binding energy is essential for solar cells. Exciton is something to prevent as much as possible as only free carriers can be harvested to produce electricity, thus energy will be lost in the process of splitting the exciton into free carrier. In addition, the lifetime of an exciton is short (from 10ps up to 1ns). Thus preventing the formation of exciton contributes to increase the overall photogenerated carrier lifetime and this increases the probability carriers of being collected at the electrodes. The ratio of free carrier to excitons of a material upon illumination can be described by the Saha equation.[34,35]

$$\frac{n_{free}^2}{n_{ex}} = \left(\frac{\mu_X k_B T}{2\pi \hbar^2} \right)^{3/2} e^{-E_b/k_b T} \tag{1.7}$$

Where n_{free}^2 and n_{ex} is the free carrier(e^- & h^+) and exciton density and μ_X the exciton mobility. This equation can yield two regimes. With small E_b(<50meV) the free carrier will be prevalent whereas with large E_b(>150meV) the exciton dominated. In between, the fraction depends on the excitation density. The larger the excitation density, the more excitons are promoted. Triple cation perovskite having an exciton binding energy around 50meV, it is mainly free carrier dominated. In GaAs, which has an E_b of 4 meV, free carriers completely dominate.[36] In comparison, organic PV, known to be exciton limited, has binding energies greater than 500meV with efficiency of less than 10% at the lab scale.[37,38]

One of the amazing attributes that make perovskite so interesting to study is that

despite the relative *dirty processing* method (in comparison to standards from the semiconductor industry), the materials exhibit exceptional transport properties rivaling with high-quality single crystal semiconductors such as silicon or gallium arsenide, despite being polycrystalline. To make a perovskite film, the go method is a solution processed deposition yielding a polycrystalline thin film of about 500nm in thickness. The detail of PSC making is developed in section 1.4.3. The resulting thin films exhibit similar traps or defect density as a monolithic single crystal of silicon or GaAs, around $10^{17}-10^{18}cm^{-3}$.[39–43] No need for complex furnaces with high temperature and ultra-pure precursors to make a perovskite cell, rendering the sample preparation very efficient and fast. This was one of the major contributors in the boom in perovskite research. The barrier to enter the perovskite field was quite low and allowed for rapid improvement of the material and thus device efficiency from 3% to 25.2% in only 10 years.[22,38] In comparison, silicon and other commercial solar cells took 20+ years to reach their full potential.

1.4.2 Low-dimensional perovskite

The versatility of the perovskite structure is even greater than discussed before when the family is expended on the low-dimensional perovskite. If one starts with a regular ABX_3 perovskite and replace some of the A-site organic cation by a larger one (R), too large to fit in the cavity formed by the corner shared octahedron(cf. figure 1.4-9) the 3D crystal lattice can be sliced along one of the crystallographic planes. Similarly to figure 1.4-10 the resulting material is a alternation of inorganic corner-shared hexahedron layer separated by organic cation from another inorganic layer. The structure is transformed from ABX_3 to R_2BX_4 when all A-site cations are replaced by R-cations, effectively becoming a layered system: 2D perovskite(2DP). When a mixture of A- and R-cation one can obtain a hybrid between 3D and 2DP. The inorganic sheet are not mono-layered anymore but are composed of multiple inorganic sheet held together by the small A-cation. Those are called quasi 2D perovskite and have the general structure $R_2A_{n-1}B_nX_{3n+1}$. The number of inorganic layers held together is denominated by the letter n. A pure 2D perovskite

has $n = 1$, quasi 2D n=2,3,4,... and when no R-cations are used $n = \infty$ yielding standard 3D perovskite(3DP). 2D-perovskites are named like this because they are composed of mono-layers of inorganic, optically active material, effectively sheet-like, separated from another by organic molecules.
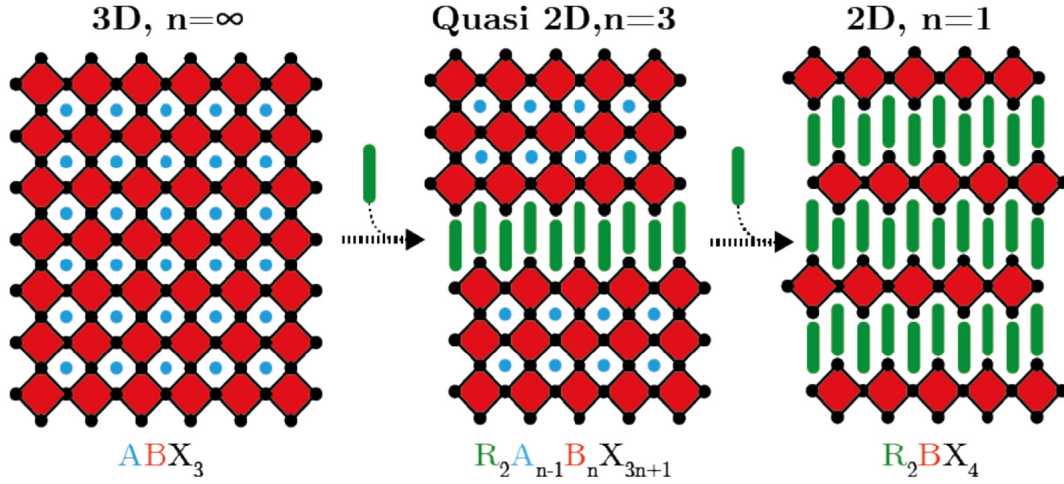
Figure 1.4-10: Low-dimensional perovskite structure transformation scheme from 3D to 2DP

The optical properties of 2DP are different from 3DP because of the layered structure. The inorganic layer of the 2DP is separated by an insulating organic layer, there is no delocalisation between the two layers effectively making a quantum well as described in figure 1.2-7. The organic layers are the large bandgap material(material A in figure 1.2-7) and the inorganic sheets the low bandgap one(material B in figure 1.2-7). In addition to the layering. The thickness of the optically active layer is limited by the I-Pb-I bond length of the inorganic layer. The other two dimensions are effectively infinite. This makes 2DP an anisotropic material with one of its dimensions experiencing quantum confinement. All this combined makes the properties of 2DP dramatically different from 3DP.[44] Indeed, the materials exhibit very strong excitonic properties, as we can see on figure 1.4-11, with a very strong excitonic absorption peak below the bandgap. The bandgap of 2DP, because of the confined dimension is blue shifted with respect to 3DP, usually around
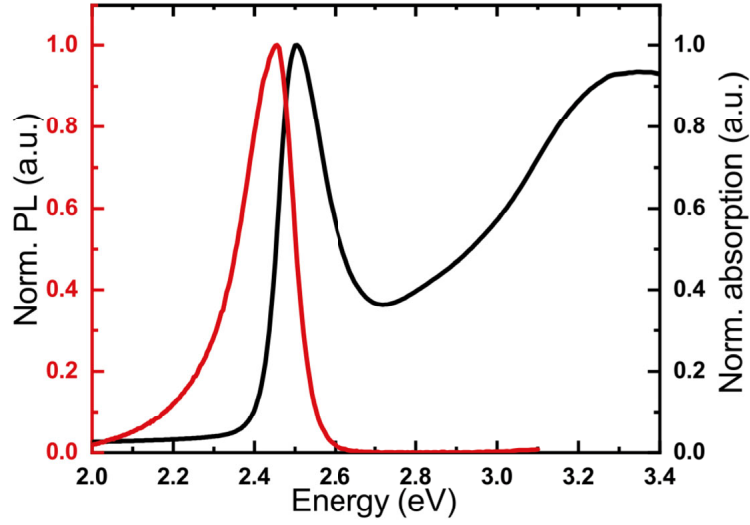
Figure 1.4-11: Absorption (black) and photoluminescence (red) spectra of a 2D perovskite

500nm for a standard $(PEA)_2PbI_4$. The organic R-cations, similarly to the A-cations of 3DP, are not electronically coupled to the lattice. Thus, changing the cation does not directly influence the electronic properties of the 2DP.[45] However, it does influence the octahedral twist of the inorganic lattice which does change the optical properties. A more twisted structure will have an effective quantum well dimension reduced compared to a flatter structure inducing a blue shifted absorption of tens of nanometers. In addition, chemically modifying the cation can change the dielectric constant of the organic layer. These influence the exciton binding energy and energy levels of the perovskite.[46] As well, similarly to 3DP switching the halide of the inorganic layer induce a large shift in the optical properties.

More structurally speaking, the 2D perovskites exhibit a vast improvement in stability with respect to water exposure. Thanks to the organic layer protecting the water-sensitive inorganic layer, the material is very stable. This is especially interesting when coupling 2D and 3D perovskites together. The narrow absorption and high exciton binding energy of the 2DP does not make for a good candidate for an efficient solar cell. However, its stability can be leveraged to protect a 3DP cell, increasing the stability and boosting

the efficiency.[47,48] Indeed, in addition to increasing the water resistance of the 3DP, the 2DP can be tuned to act as a hole transporting material/electron blocking layer or as a passivating layer between the 3DP and the HTM.

Oddly enough, the study of 2DP goes back long before the hybrid perovskite era. Research of 2D layered perovskite goes back to at least the 1980's.[49,50] They remained a niche subject until the mid 2010's when the very active hybrid perovskite community made the research on this 2D material resurface. The newly "rediscovered" material has become very interesting as a derivative of hybrid perovskite for device makers to improve the stability of the PSC, and to physicists for its unique excitonic properties and tunability.

1.4.3   Perovskite solar cell processing and optimisation

Perovskite solar cell are, as mentioned above, part of the 3rd generation of solar cell, namely the emerging solar technologies. One of the main differentiation points with respect to 1st and 2nd generation cells, material aside, is the processing methods. The PSC deposition method is almost entirely solution-based. Given this, there are several ways of depositing a solution on a substrate, namely: spincoating, spray deposition, doctor blading, meniscus coating, and more. Here we will focus on the most common method, the spincoating.

Figure 1.4-12 describes the solution process method commonly used to make a PSC. There is two different cell configurations: the standard n-i-p and the inverted p-i-n. The two configurations refer to the directionality of the cell. In the n-i-p, the electron flows toward the illuminated electrode as the hole goes toward the back electrode. In the inverted configuration, the directionality is reversed.

For making a n-i-p cell, all start from the substrate: a piece of conductive glass, usually fluorinated tin oxide(FTO) doped glass. On this substrate, a compact layer of TiO_2 is sprayed. This layer acts as an electron transport(ETL)/hole blocking layers. On top, a layer of mesoscopic alumina or TiO_2 can be added for improved PCE, but is not
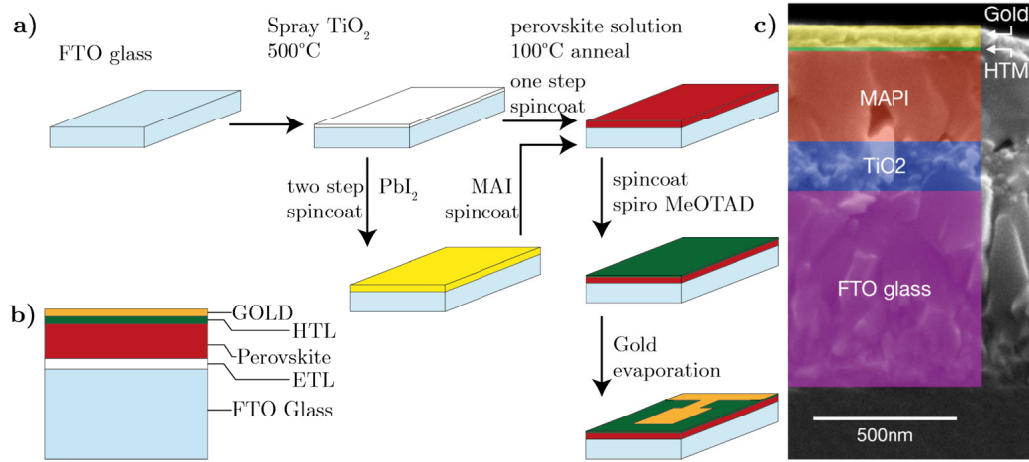
Figure 1.4-12: (a) Processing steps in the making of state of the art an n-i-p PSC, (b) scheme of the completed cell, c) Cross section SEM image of a MAPI cell[51]

strictly necessary.[52] Different treatment can be performed on the ETL to improve its characteristics, such as the addition of to LiTFSI.[53] Afterward, the perovskite solution is spin-coated in either one or two steps. The one-step methods simply use a solution of the perovskite precursors: MAI and PbI2 for MAPI.

In the two-step process, first, a solution of PbI_2 is deposited and dried. On top of it, a second solution containing the cation MAI is spin-coated. Then the film is annealed with both methods to evaporate the remaining solvent and crystallize the perovskite. Prior to annealing, an antisolvent step can be performed. The latter consists in the spincoating of a solvent that is "orthogonal" to the film, meaning that it cannot dissolve it, usually chlorobenzene. This step will help in the crystallisation process of the perovskite. When the perovskite layer is formed, an hole transporting (HTL)/electron blocking layers of Spiro-oMeTAD is spincoated. The HTL solution, similarly to the ETL, can have some additives to improve the electronic properties. Finally, the cell is placed in a metal evaporator to apply a thin gold back electrode. Figure 1.4-12 b) shows a scheme of the completed cell along a real cross-section SEM image of a MAPI cell in 1.4-12 c). At each step of the process improvement can be made in either the material or the processing. The scope of tunability of PSC is thus enormous. Extra layers can be add, changed,

or even removed entirely for making ETL or HTL-free devices, for example.[54–56] Each modification is having the ultimate goal of attaining the perovskite nirvana of a stable and efficient large area device.

At the beginning of the perovskite boom, the optimisation of the device was mostly trial and error based. Nowadays, the research aims more and more at understanding how each layer interacts with each other for a more precise, more intelligent, device optimization. To this day, one can achieve very high efficiency, over 25% on a small device that will deteriorate in a few weeks.[38] Or, a very stable but with a low efficiency device.[57] Then comes the scalability issue as the processing method used in the lab hardly scales to a larger standard $24cm^2$ module. These are the three axes of research of the device makers: efficiency, stability, scalability. Realistically, these three researcher axes are not independent, they are very interdependent rendering the optimisation process a complex problem.

1.5   Motivation and strategy

At the start of my thesis, 2D perovskite started to appear on the radar of HOPV research groups. They were seen as a great opportunity to improve the stability and efficiency of 3D perovskite either by blending the two materials together, or by interfacing them as a bilayer. However the interaction of the two materials was not under high scrutiny. I thus decided to focus on this lack of knowledge and decided to study 2D perovskite and the interface of the latter with 3D perovskite for improved stability and efficiency of HOPV cells. To do that, I adopted the following strategy:

First I studied a new 2D perovskite designed to have a higher stability toward water thanks to highly fluorinated cations. This group of perovskites was revealed to have quite diverse optical properties with a high degree of tunability according to the chosen cation.

After realising the diversity of this family of perovskites and their related optical characteristics, I decided to investigate more deeply the optical phenomena present. I focused

my attention on a 2D perovskite made with one cation: A43. This material was chosen because of its unique optical properties. It turned out that the unique electrostatic potential of the cation in conjunction with its steric hindrance yielded long lasting electron-hole pairs in the material.

Following the study of 2D perovskites, I have focused on the interface between 2D and 3D perovskites. I have revealed how the 2D layer structurally arranges on the 3D perovskite. How the 2D layer prevent degradation of the 2D layer by blocking the small molecule in the 3D layer from migrating out of the crystal structure. Following that, we also assessed the improved thermal stability of the bilayer cell thanks to the 2D perovskite again preventing the degradation of the 2D layer.

Lastly, in an attempt to diversify the material investigated, by studying another layered material family: Transition metal dichalcogenide monolayers. This family of material showed compatible properties with an HTM role. The long-lived excited state of these materials, more specifically MoS_2 wasn't studied. I thus have examined the long-lived free carrier dynamic of the latter material.

Overall, this work presents the investigation of new 2D perovskites, the interfacing of 2d and 3d perovskite, the extensive exploration of the behavior of this type of interface and the analysis of another 2D layered material family carrier dynamics for use a potential in PCS.

CHAPTER 2

Experimental Methods

This chapter will discuss the different measurement techniques used in this work. We will go though the working principle, and discuss the information they provide us about the studied materials. This work is centered around the understanding of photoinduced processes, understanding the optical properties of the studied material is thus a prerequisite to any further investigation, and it starts with the absorption and emission properties. Afterward, to dig into the intimacy of the material, more complex, mainly time-resolved experiments are needed. These time-resolved methods allow us to probe the evolution of the photoinduced carriers and understand their behavior. In addition, the data analysis tools created for the occasion will be discussed as well as models developed to extract meaning out of it.

2.1   Steady state optical measurement

The Absorption spectrum, also called linear absorption spectrum, allows to identify the band edge as well as other optically active transitions such as the excitonic transition. To infer the band edge energy, it is common to use the Tauc analysis.[58] This analysis does not give a precise value but is useful enough for that matter. Looking at the absorption

spectra at different temperatures allows for the exploration of the strucural phase change in the material as the spectrum shifts abruptly when it occurs. One example of a phase change can be seen in figure S3.2-2 in the annex. The absorption spectra in black in figure 1.4-11 show the characteristic absorption peak of an exciton transition followed by the rise of the band edge. This shape is very typical of a 2D perovskite with a band edge around 2.7 eV and an exciton binding energy of 200 meV.

The photoluminescence(PL) spectroscopy is the sister experiment to the absorption spectroscopy. In the latter, we look at what wavelengths are absorbed. In PL spectroscopy, we look at the wavelength emitted from the material upon excitation. In the case of figure 1.4-11 The emission is due to exciton recombination. This measurement is principally used to assess the emissive properties of a given sample. It can also reveal, to an extent, the process behind the emission by looking the energy difference between the maximum of emissions and absorption, called the stokes shift. This is important is asses the excited state picture of the sample. The PL spectroscopy can also give access to the quantum yield of a material(see eq. 1.3 in section 1.2.2). The PL spectrum in red in figure 1.4-11 is also very typical of 2d perovskite with the very sharp peak and a small Stokes shift.

2.2   Time-resolved fluorescence spectroscopy

This method is pretty self-explanatory. Time-resolved fluorescence spectroscopy is a measure of the fluorescence of a material resolved in time. The most common method to measure it is: Time-correlated single-photon counting(TCSPC). In brief, it uses a high-frequency pulsed monochromatic source with very low intensity to excite the material and measure the time delay between a start and stop signal. The start time is equal to the time the source pulse took to go from the source to the detector without any sample. The stop time is equal to the time between the source pulse took to go from the source, absorbed in the material, emitted from it and to the detector. Over a period of time, the
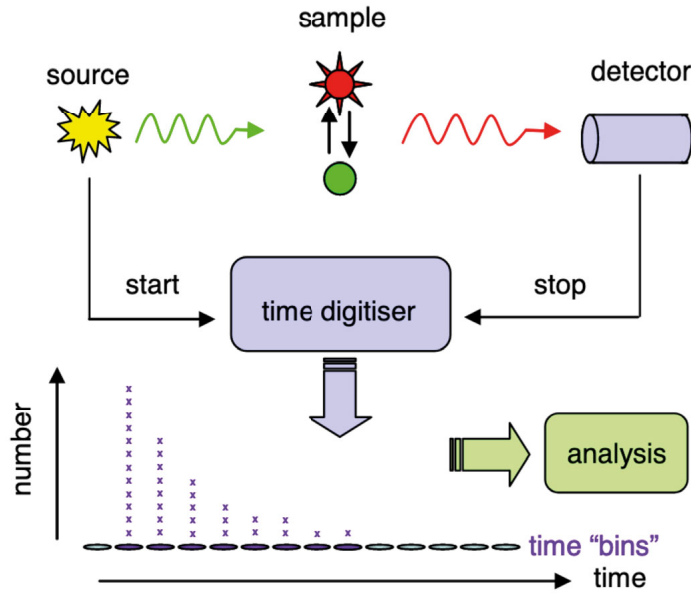
Fig. 1. Schematic for TCSPC

Figure 2.2-1: TCSPC setup diagram

accumulation of different time delays will result in a fluorescence decay curve where the amplitude at each point is propositional to the number of photons with that particular delay. Using this curve, we can assign a fluorescence time constant(τ_f) to the material by using and exponential fit as the fluorescence intensity can be expressed by:

$$I(t) = I_0 e^{-t/\tau_f} \tag{2.1}$$

The fluorescence lifetime is a useful characteristic of a material especial when interfacing it. Indeed, looking at how τ_f changes when an electron or hole extracting layer is interfaced with the material gives information about how well these two materials work together. For example, an increased lifetime means that it suppresses the recombination site at the interface. A decrease in lifetime might be due to a transfer process from one material to another decreasing the number of carriers recombining radiativaly, also called quenching. It is important to note that the decay is usually not a single pure exponential

decay. At this point, there are two ways of analysing it. Either using a sum of two or more exponential decays, each with a different time constant and amplitude.

$$I(t) = \sum_{i=1}^{n} a_i e^{(-t/\tau_i)} \tag{2.2}$$

The analysis using this function will result in comparing the diffrent τ_i and because they are exponential functions the fit are quit ill define and they τ_i are not completely independent. This can make the interpretation difficult. Another method, quite similar to the previous one exist, using a stretch exponential function.

$$I(t)_\beta = I_0 e^{(-t/\tau_c)^\beta} \tag{2.3}$$

Where τ_c is the characteristic lifetime of the exponential and β the stretch factor with values between 0 and 1. A pure exponential will have $\beta = 1$. This function can be interpreted as a sum of exponential with a distribution β. From this we can calculate the average lifetime $< \tau >$

$$< \tau >= \frac{\tau_c}{\beta} \Gamma \left(\frac{1}{\beta} \right) \tag{2.4}$$

where Γ is the gamma function. This as the advantage of indicating how close to a real exponential decay the signal is. And it gives one parameter to compare $< \tau >$. This method is not widely used in the perovskite field but it should. The justification is that the perovskite layer is not homogeneous, especially mixed cation and quasi 2D perovskite. Stretch exponential are especially useful in such case because it can capture a distribution of emission very easily compared to an arbitrary sum of exponential functions.

The limit of the photoluminescence decay resides in its essence. It only measures radiative recombination. However, as mentioned previously, the radiative process is only one process of the different recombination mechanisms a photo carrier can undergo. All non-radiative pathways are invisible. To assess the latter, another time-resolved technique can be used: transient absorption spectroscopy(TA).

2.3 Transient absorption spectroscopy

This method is different from other optical ones as it is a so-called pump-probe technique. This means it uses two different beams to function: a pump, or excitation,is a monochromatic beam from a pulsed laser, and a broadband probe beam from a flash lamp or a laser with the help of a broadband generating nonlinear crystal. The concept of this measurement is to take the absorption spectra of the material while being pumped to it excited state by the pump pulse. To do so, the material is excited by the pump beam and overlapped in space and time the probe beam will them measure the absorption in transmittance by changing the delay between the pump and probe arises the time resolution from femtoseconds to microseconds according to the setup.

The time frame of the experiment is defined by the type of setup used. For femtosecond resolution, the excitation and the probe are both coming from the same laser. The beam are then tuned by nonlinear optics and delay one from the other to create the time component of the experiment by changing the beam path length of the probe. Such setup will record a spectral snapshot using CCDs at different pump-probe delays up to a few nanosecond delays. For the nanosecond resolution or longer the setup is simpler as it does not need an optical delay and laser generated white light. Such a setup is exemplified in figure 2.3-2 and consists of a tunable laser for the pump and a xenon flash lamp for the probe. The signal is, usually, recorded wavelength by wavelength using a PMT. As a result, the main difference is that for a fsTA setup, spectra are recorded as the nsTA decays are measured.

By calculating the difference in absorption with the pump and without the pump, a differential absorption spectrum(ΔA) is created. An increase in the amount of probe light detected under excitation will result in a negative signal and an decrease in a positive one. This yield in different types of signal measurable being: ground state bleaching(GSB), excited state absorption(ESA), and stimulated emission(SE).
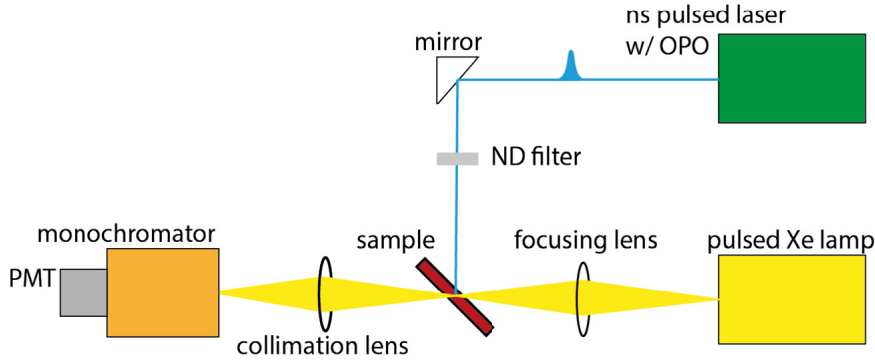
Figure 2.3-2: Nanosecond transient absorption setup diagram

$$\Delta A = \frac{\text{pump on} - A_{\text{pump off}}}{A_{\text{pump off}}} \qquad (2.5)$$

Following the dynamics of the TA spectra, we can measure the lifetime of the excited state species, and given the correct time resolution, follow the dynamic process such as energy transfer, carrier recombination,etc. All these phenomena happen at the same time, overlapping each other. The measured signal being the sum of all these overlapping signals, it results that the analysis of a transient absorption spectrum is a complex task.

2.3.1 Global analysis

The procedure to interpret the TA data is called global analysis(or global fit) and consists in using one set of parameters to describe the whole dataset. The TA datasets take the shape of a 2D matrix $M(\lambda, t)$ where λ and t are, respectively, the wavelength and time and are independent variables. The spectral variables λ describe the spectral shape and t the time evolution of the spectra. As a result the dataset can be represented as:

$$M(\lambda, t) = \sum_{i=1}^{n} S_i(\lambda) \cdot D_i(t) \qquad (2.6)$$

Where n is the total number component. The dataset can be interpreted either spec-

trally or kinetically by modeling either $S_i(\lambda)$ or $D_i(t)$ respectively. This reflects the two ways of constructing the dataset. As previously mentioned one can either measure the spectra at different times or measure decays at different wavelength. Both methods yield the same measurement. The modeling of the dynamics is preferred as it is the easiest. Usually a simple model involving a first or second-order decay is enough result in a system of linear differential equation to solve. The solution of this system is a sum of exponential eventually convoluted with a Gaussian to take into account the initial rise of the excitation pulse. The convolution is required for early time phenomena happening close to the excitation time. Otherwise, it is not required. The global analysis of this system will use the time constant of each exponential as a shared parameter and will thus be the same for each wavelength. The amplitude of each exponential will be the variable to optimise. For a simple single exponential model, the whole dataset will be modeled by the following equation:

$$\Delta A(\lambda, t) = \sum_{i=1}^{n} a_i(\lambda) \cdot e^{\frac{t}{\tau}} + c_0 \tag{2.7}$$

Where $\Delta A(\lambda, t)$ is the dataset, $a_i(\lambda)$ is the amplitude for each wavelength, τ is the shared time constant and c_0 a constant representing the baseline. The result of the analysis will be a plot if $a_i(\lambda)$ that should mimic the global spectral shape of the experiment as in figure S3.2-5.

As a summary, the procedure to perform a global analysis is : *I)* find a suitable model. *II)* Test the said model on selected data points(2-3 wavelengths. *III)* If the test is a good fit, use the resulting time constant as a shared parameter for the entire dataset. *IV)* Performe said fit and extract the different amplitudes. These amplitude for the so-called decay associated spectra and by plotting them against wavelengths. If multiple exponential are used, each parameter will fit part of the global spectrum. Summing all the amplitudes will yield the global TA spectral shape.

2.3.2 Kinetic models

The choice of the model is core to the analysis and to what it will yield. Indeed, the simpler the model the lesser information can be extracted. However a more complex model requires more data to crunch. Specifically, for TA data, the simple sum of exponential is already quite good. With it, the early and late phenomenon can be fitted and their relative population can be assessed. Different process can be spectrally convoluted. However, such a model will not say anything about the physical meaning of the resulting parameter.

A more complex, but also physically meaning full one can be constructed from basic principles and by looking at the population evolution of different spices considering their recombination and interactions. Such a construction is call a kinetic rate model and is a system of partial differential equations, one for each species modeled. For a simple electron and hole and trapped electron model, such a system will be:[59–61]

$$\frac{dn_e}{dt} = G_c - k_2 n_e(n_h + p_0) - k_T n_e(N_T - n_T) \tag{2.8}$$

$$\frac{dn_h}{dt} = -G_c + k_2 n_c(n_h + p_0) + k_D n_t(n_h - p_0) \tag{2.9}$$

$$\frac{dn_t}{dt} = k_T n_e(N_T - n_T) - k_D n_t(n_h + p_0) \tag{2.10}$$

Where n_e, n_h and n_t are the electron, hole and trapped electron populations, respectively. N_T is the global trap density, k_T and k_D are the trapping and detraping rate, k_2 the radiative recombination and p_0 the initial population of holes. This type of model can be tuned to include or exclude any process but requires more that just TA data. Indeed to be able to converge such a complex picture, another dimension is necessary. This usually comes in the form of a power dependence measurement. Having TA dataset at different excitation density for the same material and feeding this into the global analysis, one can then extract the population evolution of each carrier as well as the different rate. Generally speaking, for this method to work, at least 2 to 3 orders of magnitude

in the excitation density is required. Indeed, the different excitation regimes have to be screened as the different process will be prevalent at different regimes. For example, trap-mediated pathways will be preferred at low excitation density and radiative one for higher density. This kind of models are very useful because very versatile. The model can be changed to suit any experiment looking at population evolution and is not reserved for TA experiments.

In annexes, section S6.1 a selection of data analysis and visualisation script I've written are presented

2.4 Conclusion

In this chapter we saw the main method to investigate the inner working of matter. By means of state of the art optical measurement we are able to probe the evolution of photo generated carriers in semiconductors from the moment they are generated up to the moment they recombined. We are able to assess by which process this happens and hopefully take advantage of it for a smart design of optoelectronic devices.

CHAPTER 3

Low-Dimensional Perovskites

As already discussed in section 1.4.2, 2D perovskites are nowadays captivating a growing interest. As quantum wells (QWs), they sustain stable excitons with relatively high Coulomb energy (Eb =400-500 meV), due to quantum and dielectric confinement induced by the dielectric mismatch between the organic and inorganic moieties.[62–65] As a result of the strengthened exciton confinement, bright photoluminescence (PL), scintillation activity and strong optical non-linearity have been observed in addition to exciting physical properties such as a gigantic Rashba splitting, and strong exciton-polariton interactions.[66–69] Assessing the nature of the electronic species in close relation to the chemical structure of 2DP is of utmost interest with profound implications for excitonic devices such as quantum well modulators, light-emitting devices, lasers, etc.

In this chapter, the design and properties of new cations for 2D perovskite will be discussed as well as an indepth analysis of the excited state species of one of them.

3.1 Fashioning Fluorous Organic Spacers for Tunable and Stable Layered Hybrid Perovskites

This is part of a work published with the same title in Chem. Mater.2018, 30, 8211-8220.[70] Dr. Garcia-Benito took care of all the sample preparation and the

gerenal discussion and Dr. Quarti the computation and general discussion. I contributed the optical measurements, analysis and general discussion.

In this work, we synthesize a new family of fluorous ammonium cations as organic spacers to create new stable 2D HP. Fluorous compounds are characterized by the presence of highly fluorinated, saturated molecular fragments, usually linear medium-sized perfluoroalkyl chains.[71] They show distinct properties compared to their fully hydrocarbon-, mono/ polyfluorinated-, or trifluoromethylated analogues. In particular, their simultaneously hydrophobic and lipophobic behavior is utilized in a variety of applications, spanning from catalysis to medicine.[72] Whereas 2D HPs featuringfluorinated alkyl or aryl ammonium cations as organic spacers have been previously proposed[73–76] (i.e., using 2-fluoroethy-lammonium ($FC_2H_4NH_3^+$),[77] perovskite materials incorporating fluorous ammonium are virtually unknown. The presence of the fluorous cations in the resulting 2D perovskite can impart an additional water-repellent character and superior stability with respect to fully hydrocarbon-based cations used so far.[78] In this work, we design four new fluorous ammonium cations having different shapes, that is, from branched to linear, fluorine loading, and length (varying the alkylene spacer) used to develop stable fluorous 2D HPs thin films with remarkable hydrophobic character. We observe that the systematic modification of the fluorous cation dimension and molecular structure impacts on the optoelectronic properties of the 2D HPs. The length of the cation tunes those properties that are paramount for optoelectronic device optimization such as the band gap and exciton binding energy, which varies from 420 to 130 meV.[79,80] In addition, the longest cation boosts the thin film water-repellent character leading to a superior hydrophobicity with respect to standard 3D hybrid perovskite.[81,82] The fluorous 2D HPs exhibit a remarkably high moisture resistance, that kept intact their structural and optical properties upon aging for one month in an ambient atmosphere (RH = 40%).
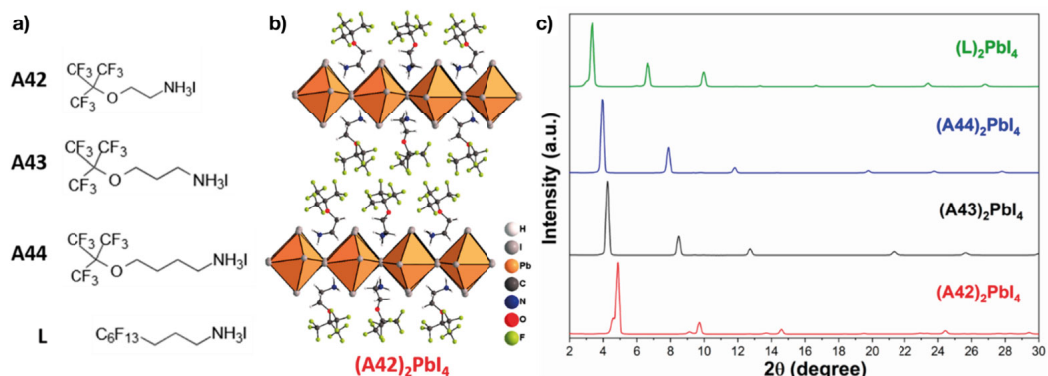
Figure 3.1-1: (a) Molecular structure and abbreviated name of the studied fluorous cations. (b) Schematic structure of 2D HP with A42 as the organic spacer between the inorganic PbI6 layer. (c) Out of plane X-ray diffraction (XRD) patterns of the $(A42)_2PbI_4$, $(A43)_2PbI_4$, $(A44)_2PbI_4$, and $(L)_2PbI_4$ in thin films

3.1.1   Structural properties

The crystalline structure at room temperature of our new fluorous 2D HPs has been unveiled by combining X-ray diffraction (XRD) analyses on both thin films and single crystal. The investigated thin films display an XRD pattern rich in the low angle region, as shown in Figure 3.1-1c, indicative of a n = 1 2D HP structure.[79,83,84] More in details, the patterns are dominated by the equally spaced (00l) reflections, peaking at 4.9°,4.3°,3.9°,and 3.4° for $(A42)_2PbI_4$, $(A43)_2PbI_4$, $(A44)_2PbI_4$, and $(L)_2PbI_4$, respectively. The shift of the peak is due to the larger distance between the inorganic planes, as the cation size increases. The reflections of the other (hkl) planes are strongly suppressed, confirming the remarkable preferred orientation of the inorganic planes, aligning parallel to the substrate.[79,84] From those reflections, we can calculate the distance between the discrete perovskite inorganic layers ranging from 18.6 to 27.1 Å, depending on the size of the fluorous cations (see SI Table S1). It is fair noticing indeed that the derived interplane distances (among the inorganic layers) parallel the length of the organic cations following the same trend which increases from A42 to A44.

3.1.2 Optical characterisation
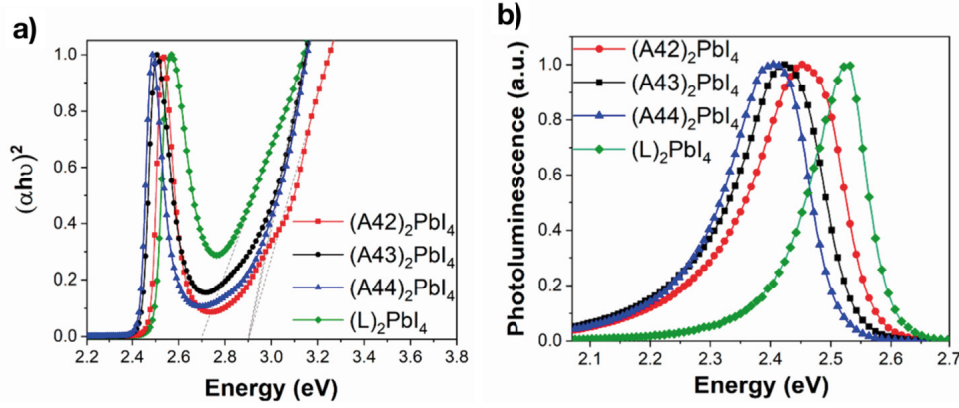
Figure 3.1-2: (a) UV-vis absorption spectrum of the four investigated 2D HPs. The plot reports also the electronic band gap, as extrapolated from Tauc linear fit (gray dashed lines). (b) Normalized PL spectra ($\lambda_{excitation}$ = 367 nm) of $(A42)_2PbI_4$, $(A43)_2PbI_4$, $(A44)_2PbI_4$, and $(L)_2PbI_4$ in thin films at room temperature.

To evaluate the optical properties of the 2D HPs, we have first measured the UV-VIS absorption spectrum and estimated the material band gap through a Tauc plot analysis (see Figure 3.1-2a). For all investigated systems, the absorption spectra reveal a sharp and intense peak at around ~2.5-2.6 eV, assigned to the excitonic feature, as typical for 2D HPs,[63,71,85] followed by a continuum absorption signal, related to direct band-to-band transitions. In the case of the branched systems, the band gap is 2.9 eV, almost independent from the structure of the cation, whereas the exciton binding energy (around 400 meV) experiences only a very small increase going from the shorter A42 cation to the longer A43 and A44, see Table 3.1-1. Conversely, the absorption of the

	$(A42)_2PbI_4$	$(A43)_2PbI_4$	$(A44)_2PbI_4$	$(L)_2PbI_4$
Eb (meV)	380	393	420	430
Bandgap Tauc (eV)	2.9	2.9	2.9	2.7

Table 3.1-1: Exciton Binding Energy (Eb) and Band Gap of $(A42)_2PbI_4$, $(A43)_2PbI_4$, $(A44)_2PbI_4$, and $(L)_2PbI_4$ Derived from the Tauc-Plot of Figure 3.1-2 Compared

$(L)_2PbI_4$ compound shows a blue-shifted excitonic peak along with a red-shifted band edge, with respect to the branched one, giving an estimation of the band gap of 2.7 eV. Notably, in this case, the exciton binding energy reduces to around 300 meV. Figure 3.1-2b shows the photoluminescence (PL) spectra for the different compounds. First, it is worth pointing out that the materials derived from the branched family of cations (A42, A43, and A44) show a main emission peak that experiences a red shift with increasing cation length, matching the shift of the excitonic peak in absorption, whereas a blue-shifted emission is consistently observed for the L-based material (see SI Table S3.1-2). This enables us to conclude that the emission is excitonic in nature, due to the high oscillator strength of the quantum confined exciton as already observed for different 2D HP systems.[86,87] The PL decays at peak position are displayed in sumplemetary Figure S3.1-1 and Table S3.1-1. The decay can be fitted with a two-exponential function giving a fast time constant of $\tau_1 = 15$ ns for the branched cations (A42, A43, A44) and $\tau_1 = 6.9$ ns for the linear one-based 2D HPs and a longer living tail. The fastdecay,which dominates in amplitude, can be associated with excitonic recombination, in line with literature reports,[88,89] whereas the tail can be related to trap-mediated recombination. From a closer inspection of the PL spectra, we notice that the bandwidth of the PL spectra is different between the branched and the linear cations (SI Figure S3.1-2), much sharper for the last. It exhibits a Lorentz shape with a bandwidth (fwhm) of 0.11 eV, a signature of purely excitonic emission. For the branched cations, a broader emission of width ~0.15-0.17 eV is observed, with a tail extended more to the red. A simple two-Gaussian fit of the inhomogeneous broadening of the PL spectrum reveals the presence of a second emission peak at room temperature, red- shifted with respect to the main exciton peak. The origin of this secondary signal can be potentially related to the contribution of trap-assisted recombination from excitons trapped in defects, generated from strong exciton-lattice coupling, common in metal halides.[90] To further corroborate the observed trend, we also examined the absorption and emission properties of materials obtained using the branched cation A43 and the linear one L mixed with lead bromide instead of

lead iodide as inorganic component, resulting in the formation of an R_2PbBr_4 structure. The substitution of iodine with bromine results in a widening of the band gap manifested as a blue shift of the absorption spectrum, as known for Br- based perovskites.[91−93] Even in the case of $(L)_2PbBr_4$ we could observe a sharper excitonic emission with bandwidth of 0.29 eV, compare to 0.39 eV for $(A43)_2PbBr_4$ (see SI Figure S3.1-3).

3.1.3   Stability
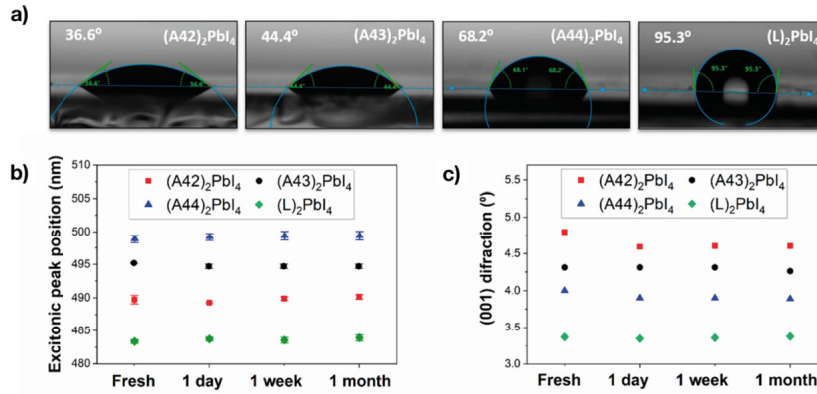
Figure 3.1-3: Illustration of the contact angle formed by a water drop on $(A42)_2PbI_4$, $(A43)_2PbI_4$, $(A44)_2PbI_4$ and $(L)_2PbI_4$ in thin films (36.6°, 44.4° 68.2°, 95.3° respectively); Stability study of the 2D IIPs in thin film stored in air: (b) Position of the maximum absorption peak, (c) Position of (001) X-ray diffraction, after the preparation, after 1 day, 1 week and one month. values

As stated in the introduction, we designed a new family of fluorous 2D HP with the final aim to increase the water-repellent character of the ultimate perovskite thin film. To verify the robustness upon water exposure and the hydrophobic character of the 2D HP, we carried out contact angle measurements using water. The results are displayed in Figure 3.1-3a. On the one hand, the 2D HPs based on L cation exhibits a clear hydrophobic character, in line with the typical behavior of materials with highly ordered linear perfluoroalkyl chains at the outermost surface.[94] On the other hand, for materials based on A4n salts, the contact angle increases with the length of the alkylene linker

present in the branched organic cations (from A42 to A44), but remains $<90°$. This is not totally unexpected, because of the higher mobility of the branched fluorinated segment with respect to the linear one, which provides frustrated packing and a reduced water shielding effect.[95] Then, to test the long-term stability, we evaluated the variation of the optical and structural properties of the 2D HPs thin films upon exposing the samples in air (relative humidity = 40%) for more than one month. Figure 3.1-3b,c shows the data collected by monitoring the R_2PbI_4 maxima absorption position and (001) diffraction position at different time exposure. As seen in Figure 3.1-3b, the excitonic peak remains at the same position over time for all 2D HPs investigated. In addition, no distinct differences were observed in the position of the (001) diffraction peak of the 2D HPs stored in air, after the different times of exposure (Figure 3.1-3c). This provides compelling evidence of the high degree of stability and resistance of the fluorous perovskite films in ambient conditions.

3.1.4 Conclusion

In this work, we have synthesized a new series of fluorous organic cations and shaped them to form tunable and stable 2D HPs. The fluorous cations impart extreme stability of the 2D HPs upon exposure to atmosphere conditions and enhance the water-repellent character of the 2D HP surface. The shorter branched and the longer linear fluorous cations have been designed as the organic barriers for the fluorous 2D HPs. The size and shape of the organic cation modulate the 2D HP structure, electronic, and optical properties. Despite the fact that the organic spacers do not participate in the electronic structure, they influence the perovskites electronic structure via an indirect structural effect on the inorganic sheet, inducing a variation of the band gap and exciton binding energy. These local distortions affect the binding energy more than the local dielectric mismatch. The longer the cation, the smaller the band gap. This results in a lower exciton binding energy and smaller effective masses, pointing toward a better transport for the elongated fluorous chains. This new family of stable 2D HP does not only shows the large

extent of tuning the optoelectronic properties by simple shaping of the fluorous organic spacer, but, importantly, it shows a remarkably high structural stability kept intact even upon a one-month air exposure. Overall, these attributes make this fluorous 2D HP an exciting candidate for stable perovskite optoelectronics.

3.2 Spatial Charge Separation as the Origin of Anomalous Stark Effect in Fluorous Two-Dimensional Hybrid Perovskites

This work was published with the same title in Adv. Funct. Mater.2020, 30, 2000228.[96] A special mention to Dr. Bouduban for the electro-absorption measurement and contributing to general discussion and Dr. Quarti for computation and general discussion. I led the work, provided the optical and TA data as well as the general analysis and discussion

In this work, we provide a comprehensive analysis views by focusing on a newly synthesized fluorine-containing 2DP of high interest for stable and efficient perovskite devices.[48, 70] Field-induced changes in the linear optical absorption reveal a combination of first- and second-derivative contributions at the exciton resonance. While the first-derivative signal (red shifting) results from QCSE, the second-derivative contribution is ascribed to charge pairs with spatially separated electrons and holes, as observed in other layered QW structures.[97, 98] Notably, upon the generation of charges by the impulsive light excitation, a Stark effect is also observed due to exciton screening, lasting for microseconds. Ab initio computational modeling suggests that the combined effects of structural and electrostatic disorders induced by the fluorinated cations stabilize long-lived weakly correlated charge pairs in these 2DP.

3.2.1 Material properties

Figure 3.2-1A shows the structure of the fluorous-2DP ($(A43)_2PbI_4$ hereafter), where a bulky fluorous cation (A43 = $(CF_3)_3CO(CH_2)_3NH_3+$) intercalate in between single in-
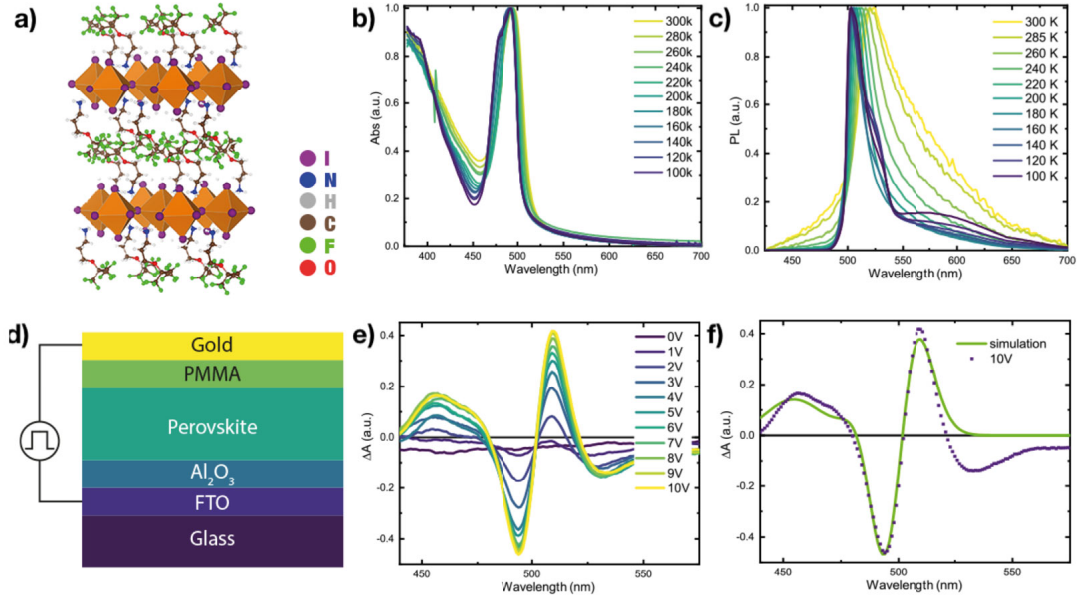
Figure 3.2-1: a) Cartoon showing the structure of $(A43)_2PbI_4$. b,c) Linear absorption and photoluminescence spectra (upon exciting at 420 nm) of $(A43)_2PbI_4$ versus temperature as indicated in the legend. d) Sketch of the device employed in Electroabsorption (EA) experiments done at Room Temperature. e) EA spectra of the $(A43)_2PbI_4$ device at different biases. f) EA spectra at 10V with a simulation composed of a linear combination of derivatives of the absorption bands.

organic layers adopting a pure 2DP $(A43)_2PbI_4$ structure. This is an attractive arrangement because of the resulting strong hydrophobic character, thereby creating a barrier layer against water penetration and allowing efficient and stable 2D/3D perovskite solar cells.[47,57,99] In addition, this class of materials is also of high interest for their exceptional ease of tuning the exciton binding energy by fashioning the size and the length of the fluorous cation.[70] The absorption profile of $(A43)_2PbI_4$ films (Figure 3.2-1B) shows a strong excitonic peak at the band edge at 495 nm (2.5eV), which sharpens going down in temperature. As discussed by Neutzer et al., a clear second peak is observed at low temperature, in this case at 498 nm, separated by a 51 meV energy gap to the main exciton band.[100] This is the fingerprint of a hidden exciton characterized by a different coupling to the lattice.[101] From Tauc Plot analysis (Figure S3.2-1), the electronic band-to-band

transition is estimated around 427 nm (2.9 eV), which indicates an exciton binding energy of around 400 meV. Similarly, the emission shows a single peak, excitonic in nature, which gets narrower going down in temperature (see PL spectra in Figure 3.1C). In addition, a broader in-gap band can also be identified at low temperature, which we tentatively assign to the formation of local defects acting as color centers.[90] We also note the absence of a shift (or discontinuity) of the band edge with temperature, indicative of no phase transition in the temperature range investigated. This contrasts with standard 2DP (see for instance, butyl ammonium based 2DP used as a reference, reported in Figure S3.2-2). The modeled absorption of $(A43)_2PbI_4$, reconstructed following the model by Katoor et al., i.e. by using a linear combination of Gaussian curves to simulate the excitonic transitions as well as the continuum, is shown in Figure S3.2-1.[102]

3.2.2 Electro-absorption

To get a deeper understanding of the nature of the electronic excitation, we measured the EA spectrum (Figure 3.2-1E) of a $(A43)_2PbI_4$ perovskite film in a device configuration, as shown in the cartoon at Figure 3.1D done at Room Temperature. Figure 3.1E displays the EA signal at different bias applied perpendicular to the film substrate. In light of the strong crystalline orientation of the thin film lying parallel to the substrate, this should mainly correspond to the direction perpendicular to the inorganic PbI_4 sheets within the film, thus along the axis of confinement (see XRD in Figure S3.2-3). The EA spectrum exhibits a modulation consisting of a negative peak at 495 nm and a positive peak at 508 nm, respectively, along with two sidebands: one positive at 455 nm and one negative at 540 nm. For quantum-confined semiconductors, the EA spectrum can be modeled in the framework of Stark's theory.[103] More in details, the EA can be decomposed into a linear combination of first- and second-derivative contributions to the linear absorption spectrum, whose relative amplitudes provide insight into the type of carriers subjected to the perturbation.

Interestingly, in this case, the modulation can be well simulated with a 2:1 ratio of the

1st and 2nd derivatives of the excitonic peak (see Figure 3.2-1F). Note that the fit is poor in the low-energy part of the spectrum. In this region below the gap, a broad, featureless negative signal appears which is related to mid-gap states in 2D perovskite, in agreement with what is already discussed in Amerling et al.,[68] which the derivative fit does not consider. The first-derivative contribution is assigned to QCSE (red shifting), while the second derivative indicates the formation of screened electron-hole pairs. In addition, its shape calls for loosely bound electron-hole pairs with a predominant charge-transfer character (CTC). This suggests that electrons and holes can separate in the $[PbI_6]^{4-}$ inorganic wells, in contrast to the common classification on 2DP.[104]

3.2.3   Nanosecond transient absorption
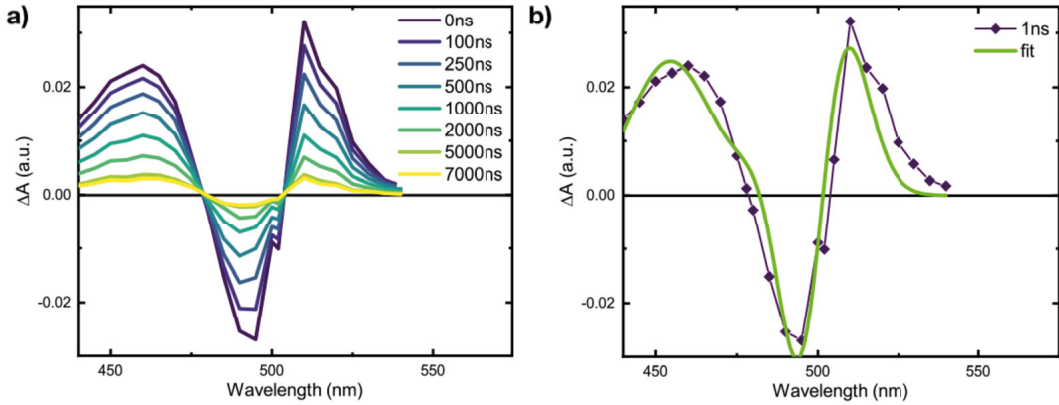
Figure 3.2-2: a) ns Transient Absorption (TA) spectra at selected delays (as indicated in the legend) for the $(A43)_2PbI_4$ thin film upon excitation at 420 nm, carrier density 10^{18} cm^{-3}. b) nsTA signal at 1 ns probe delay with the simulated EA spectra (as in Figure 3.1f).

Time-resolved transient absorption measurements in the nanosecond domain have been performed to elucidate the dynamic response of the system upon impulsive excitation, which generates a high carrier density of around 10^{18} cm^{-3}. We show in Figure 3.2-2a the ns Transient Absorption (TA) spectra of the $(A43)_2PbI_4$ thin film at selected pump-probe delays. The spectra exhibit an oscillatory feature with two positive peaks at

460 nm and 510 nm as well as a negative peak at 495 nm. It is apparent that the spectral evolution of the nsTA resembles a combination of derivative-like features with two zero-crossing points that do not move in time. They all exhibit the same decay, showing a faster component with a time constant of τ_1=930 ns and a second τ_2 extending beyond our temporal window.

To further analyze the spectral behavior and retrieve the associated time constant, we fitted the whole spectral evolution using a Global Analysis (GA) procedure (Figure S3.2-5). The three bands have the same dynamics, suggesting that one process is responsible for the whole spectral evolution. Figure 3.2-2b shows a cut of the nsTA signal at 1 ns delay superimposed on the linear fit of the EA data (Figure 3.1f). Notably, for nsTA, no field is externally applied, thus the perturbation related to a long-living photoinduced Stark Effect in this case only arises upon illumination and consequent creation of long-lived charge pairs. It is worth pointing out that this observation differs from previous reports on alkylammonium-based 2DPs (e.g. (C_6PbI_4) containing hexylammonium cations), where only a first-derivative contribution in the EA spectra was reported and associated with strongly bound excitons.[105] In our case, despite the very similar exciton binding energy (400 meV in $(A43)_2PbI_4$ versus 360 meV in C_6PbI_4), an additional contribution from long-lived, loosely bound, charge pairs is observed.

3.2.4   Computational investigation

Since the physical origin of the screening of the correlated electron-hole pairs is inherent to the detailed chemical composition of the system, we have performed periodic Density Functional Theory (DFT) calculations using the planewave/ pseudopotential formalism, as implemented in the Quantum Espresso package (see Computational Methods for a detailed description of the approach).[106] We performed preliminary calculations on these systems considering the crystalline models reported in literature.[48,107]

The corresponding partial Density Of States pDOS of $(A43)_2PbI_4$ is reported in Figure S3.2-6 and shows somewhat larger band gap compared to reference $(BUA)_2PbI_4$, a

fact that has been directly related to larger rotation of the PbI_6 octahedra in the former system, as discussed in reference.[70] However, the qualitative trend in the pDOS is similar, consistent with the fact that the models from the XRD experimental structures share similar Pb-I bond length and structure. Most notably, we notice that both the A43 and BUA present a type I electronic alignment between the inorganic and organic frame, hence with the frontier levels of the former embedded in the frontier levels of the latter component. So, for both systems we can exclude direct perturbation of the PbI_4 electronic structure due to the cation, as manifested by the absence of intragap trap states. Rather, the impact of the organic cations is twofold: (*I*) a (indirect) structural effect. As well-known from literature, the organic cation can impact on the electronic structure of the inorganic semiconducting component through distortion of the octahedral lattice.[108–110] This is expected to be particularly important here as a result of the bulky character of the $C-(CF_3)_3$ fluorous spacers (see Figure 3.1a). (*II*) a (direct) electrostatic effect. The decoration of the chains with strongly electronegative fluorine atoms pointing away from the inorganic lattice is expected to yield a sizeable electrostatic potential affecting the energy landscape explored by holes and electrons residing within the PbI_4 layers. To address the possible role of an indirect structural effect, we performed frozen-glass simulations as follows. We first carried out ab-initio Born-Oppenheimer molecular dynamics (BOMD) simulations at high temperature (600 K, see Method Section in the SI for details), so as to widely explore the ground-state potential energy surface. Then, we randomly picked up forty structures from the MD trajectory, which were fully minimized (at 0 K). Using such a numerical thermal annealing protocol, we do not allow the system to reach the absolute minimum energy configuration, but rather freeze the system into a set of local minima on the ground-state potential energy surface.[111–114]

In Figure 3.2-3a, we compare the lead-iodine radial distribution function for the so-prepared frozen glasses of the fluorous-based perovskite, compared to butylammonium (named BUA after-on) taken as the reference material. BUA shows the usual distribution of bond lengths among the inorganic atoms,[115,116] with the first peak associated to

the lead-to-iodine distance, peaking at the equilibrium distance of 3.2 Å(full width half maximum, FWHM is 0.12 Å). Most interestingly, in the case of the fluorous cations, the Pb-I distance, while being centered at the same value, shows a significantly broader distribution (FWHM of 0.18 Å). In particular, configurations with lead-to-iodine distances in excess of 3.75 Å, hence 0.55 Ålonger than the typical Pb-I distances are now accessible. Thus, compared to BUA, the bulky fluorous cations distort more severely the PbI_4 inorganic structure. It is also worth pointing out that the single crystal structure revealed a triclinic symmetry in contrast to the monoclinic structure for the most common 2D perovskite, already indicating a more distorted structure. Most noteworthy, previous literature in the field already pointed out the importance of structural dynamics and local distortions in affecting the electronic features of hybrid halide perovskites, as related, for instance, to the variation of the optical properties with temperature,[116] as first step towards the formation of point defects,[117] to explain less effective electron-phonon scattering events.[118] We will later on discuss the effect of the structural distortions of the $(A43)_2PbI_4$ material, as reported in Figure 3.2-3.

With the aim of characterizing possible structural deformations indirectly induced by the organic cation, as discussed above, we computed the lead-iodine radial distribution function for the fluorous-based perovskites under study and for a reference alkyl-based compound (butylammonium-), as reported in Figure 3.2-3a. We now turn to the collective electrostatic effects of the cations on the energy of the frontier crystalline orbitals. In 2D slabs, an extended monolayer of oriented dipoles produces a jump (ΔE) in electrostatic potential with respect to vacuum, which can be cast in terms of the component of the dipole moment orthogonal to the slab surface (μ_z) per unit area (A) via the Helmholtz relation:

$$\Delta E = \frac{-\mu_z}{\epsilon_0 A} \tag{3.1}$$

(where ϵ_0 is the vacuum dielectric constant). As shown in Figure 3.2-3B and in agreement with our expectations, the fluorinated side group of the Fluorous organic cation (A43,
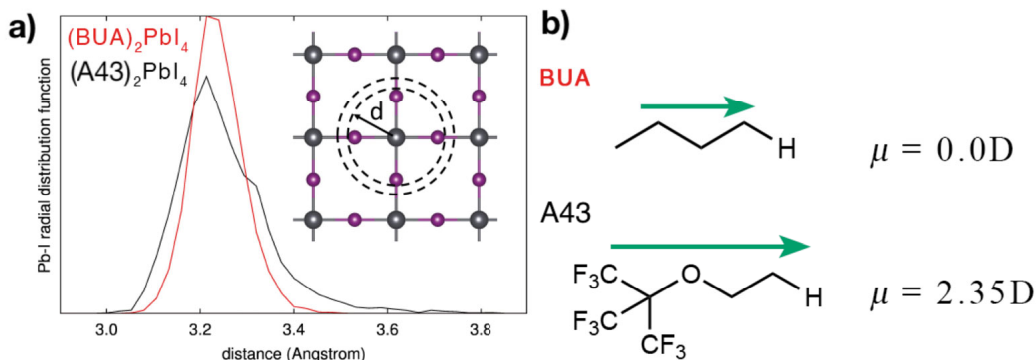
Figure 3.2-3: Results of frozen glass simulation. a) Lead-Iodide radial distribution function computed for $(A43)_2PbI_4$ and $(BUA)_2PbI_4$. b) Dipole moment for BUA and A43 cations, with the NH_3^+ group substituted by a hydrogen atom to preserve the charge neutrality.

see Figure 3.2-3A) features a larger dipole than the corresponding hydrocarbon chain of BUA. Here, the calculations are performed by substituting NH_3^+ with H, as dipoles of charged molecules are ill-defined (notably, similar results are obtained considering CH_3 or NH_2, terminal groups, see Supporting Information). This is corroborated by the DFT electronic structure calculations reported in Figure 3.2-4A, showing an upshift of the electrostatic potential in the vacuum region by 1eV when going from $(BUA)_2PbI_4$ to $(A43)_2PbI_4$ (in line with the difference in dipole moments in Figure 3.2-3 and with Eq. 3.1). Correspondingly, the valence and conduction band edges of $(A43)_2PbI_4$ get stabilized by the same ΔE value, as shown in Figure 3.2-4B, with namely larger ionization potential (IP) for $(A43)_2PbI_4$, compared to the reference $(BUA)_2PbI_4$

The combination of the electrostatic and structural distortion effects discussed above provides a simple rationale for the formation of charge-separated states in $(A43)_2PbI_4$. Inspired by the results in Figure 3.2-3, namely, that the $(A43)_2PbI_4$ can sustain significant distortions of the Pb-I lattice, we propose that iodine atoms are more labile in the fluorinated compounds and, to evaluate the effects of such structural distortions on the electronic structure of the material, we propose that iodine atoms are more labile in the fluorinated compounds. We thus performed 'pull-out' numerical experiments, where one
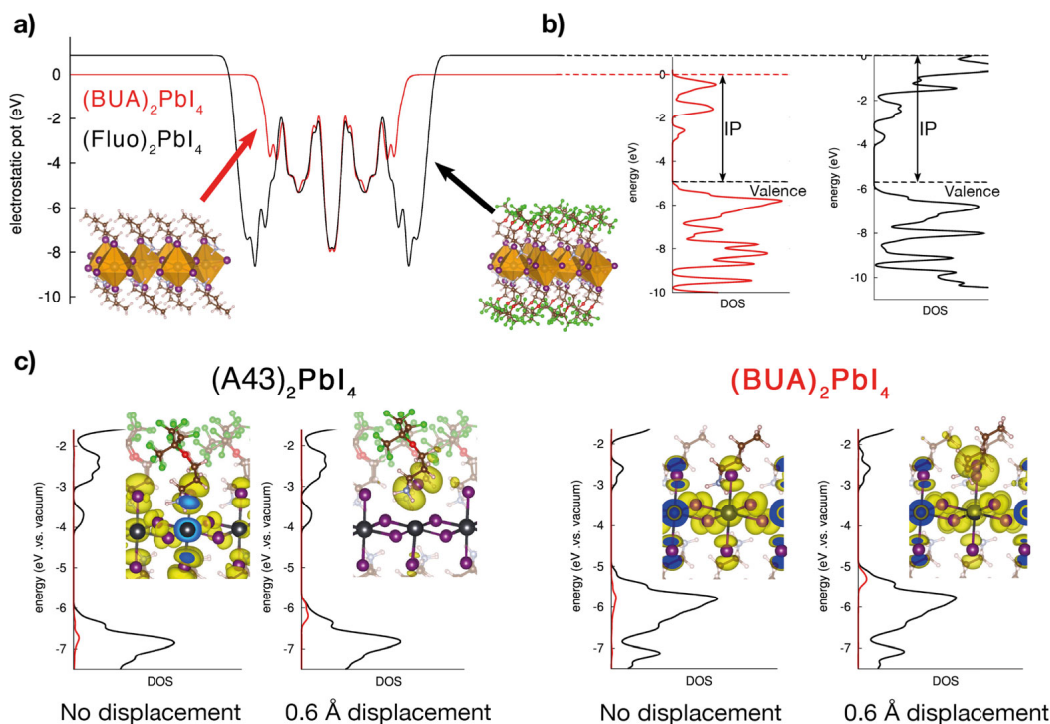
Figure 3.2-4: a) Electrostatic potential along the thickness of $(BUA)_2PbI_4$ and $(A43)_2PbI_4$ slabs; b) Partial density of electronic states (pDOS) for the two materials referred to the electrostatic potential in a. The ionization potential (IP) is indicated. c) Total density of state (black curve) and density of state (red line) of one iodine which has been pulled out by 0.6 Å(vide infra) with respect to the central PbI_4 plane. The spatial localization of the valence band edge orbital is reported in the inset.

iodine atom is increasingly dragged away from the inorganic lattice by the closest organic cation. Considering a displacement of 0.6 Å, which is on par with the range of values predicted by MD simulations in Figure 3.2-3A, for the apical iodine A43-cation , we find that gap states located around the labile iodine ions form just above the valence band edge in the case of $(A43)_2PbI_4$ (see Figure 3.2-4C). We stress that it is the combined effect of the increased structural distortion prompted by the bulky side groups together with the overall downshift of the delocalized band states driven by fluorine-induced electrostatic effects that expels these shallow trap states from the band edge into gaps. Such localized trap states do not show up in similar simulations performed for $(BUA)_2PbI_4$,

at least, considering 0.6 Ådisplacement. In Figure S3.2-7 and SI8, we report both the partial Density of States and shape of the highest occupied orbital for $(BUA)_2PbI_4$ and $(A43)_2PbI_4$ materials, with increasing pull-out displacements ranging from 0.15 Å to 0.6 Å.

For the case of $(A43)_2PbI_4$, the appearance of shallow trap states, fully localized on the apical iodine interested in the pull-out is already evident at 0.45 Å, while for the $(BUA)_2PbI_4$, these states still lie below the delocalized valence band maximum even for displacement 0.6 Å. Thus, following Figure 3.2-3A, we propose that the frozen glass arrangement of the side chains in the fluorous 2D perovskites can stabilize a broad range of configurations that differ by the relative displacement of some axial iodines with respect to the equatorial lead-iodine layer. Such configurations would support electron-hole pair excitations with spatially separated wave functions, explaining their ionic (CT) character as revealed by EA as well as their long lifetimes measured by nsTA. We expect the spatial distribution of axial iodines to extend continuously from their crystalline equilibrium position up to full separation with respect to the inner layer, with the corresponding formation of electronic excitation going from confined excitonic states for small displacements to poorly overlapping electron-hole pairs in the limiting case of halide vacancies/interstitial Frenkel defects.[90] This seems to be corroborated by the presence of the broad 600 nm emission in Figure 3.1C.

The combination of the electrostatic and structural distortion effects discussed above provides a simple rationale for the formation of charge-separated states in $(A43)_2PbI_4$. Indeed, the larger structural flexibility of the fluorinated layered perovskite goes together with stronger electrostatic effect imposed by the larger molecular dipoles, in the normal direction to the inorganic PbI_4 layer, as shown in Figure 3.2-4A,B. In this frame, we propose that structural distortions of the Pb-I lattice along the direction normal to the inorganic plane, hence in the direction of the strong variations of the electrostatic landscape in Figure 3.2-4A, strongly impacts on the formation of free carriers. Inspired by the results in Figure 3.2-3, we then performed 'pull-out' numerical experiments, where one

iodine atom is increasingly dragged away from the inorganic lattice by the closest organic cation where one iodine atom is increasingly dragged away from the inorganic lattice by the closest organic cation.

Before concluding, we briefly discuss the role of oxygen present in the A43 cation, in driving the formation of the trap states highlighted in Figure 3.2-4C. Indeed, we inherently attributed the electrostatic effect dictated A43 cation, as quantified by the larger ionization potential computed for this system, only to the terminal fluorine atoms, but oxygen can also contribute to such an effect, in light of its larger electronegativity compared to carbon. To verify this, we performed a similar pull-out computational procedure to a hypothetical new cation, having the same backbone of A43 but with all fluorine atoms substituted by hydrogens (we name this cation Fluo-H). From the pDOS in Figure S3.2-9 it is evident that the removal of fluorines in the Fluo-H cation results in 1eV up shift of the ionization potential of the perovskite, compared to the original Fluo. As result the new fluorine-free cation has ionization potential closer to the one of NBT. Consistently, inspection of the highest occupied orbital for Fluo-H reveals that this corresponds to the delocalized valence band edge and no shallow trap states form for distortions up to 0.6 Å. In other words, the removal of fluorines results in a less effective electrostatic effect on the electronic structure of the PbI_4 lattice significantly reducing the possibility of formation of shallow trap states, similar to what was found in the reference BUA material. Hence, in the perspective of cation engineering, the oxygen on the backbone of the organic molecule does not seem to be related to the optical response evinced from the EA measurements and on the long lifetime related to the A43 cation.

3.2.5 Conclusion

In conclusion, our work provides compelling evidence for the existence of long-lived weakly bound charge pairs in layered n=1 $(A43)_2PbI_4$ 2DP as evident from the anomalous second derivative shape of the field (and light) induced Stark signal. Furthermore, the optical response of this material to an impulsive optical perturbation develops over hundreds

of nanosecond timescales. This result is surprising in view of the large exciton binding energy measured in these 2D materials and highlights the role of the chemical composition of the organic components. Specifically, our atomistic calculations show that the presence of bulky $C(CF_3)_3$ groups in the fluorinated cation results in frozen-glass like structures, where the apical iodines can explore a broad range of distances from the PbI-inorganic layer, compared to standard alkylated materials. In addition, the fluorous side groups result in a sizeable electrostatically driven energy shift of the crystalline orbitals. It is the combined structural and electrostatic effects that promote the formation of spatially confined hole states at the valence band edge and stabilize loosely interacting electron-hole pairs with reduced recombination and longer lifetimes. While this feature is to our knowledge unique to Fluo-based perovskite, our study broadens the standard classification of electronic species in 2DP and opens up a way for the design of new 2DP materials. Indeed, smart design of new organic cations, characterized by bulkier/more disordered structure and/or larger molecular dipole can potentially drive the system to a larger fraction of long-living charge carriers, which are of interest for perovskite-based 2D/3D photovoltaic devices, as well as for lasers and delayed emitters. Future time resolved, power-dependent and/or field-dependent studies can further help to identify the nature of the excited species in the 2D layered perovskites family and beyond.

3.3   Conclusion

In this chapter we have started by introducing a set of new 2D perovskite made with highly fluorinated cations. It explores the mechanical as well as optical properties of this fluorinated 2d perovskite family. The fluorous cations impart extreme stability of the 2D HPs upon exposure to atmosphere conditions and enhance the water-repellent character of the 2D HP surface. The longer the cation, the smaller the band gap. This results in a lower exciton binding energy and smaller effective mass, pointing toward a better transport for the elongated fluorous chains.

Following that, the chapter moves to the extensive analysis of one member of the 2D fluorinated perovskite called A43. Here, fast spectroscopy and electro-absorption, revealing the presence of long-lasting correlated electron–hole pairs. Such states have a marked charge-transfer character, as revealed by the persistent Stark effect in the form of a second derivative in electro-absorption. This effect is the result of the unique fluorinated cation electrostatic effect as well as the steric hindrance of the later and reveals the presence of long lasting charges.

CHAPTER 4

2D/3D Perovskites Interfaces

As previously discussed, 3D perovskite solar cells are very efficient reaching 25% PCE thanks to their high carrier mobility, panchromatic absorption and low exciton binding energy.However, such high efficiency is only available for a short period of time because of degradation due to moisture, ion leakage/migration, and other. We are far from the 20-year life span of Silicon cells. The lower dimension parent of 3D perovskite, namely 2D perovskites, does not exhibit the weaknesses of 3D perovskite. The material is more robust toward humidity, does not show ion migration to name a few. But they do not have a high carrier mobility, neither a panchromatic absorption and they have a large exciton binding energy. A solar cell made only of 2D perovskites as thus an efficiency that is restricted by its characteristics.

To encompass these limits, 2D/3D mixed systems have been proposed as efficient and stable solutions by exploiting the advantage of both compound,[48, 64, 119-122] either as 2D/3D blends, where the 2D portion acts as a bulk passivant, or as 2D/3D interface, where the 2D portion functionalizes the perovskite/electron (or hole) transporting layers (ETL/HTM). These mixed solutions have propelled perovskite device performance; however, such empirical evolution of devices processing prevents a clear control of the interface properties and structure, leading to a poor "trial and error" device optimiza-

tion. A solid rationalization of the relation between interface structure and physics is thus urgently needed. How to manipulate crystal growth by material design to drive proper crystallisation of the 2D on top of the 3D, or how this impacts the interface charge carrier dynamics in terms of surface trapping, recombination, and device physics. And how the interface evolves with time and environmental conditions. All these questions are paramount issues to address. In this chapter, we will approach the crystallisation of the 2D layer on the 3D bulk as well as the evolution of the 2D/3D interface.

4.1 Crystal Orientation Drives the Interface Physics at Two/Three-Dimensional Hybrid Perovskites

This work was published with the same title in J.Phys.Chem.Lett.2019, 10, 5713-5720.[47] A special mention to my co-author, Dr. Marine Bouduban for carrying the ultrafast measurement and her general help with the discussion, Dr.Kirmani for providing the GIWAX and V.Caselli for the TRMC. I co-led the work with Dr. Bouduban, provided the PL data as well as the general analysis and discussion

Here we consider a stratified nanometer-thick 2D/3D interface based on PEA-based 2D/$Cs_{0.1}FA_{0.77}MA_{0.13}PbI_{2.59}Br_{0.41}$ perovskites, where PEAI is phenethylammonium iodide (see Figure 4.1-1), FA formamidinium, and MA methylammonium. When embedded in the device stack (i.e., between the mesoporous oxide ETL and the organic HTM on top), the 2D interface outperforms the standard 3D solar cells, pushing devices open-circuit voltage (Voc).

4.1.1 Device Characteristics

Figure 4.1-1A present a sketch of the 2D/3D perovskite solar cell architecture, highlighting the chemical structures of the PEAI and fluorinated analog, FPEAI, obtained by the para-substitution of one fluorine atom on the phenyl moiety cations. Recently, similar compounds have been used in "quasi-2D" based solar cells, showing that the fluorinated
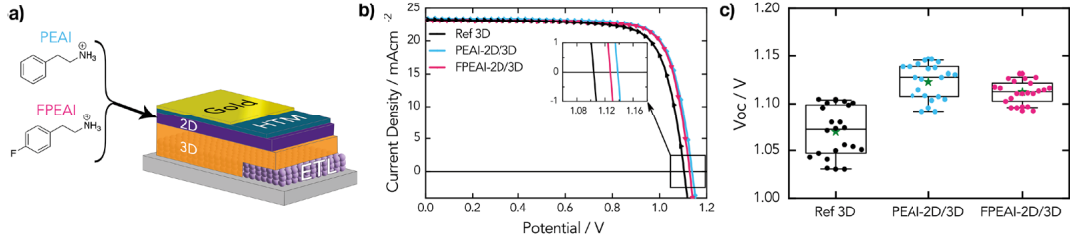
Figure 4.1-1: (a) Device stack architecture along with the chemical structure of the two cations used in the 2D layer. (b) Current-voltage characteristic comparing 2D-PEAI/3D, 2D-FPEAI/3D, and ref 3D devices. Inset: zoomed-in portion close to the Voc. (c) Voc statistics (Turkey boxplot) for the two bilayers and the reference cell over 25 devices of each.

version imparts a better alignment of the perovskite sheet stacking, which is responsible for better PCE (around 14%). In our work, we develop a stratified 2D/3D interface where the 2D portion is dynamically grown on top of the 3D portion (see Methods for details). This results in a 2D crust that is a few tens of nanometers thick (20-60 nm, see scanning electron microscopy images in Figure S4.1-2).[48,121] Device current-voltage characteristics and parameters are presented in Figure 4.1-1B and Table 4.1-1, while Figure 4.1-1C shows the V_{OC} statistics (see Figure S4.1-2 for full device statistics). Solar cells involving a 2D/3D interface outperform their 3D reference, with a clear improvement in the device V_{OC}, without causing a detrimental loss of current. Notably, the boost in the V_{OC} appears higher for the PEAI-based 2D with respect to the FPEAI, overall leading to 20.62% PCE for the champion device. Such improvement asks for a deeper understanding of the optoelectronic processes governing the device operation, which is of key importance

Table 4.1-1: Device Parameters for the Champion Solar Cell.

	PCE (%)	V_{OC} (V)	Jsc (mA·cm^{-2})	FF
FPEAI-2D/3D	20.53	1.127	23.21	0.784
PEAI-2D/3D	20.62	1.138	23.43	0.774
ref 3D	19.48	1.104	23.25	0.759

for device development and which is often disregarded. The 2D portion being the core of our system, here we investigate the interface processes at the 2D/3D stack as well as at the HTM/2D/3D interfaces making use of a combined series of light-induced spectroscopic tools to shed light on the interface energetic and carrier dynamics on femtosecond to microsecond time scales.

4.1.2   Interface photophysics

Given the complexity of the 2D/3D system and the paramount importance of the 2D/3D interface energy levels alignment, we have combined X-ray photoelectron spectroscopy (XPS) with broadband transient absorption (TA). In TA, the selective excitation of the components will enable the monitoring of the photoinduced processes from 3D → 2D or from 2D → 3D, allowing us to retrieve the energy level alignment. Figures 4.1-2A,B displays the TA spectra and dynamics for 3D perovskite and 2D/3D systems upon excitation at λ_{ex} = 600 nm (selectively exciting the 3D), while the plots in Figure 4.1-2,D are obtained upon pumping at λ_{ex} = 390 nm (exciting both 2D and 3D). Exciting only the 3D portion (Figure 4.1-2), the signal is dominated by a large negative feature peaking at 750 nm, which forms with a time constant of 300 fs and persists throughout the investigated time window (1.5 ns). This feature relates to ground state bleaching (GSB) upon state filling at the 3D perovskite band edge.[122]

TA spectra of the 2D/3D systems are identical, with no difference in the evolution of the GSB (Figure 4.1-2). Given that the GSB is proportional to the photoexcited carrier density, its evolution reflects the charge dynamics. Notably, when exciting at λ_{ex} = 390 nm, the TA spectra (Figure 4.1-2) for the 2D/3D differ from the 3D control. Two additional negative features appear in the blue region (500-575 nm). They arise from the direct excitation of the 2D layer and relate to the GSB of the 2D perovskites. Given the spectral position, the peak at 500 nm matches with the GSB from pure R2PbI4, while the PB at 550 nm can be assigned to PB of an interfacial mixed phase (with n > 1, in agreement with the weak emission from a red-shifted band as shown in Figure S4.1-

5). Corresponding dynamics of FPEAI-2D/3D and PEAI-2D/3D GSB are presented in Figures 4.1-2D,E, compared to the GSB dynamics at 750 nm of the 3D portion. A clear trend is observed: the GSB at 750 nm rises (with a time constant of a few picoseconds, see Table S4.1-2) while the GSB at 500 nm decays with a similar time constant. This can be explained as a charge or energy transfer from the 2D to the 3D portions. However, we can safely exclude the later upon analysis of the photoluminescence excitation (PLE) map (Figure S4.1-6). If energy transfer would have occurred, one would have expected an increase in the PL of the 3D phase, upon excitation in the spectral region where the 2D portion absorbs. In contrast, we observe rather a reduction of the 3D PL signal, indicative of a filtering effect induced by the 2D layer.

Combing this information with the dynamic picture retrieved from the TA analysis, we can thus conclude that electron dissociation happens from the 2D to 3D perovskites. This is enabled by the favorable energy level interface matching, as shown by XPS data on the energy band alignment in Figure S4.1-8. The valence band maximum (VBM) of the 2D perovskite is just slightly down shifted by 0.1 eV with respect to the VBM of the 3D perovskite. Given the band gap of 2D perovskites around 3 eV, their conduction band minimum (CBM) lies well above the CBM of the 3D perovskite.[121] This energetically enables electron transfer from the 2D to the 3D portions as indicated by the TA results. The energy level landscape of the 2D/3D system is schematically depicted in the cartoon in the inset of Figure 4.1-2. To gain insight on the free carrier dynamics at the interfaces, a main goal of our work, we employ time-resolved photoluminescence (TRPL) and time-resolved photoconductance (TRPC) measurements targeting the 2D/3D interfaces (Figure 4.1-3A,) as well as the 3D/2D/HTL system (Figure 4.1-3C,D). Figure 4.1-3A show the TRPL decays at 780 nm, monitoring the 3D emission with or without the 2D layer. Note that in both cases we selectively excite the 3D portion with an excitation density of 10^{14} carriers/cm^{-3}.[123] Decays of 3D and FPEAI-2D/3D perovskite show a similar behavior (slightly slower for the FPEAI-2D/3D), while the PEAI-2D exhibits a much slower PL decay (see Table S4.1-1 for time constants). Figure 4.1-3B shows the
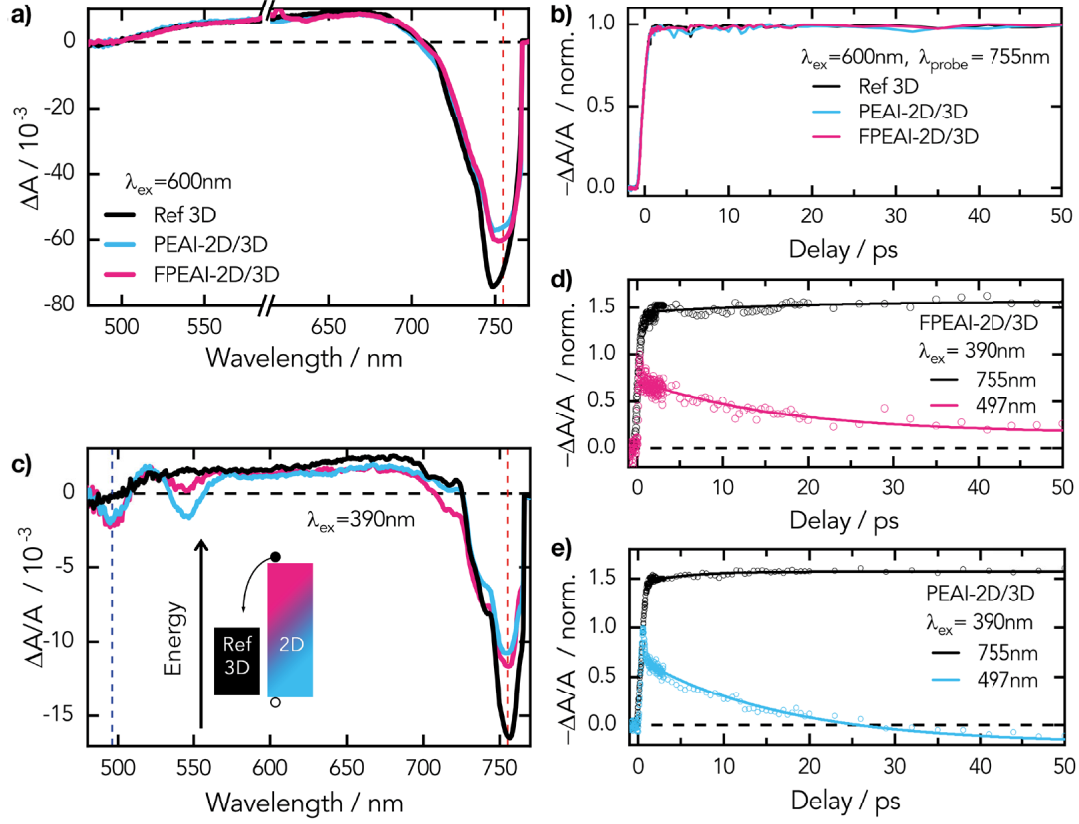
Figure 4.1-2: (a) Transient absorption (TA) spectra of 3D perovskite, PEAI-2D/3D, and FPEAI-2D/3D bilayers (excitation wavelength λ_{ex} = 600 nm, carrier density of 10^{18} cm^{-3}) at 1 ps delay (spectra up to 1 ns in Figure S4.1-3). (b) TA dynamics at 755 nm comparing 3D perovskite with PEAI-2D/3D and FPEAI-2D/3D bilayers (excitation wavelength λ_{ex} = 600 nm, carrier density of 10^{18} cm^{-3}). (c) TA spectra of 3D perovskite, PEAI-2D/3D, and FPEAI-2D/3D bilayers (excitation wavelength λ_{ex} = 390 nm, carrier density of 10^{18} cm^{-3}) at 1 ps delay (spectra up to 1 ns in Figure S4.1-4). Inset: illustration of band diagram and of the charge transfer from the 2D to the 3D perovskite. (c,d) TA dynamics of FPEAI-2D/3D and PEAI-2D/3D, respectively, at 497 and 755 nm upon excitation at 390 nm (carrier density of 10^{18}cm^{-3}). Samples have been excited from the 2D side.

TRPC signal, which monitors the free charges generated within the 3D slab and their dynamic evolution (see Figure S4.1-9 for carrier density-dependent dynamics). Notably, the initial amplitude of the TRPC signal is proportional to both the yield of free charges generated upon photoexcitation and their mobility, while the decay mirrors the charge im-

mobilization or recombination.[124] No sizable differences are observed between the initial TRPC amplitudes of the 3D and the 2D/3D-modified surfaces (see Figure S4.1-10).

However, their dynamics are different, as PEAI-2D shows a slower decay with respect to the bare 3D, while it is rather similar in the case of the FPEAI-2D. The combined TRPL and TRPC findings can be rationalized as follows: *(I)* The initial TRPC amplitudes indicate that no significant 3D $\rightarrow$ 2D hole transfer is taking place, as this would have lowered the amplitude of the signal at time zero (for instance, as is the case at the HTM/3D interface, see Figure S4.1-10), confirming the TA results. *(II)* The slower decay in both PL and TRPC results for PEAI-2D/3D indicates a delayed electron-hole recombination, possibly related to better surface passivation induced by the structural organization and homogeneity of the PEAI-2D layer, as demonstrated in the following (see Table S4.1-2). *(III)* This does not extend to FPEAI-2D/3D system, which exhibits similar behavior with respect to the bare 3D sample. To determine the kinetic parameters from the TRPC measurements, we have applied the kinetic model described in the Letter by Hutter et al. (see the relevant parameters summarized in Table S4.1-4 in the Supporting Information, together with a description of the model and experimental fits in Figure S4.1-9 and S4.1-11).[59] Interestingly, the bimolecular recombination rate constant, k_2, is halved upon addition of PEAI or FPEAI-2D layers on the 3D perovskite. As previously reported, k_2 represents the sum of all bimolecular recombination processes.[125] Therefore, the bimolecular recombination processes occurring at the 3D surface is considerably retarded by introducing the 2D perovskite. The enhanced lifetimes in the case of PEAI-2D/3D samples are related to the significantly reduced number of background charges in the material, which slows down the bimolecular recombination. In light of this, and in agreement with the energy level alignment previously discussed, we conclude that the PEAI-2D/3D interface can retard the electron-hole recombination and passivate the 3D surface much more efficiently compared to the FPEAI-based system.

Figures 4.1-3C,D shows the TRPL and TRPC signals for 3D/2D/HTM systems. From Figure 4.1-3C, the PL shows similar decays, with a slower tail component for the PEAI-
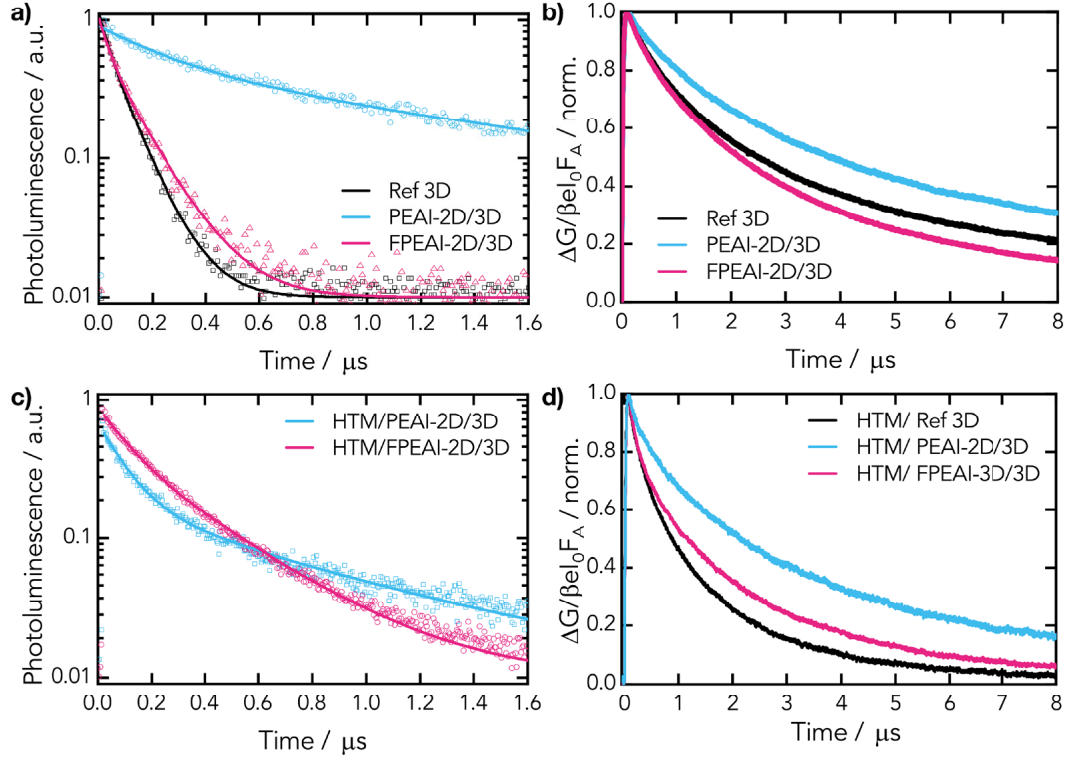
Figure 4.1-3: (a) Normalized photoluminescence (PL) decay of PEAI-2D/3D, FPEAI-2D/3D, and ref 3D sample (excitation wavelength λ_{ex} = 635 nm, carrier density of 10^{14} cm^{-3}).(b) Normalized time-resolved photoconductance (TRPC) of the same samples ($lambda_{ex}$ = 650 nm, carrier density of 10^{14} cm^{-3}). (c) Normalized PL decay of HTM/PEAI-2D/3D and HTM/FPEAI-2D/3D samples ($lambda_{ex}$ = 635 nm, carrier density of 10^{14} cm^{-3}). (d) Normalized TRPC of bilayers of HTM/PEAI-2D/3D, HTM/FPEAI-2D/3D, and HTM/3D (λ_{ex} = 650 nm, carrier density of 10^{14} cm^{-3}). Samples have been excited from the 3D side.

2D/3D system (see Table S4.1-2 for the time constants). From the TRPC measurements in Figure 4.1-3D (also see Figure S4.1-10) we can observe that the initial amplitudes drop, and the dynamics get faster if the HTM is deposited on top. This is indicative of a reduction of the charge density due to hole transfers and faster decay due to interfacial recombination. Comparing the TRPC signals of the 3D/HTM with 3D/2D/HTM samples, we observe that the addition of a 2D layer does not hinder the charge transfer to the IITM (initial amplitude reduction, see Figure S4.1-10), but recombination is slowed down more visibly for the PEAI-based system. As a physical spacer, holes can be easily

delocalized at the 2D/3D interface, given the low energetic barrier perceived by the holes at the 2D phase, thus favoring charges transfer to the HTM. Therefore, the 2D layer can act as a physical spacer where, especially in the case of PEAI-2D, back electron-hole recombination is retarded. Overall, our results point to a beneficial effect of the 2D layer by reducing surface recombination, which can explain the improvement in the device V_{OC}. As an important remark, we observe that this statement does not hold a general validity but strongly depends on the chemical nature of the organic cation composing the 2D layer. In particular, despite the close energetic and similar electronic structure of their corresponding 2D layers, PEAI-2D/3D and FPEAI-2D/3D behave differently.

4.1.3 Grazing angle X-ray diffraction

To address the reason behind such different behavior, we investigate the structural properties of the interfaces and the crystal plane orientation by GIWAXS measurements. This technique is extremely surface-sensitive at incident angles below the critical angle, allowing one to directly probe the 2D perovskite layer. GIWAXS maps and the corresponding sector averages are shown in Figure 4.1-4A,B. Diffraction peaks associated with the lamella structure of the 2D phase are clearly visible for $q < 1.0$ Å^{-1} and correspond to the (0k0) planes. Both the PEAI and FPEAI layers show a major diffraction peak for the pure 2D phase (n = 1), with first order at 0.36 Å^{-1} and higher orders at 0.74 Å^{-1} and 1.08 Å^{-1}. We also observe a minor intermixing phase resulting in a weak n > 1 (n = 2, more precisely) diffraction peak (first order at 0.25 Å^{-1}; higher orders at 0.52 Å^{-1} and 0.80 Å^{-1}). Interestingly, the PEAI-2D layer clearly exhibits the presence of n > 1 phase, more visible if compared to FPEAI-2D with a stronger first-order 0.25 Å^{-1} peak. This assignment is also supported by the PL and TA spectra. PL spectra (Figures S4.1-3-S4.1-5) show a weak shoulder at 550 nm assigned to n = 2 quasi-2D perovskite emission; and TA spectra (λ_{ex} = 390 nm, Figure 4.1-2A) exhibit a second peak at 540
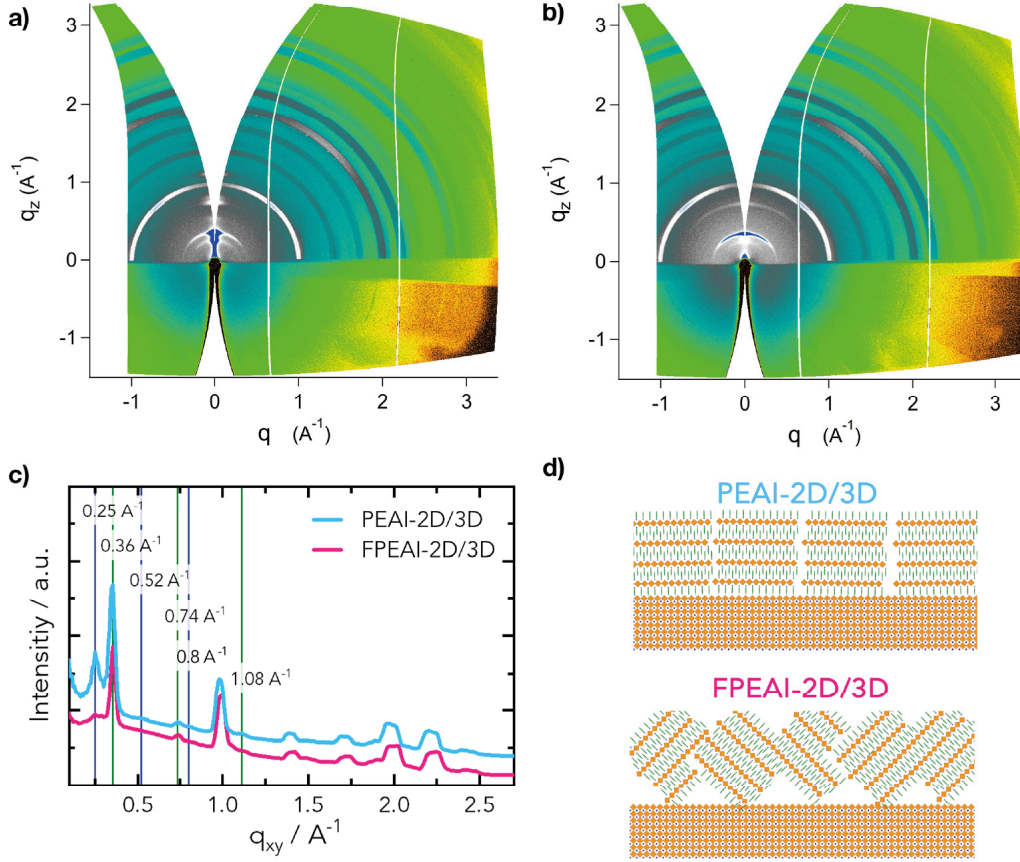
Figure 4.1-4: (a) GIWAX map of PEAI-2D/3D showing a parallel preferred orientation in low-q region below the 3D bulk perovskite peak of qz = qxy = 1.0 Å^{-1}. (b) GIWAX map of FPEAI-2D/3D showing more random orientation. (c) 2D GIWAXS sector average for PEAI-2D and FPEAI-2D layers atop 3D bulk. The 2D (n = 1) features are noted by green lines, while the n > 1 (n = 2) features are noted by the blue lines. The PEAI-2D layer clearly shows relatively more intermixing of lower dimensionalities compared to the FPEAI-2D. (d) Cartoon representing preferred orientation of the 2D on top of the 3D bulk.

nm associated with the GSB of the n = 2 quasi-2D perovskite, as previously discussed. The first-order peak at 0.36 Å^{-1} belonging to the n = 1 lattice was integrated with respect to the azimuthal angle (χ) to glean information regarding the orientation of the 2D perovskite planes. Results are reported in Figure S4.1-12 comparing the FPEAI-2D- and the PEAI-2D-based interfaces. From Figure S4.1-12, it is clear that the PEAI-2D peak integral is almost entirely in the range of $\chi = 0°$-$5°$, suggesting that the layers as-

sume a parallel orientation with respect to the underlying 3D phase and the substrate (as observed in other 2D-based systems).[126]

In contrast, the formation of FPEAI-2D layers is more random: a majority of these layers have a 40°-45° orientation with respect to the 3D phase and the substrate (see Figure 4.1-4C,D). We suggest that the different crystallite orientation of PEAI-2D and FPEAI-2D is the reason behind the different interfacial physics observed. In the case of the parallel orientation of PEAI-2D, the slowing down of the TRPC dynamics proves that back electron hole recombination (between holes in the HTM and electrons in the 3D perovskite) is retarded, with a direct positive impact on the charge carrier lifetime and thus on the device V_{OC}. The intimate reason behind this lies in the structural orientation of the PEAI-2D and the uniformity of this layer enabling a more perfect homogeneous physical spacer between the 3D perovskite and the HTM. The random orientation of FPEAI-2D is responsible for the lack of a beneficial effect of the 2D interlayer in terms of enhanced charge lifetime. In addition, disorder in the 2D portion may allow partial interpenetration of the HTM, leading to behavior of the FPEAI-2D/3D that is similar to that of the 3D-only system. Our findings present a different picture with respect to common knowledge: while much effort has been focused on orienting the 2D planes perpendicular to the substrate in a way to maximize charge transport and extraction,[127–130] here we reveal that, contrarily, planar orientation is needed in the case of 2D/3D interfaces to optimize interface processes and device performances. A similar finding has been revealed for Sn-based 2D/3D interfaces where planar growth of the 2D is essential for the device operation.[126] Further analysis, beyond the scope of the presented work, will be needed to clarify the transport mechanism through the organic barrier.

4.1.4   Conclusion

To conclude, we elucidate the optoelectronic properties and carrier dynamics at 2D/3D interfaces leading to highly efficient solar cells. Our results provide compelling evidence of the crucial role of the crystal alignment of the 2D perovskite on top of the 3D perovskite.

If the 2D perovskite orients "flat" with respect to the substrate, it can effectively passivate the surface while retarding charge recombination. This results in an enhanced V_{OC} of the solar cells and overall improved performance. On the other side, a more disordered 2D perovskite alignment limits such beneficial effects. We demonstrate that such alignment can be controlled by fine-tuning the chemical composition of the 2D cation, i.e. by a simple atomic substitution, providing a new guideline for material and interface design.

4.2 Dynamic evolution of the 2D/3D interface: A hidden driver behind perovskite solar cell instability

This is part of a work publish with the same title in J.Mater.Chem.A, 2020, 2343-2348.[131] Thanks to A. Sutanto which carried all the sample preparation as well as device characterisation and general discussion. My contribution was focused on PL measurement, analysis and general discussion.

Previously, we have seen how choosing the organic cation can change the crystallisation and interface dynamics of the 2D layer. However, the evolution of the interface in time as the material age and the solar cell works wasn't investigated. This is the point of this study to research how different 2D/3D interface, with different organic cations specially synthesize for the occasion, react to time and heat cycles. The cations used for this study are thiophenealkylammonium salt. More precisely, three derivatives : 2-thiophenemethylammonium iodide (2-TMAI), 3-thio- phenemethylammonium iodide (3-TMAI), and 2-thio- pheneethylammonium iodide (2-TEAI)(see annex for synthesis and figure S4.2-1 for the molecular structure). The difference between them is the position if the alkyl chain in the thiophene for the 2- and 3-TMAI and the length of the chain for the 2-TEAI.

4.2.1 Interface and cell characteristics

The interface was created using the same method presented before as well as the rest of the cell. Only the cations differ. However, changing the cation change the nature of the

interface. Indeed, in the case of these thiophene cations, the 2D layer as an increased dimensionality compared to the previous study. 2-TMAI and 3-TMAI have a preferred n=2 arrangements and 2-TEAI n=1. This is reveled by the XRD pattern where the 6°peak, corresponding to n=1, is not the prevalent one but the 4°peak, corresponding to n=2, is (see figure S4.2-2). The photovoltaic characteristic of solar cells made with these cations is reported in table 4.2-1. The cells show similar behavior with respect to the reference with a slight deviation for 2-TEAI which has a lower PCE mainly because of the slightly small Voc and FF.

Table 4.2-1: Photovoltaic parameters of champion aged for 24 weeks 2D/3D PSCs employing 2-TMAI, 3- TMAI, 2-TEAI, and 3D control Organic

Sample	Voc (V)	Jsc(mAcm^{-2})	FF	PCE (%)
2-TMAI	1.132	23.50	0.751	19.97
3-TMAI	1.132	23.60	0.771	20.59
2-TEAI	1.117	23.60	0.737	19.42
3D	1.124	23.57	0.773	20.48

However, when look at the stability of these cells the story is different. Figure 4.2-1 show the stability of the different samples under continuous illumination for 1000 hours. After 1000 hours, the 2-TEAI is now the best performing with a 90% retention of the initial PCE. Three other samples all have a similar 70% retention. A natural question arises, why is this the case? To investigate this point, we focus our attention on the evolution of the interface. We want to understand what is changing when the cell is under light and more precisely what is happening to the 2D and 3D perovskite layers when the different cations are used.
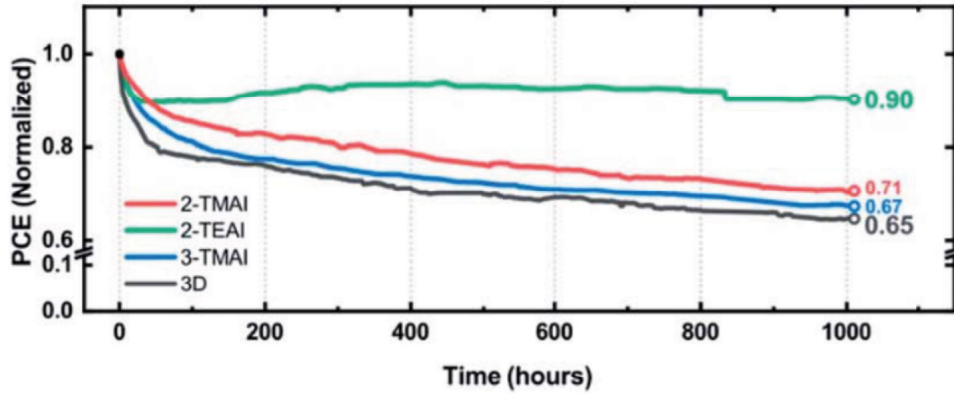
Figure 4.2-1: Stability test for freshly prepared devices under continuous 1 sun illumination for 1000 h in an Ar atmosphere without any encapsulation.

4.2.2 Interface evolution

To investigate this evolution of the interface, we accelerated the aging of the cell by eating it at 50°C for several hours and monitor the material by measuring the photoluminescence(pl) of the sample. Figure 4.2-2 show the pl of the different sample after several heating interval. Before heating, we can see the 2D ans 3D layers emitting at between 500nm-600nm and 780nm respectively. The n=2 2D morphology is clear for the 2-TMAI and 3-TMAI with the peak at 575nm. The n=1 is visible on the 2-TMAI and 2-TEAI at 525nm. The presence of multiples 2D peaks shows that the interface has a complex structure and depending on the cation used, even is almost similar, the 2D layer morphology changes. As time increases, a very clear process is happening for 2-TMAI and 3-TMAI. The 2D peak is weakening an the 3D one increasing as well has new peaks appearing. This isn't the case for 2-TEAI. This particular cation only exhibits a slight shoulder on the 2D peak.

Focusing on cations individually, we can see on figure 4.2-2 A that the 2-TMAI pl spectra shift from from a mixutre of n=1 & 2 to only n=2. This suggests that 2D layer is reacting with the 3D perovskite underneath, transforming the remaining 2D n−1 into n=2. Looking a figure 4.2-2 B, the 3-TMAI layer is also reacting with the 3D

layer forming higher dimensionality quasi-2D layer with a high n number with a spectral signature around 650nm shifting and growing with a prolong exposure. Now, regarding the 2-TEAI on figure 4.2-2 C, we do not see this phenomenon. The nature of the cation and the resulting 2D layer prevent it from reacting with the 3D perovskite leading to change in morphology.
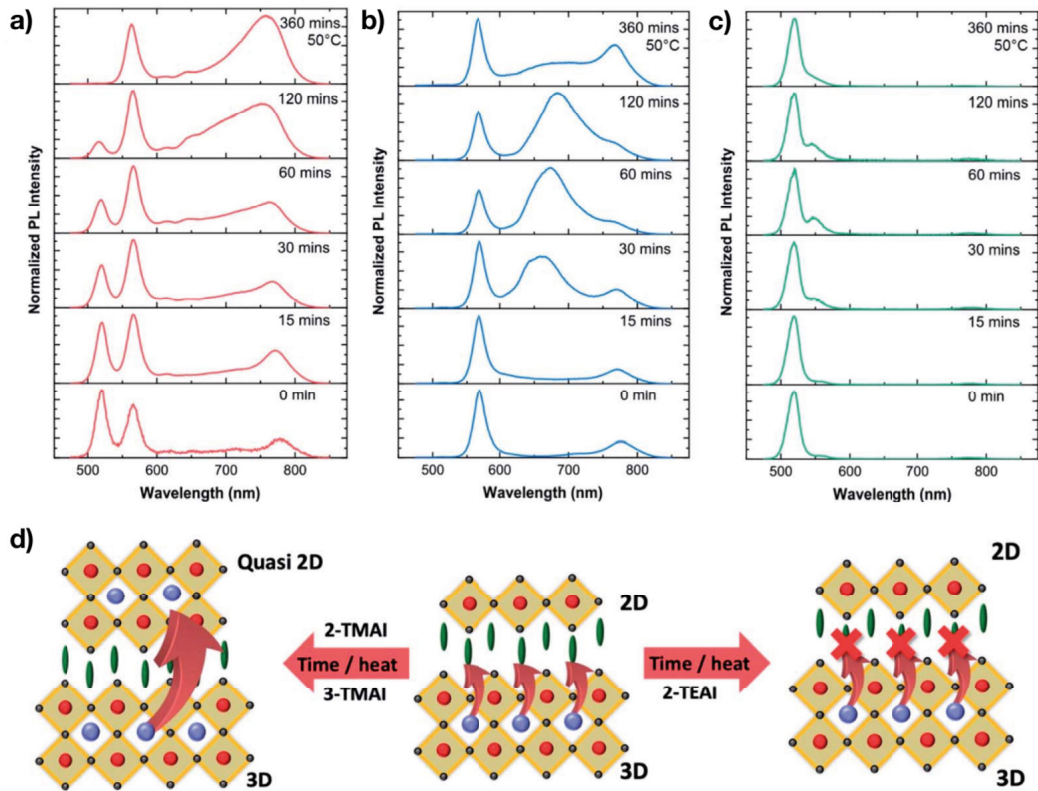
Figure 4.2-2: PL spectra upon thermal stress (heating the film at 50°C for the time as indicated in the legend) for (a) 2-TMAI, (b) 3-TMAI, and (c) 2-TEAI 2D/3D systems. (d) Cartoon illustrating the proposed interfacial mechanism. 2346

Given that the 2D layer is changing, the culprit is the methylammonium(MA) cation of the 3D layer. Indeed it has been shown that this small cation can be volatile and is one of the degradation paths of 3D perovskite. The 2D over layer is then acting as a sponge, reacting with this methylammonium and changing the structure of the 2D layer as presented in figure 4.2-2 D. The 2-TEAI cation is preventing the MA from going out of

the 3D perovskite, thus decreasing degradation. The 2-TEAI having a longer alkyl chain, is strain forward to suggest that this feature is the reason for the increase robustness of the 2D layer as well as how the cation are packing.

4.2.3 Conclusion

The leaking of MA in the 2D layer is undeniably a mechanism to prevent for highly efficient solar cells. The choice of the cation is crucial in mitigating this problem. Choosing a cation that creates a robust n=1 2D layer is key for increase stability. This study reveals that larger cation perform better in these regards and should be considered in the development of future highly efficient and stable solar cells.

4.3 In Situ Analysis Reveals the Role of 2D Perovskite in Preventing Thermal-Induced Degradation in 2D /3D Perovskite Interfaces

This is part of a work published with the same title in NanoLett.2020, 20, 3992-3998.[132] A. Sutanto which carried all the sample preparation as well as device characterisation and general discussion. My contribution was focused on PL measurements, analysis and general discussion.

Here we investigate the 2D/3D film properties during thermal stress, monitoring the structural evolution of the interface and the related optoelectronic and dynamic properties. We performed combined steady state and time- resolved photoluminescence (PL) measurements as well as XRD on two study cases of 2D/3D perovskite systems used in the most common highly efficient device configuration.[121,131] They consist of the same bulky thiophene- or phenyl-terminated cations in the form of 2-thiophenemethylammonium iodide (2-TMAI) presented in the previous section and phenylethylammonium (PEAI), forming (2-TMAI)$_2$PbI$_4$ and PEA$_2$PbI$_4$ 2D perovskites, respectively, which overlay the bulk 3D perovskite. (See Figure 4.3-1) The structural evolution of the interface is monitored upon exposing the sample to a thermal cycle, simulating the working conditions

under real device operations. We reveal that a slow dynamic variation of the 2D/3D interface manifests, leading to a structural modification of the 2D perovskite. In concomitance, the 3D perovskite bulk, if protected by the 2D layer, is unperturbed, whereas in the absence of the 2D layer, it shows visible signs of structural degradation. We thus identified a key role of the 2D capping layer in blocking the thermal degradation of the 3D perovskite bulk, maintaining its structural integrity, and retarding thermally induced degradation in perovskite solar cells.

4.3.1 Interface characterisation

To create the 2-TMAI- (or PEAI-) 2D/3D thin films and devices, we dissolved the organic salts in isopropanol (IPA) and dynamically spin-coated them on the top of a triple-cation $[(FAPbI3)_{0.87}(MAPbBr_3)_{0.13}]_{0.92}(CsPbI_3)_{0.08}$ based 3D perovskite film, where MA stands for methylammonium and FA stands for formamidinium. (See Annexe S4.3.1 for details.) As a result, a thin layer of 2D perovskite ($\sim$60 nm) was formed on top of the 3D bulk, as shown by the scanning electron microscope (SEM) image in Figure 4.3-1 (right).
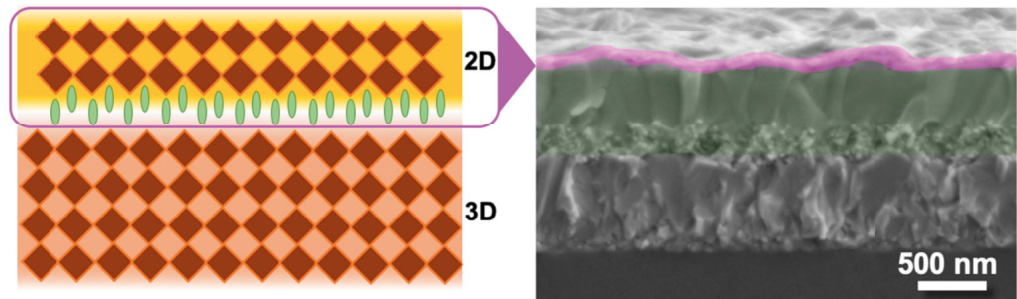

Figure 4.3-1: Cartoon of the 3D/2D interface (left) and the corresponding cross-sectional SEM image of the 3D/2-TMAI 2D interface.

4.3.2 Interface thermal evolution

To better elucidate the structural changes in the 2D layer, we monitored the PL spectral evolution as a sensitive probe of the material band gap and the variation thereof, which is

indicative of any possible structural change (i.e., n variation), following a similar thermal cycle, as shown in Figure 4.3-2.
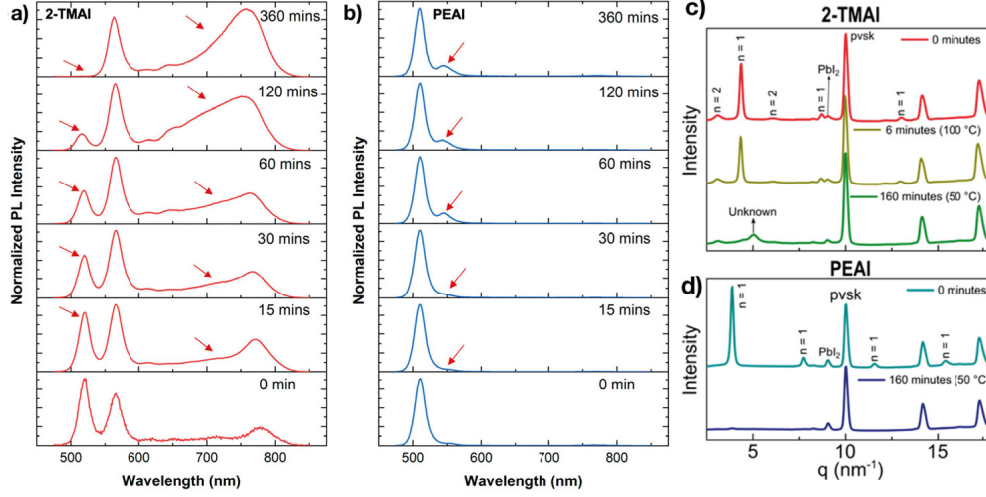
Figure 4.3-2: PL spectra of (a) 2-TMAI-2D/3D and (b) PEAI-2D/3D perovskite thin films upon thermal aging at 50°C and excitation at 450 nm from the front (in other words, from the 2D side),(c,d) Respective X-ray diffraction patterns at different times.

Because the PL spectra were recorded from the front side (2D perovskite side) of the 2D/3D film, they mainly show the emission from the 2D perovskite top layers. The PL measurements were carried out after thermal annealing at 100 °C and without heating to 50 °C (time 0 for PL characterization). At time 0, the 2-TMAI-2D/3D film PL spectrum shows two emission bands centered at 519 and 567 nm, whereas the PEAI-2D/3D film shows only one band at 510 nm and a small shoulder at 555 nm. According to the literature, these bands correspond to the emission from n =1 and 2 phases of 2D perovskites, respectively,[131, 133] in excellent agreement with the XRD results presented in Figure 4.3-2c and d. From the normalized PL spectra reported in Figure 4.3-2, it is also evident that for the 2-TMAI 2D-based interface a broader emission in the 700-800 nm spectral range gradually appears during the annealing process. This suggests the formation of a mixed disordered phase,[134, 135] in agreement with the XRD data. On the other hand, for PEAI-2D/3D, the variation of the shape of the PL spectra is less dominant, whereas the absolute intensity (reported in Figure S4.3-3a) of the n = 1 PL peak abruptly dimin-

ishes, in agreement with the XRD data. This suggests that PEAI-based 2D perovskite is structurally more robust and less prone to forming a quasi-2D (n > 1) phase under these conditions.[136,137] A similar behavior of the intensity is observed for the 2-TMAI 2D-based interface, showing a decrease in the n = 1 PL peak and a concomitant increase in the broader emission at the longer wavelength side (Figure S4.3-3b). These measurements prove the dynamic variation of the 2D surface perovskite band gap. To gain a deeper understanding of the mechanism behind such dynamic structural/band gap evolution, we also measured the PL spectra of the 2D/3D perovskite films upon aging the film for a long time window of 7 weeks without any heating. The films were stored in a dark and dry environment (RH < 20%) at room temperature, and the PL spectra were periodically recorded over time. Interestingly, we observed an analogous modulation of the emission features for both 2-TMAI-2D/3D and PEAI-2D/3D over slow dark aging, as shown in Figure S4.3-4. This phenomenon indicates that a similar transformative process happens even at room temperature, over a several weeks time window, while being accelerated under thermal stress. We can rationalize our results considering an intrinsic dynamic evolution of the 2D/ 3D perovskite interface upon aging, which manifests as (I) destructuration of the 2D perovskite overlayer and (II) the formation of an additional mixed phase at the interface, both combined with (III) improved resilience to the degradation of the 3D perovskite bulk underneath, independent of the 2D cation used.

To better analyze the interfacial processes, we implemented time-resolved PL (TrPL), with the idea of monitoring the charge- carrier dynamics in the 3D bulk upon the thermal cycle. The thermal aging for the TrPL measurement was performed under the same conditions as in the steady-state PL measurement. The results are reported in Figure 4.3-3 for the 2D/3D interface (blue and red) compared to the control samples without the 2D layer. It is worth noting that upon thermal aging, the PL signal of the bare 3D film shows an enhancement of the lifetime with a marked long living tail. This happens at time 0 but is even more evident after 15 min of annealing, and it continues to increase up to 360 min of thermal aging (Figure S4.3-5). This is also true for the 2D/3D interface,
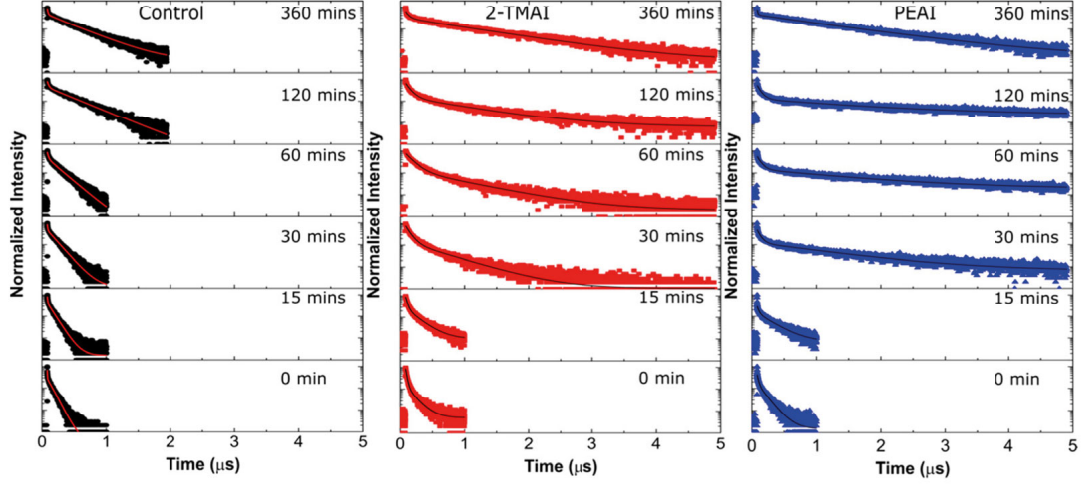
Figure 4.3-3: TrPL decays (λ_{exc}= 440 nm;F= 9.7 nJ cm^{-2};λ_{PL} at the maximum of the 3D at 780 nm emission at 50°C in the samples) of the 2D/3Dmodified perovskites: 3D control (black), 2-TMAI (red), and PEAI (blue). The fits of the decays are also shown

where the increase in the lifetime is even more evident. We can attribute the longer living signal to the beneficial effect of the restructuring of the interface, leading to the surface passivation effect and retarded surface charge-carrier recombination.[47,134]

4.3.3 Device perspective
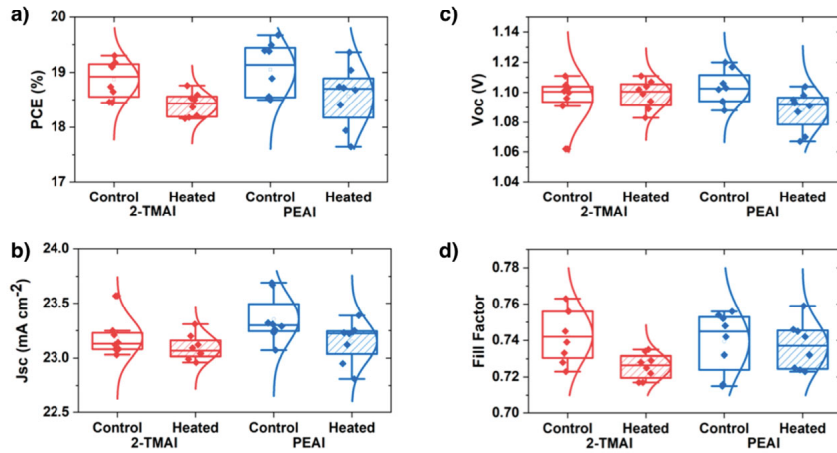
Figure 4.3-4: a)-c) Statistics of the device photovoltaic properties (PCE, Voc, Jsc, FF) by comparing the fresh device and the thermally aged devices.

Device where made in the same conditions and subjected to the same thermal treatment. It is interesting to note that upon thermal stress, the device characteristic is not dramatically affected, showing no massive effect of the thermal stress on the device efficiency. A small decrease is observed only for the device fill factor, which, however, does not dramatically reduce the overall device performance.

4.3.4 Conclusion

In conclusion, the in situ structural and optical analysis of 2D/3D perovskite interfaces gives a compelling proof of an intrinsic dynamic structural variation of the 2D perovskite layer after thermal stress, which (*I*) protects the 3D perovskite from degradation regardless of the 2D perovskite phase evolution upon heating, (*II*) does not perturb the dynamic processes at the interface, and (*III*) is beneficial to keeping the device performance unaltered under thermal stress. Our results have highlighted the key role of the 2D surface functionalization in retarding perovskite degradation upon thermal stress, providing a clear direction on how to gain perovskite device longevity.

4.4 Conclusion

In this chapter we have investigated the interaction of 2D perovskite deposited on top of 3D perovskite. We have elucidated the optoelectronic properties and carrier dynamics at 2D/3D interfaces leading to highly efficient solar cells. Our results provide compelling evidence of the crucial role of the crystal alignment of the 2D perovskite on top of the 3D perovskite. We demonstrate that such alignment can be controlled by fine-tuning the chemical composition of the 2D cation.

Furthermore, we have explored the evolution of the 2D/3D interface and revealed that the leaking of MA in the 2D layer is undeniably a mechanism to prevent for highly efficient solar cells. Choosing a cation that creates a robust n=1 2D layer is key for an increased stability. This study reveals that larger cations perform better in this regard and should

be considered in the development of future highly efficient and stable solar cells.

Finally, we have inspected the thermal stability of the 2D/3D interface. We have shown that the dynamic structural variation of the 2D perovskite layer after thermal stress is beneficial to keep the 3d bulk unaltered under these conditions, providing a clear direction on how to increase perovskite device longevity.

CHAPTER 5

MoS$_2$

In previous chapters we have explored low dimensional perovskite as a standalone material and as an interface layer. The search of interface layers in PSC is intense. Many materials have been proposed as HTM or intermediate layer to increase the transport of carriers while preventing losses. They are new organic HTM design, inorganic crystalline material, 2D perovskite or other low-dimensional materials. The latter are of a particular interest thanks to their peculiar and tunable optoelectronic properties and the very high activity in their respective research field.[51, 138–142] Notably, Molybdenum disulfide (MoS$_2$), is a member of the two-dimensional (2D) layered transition metal dichalcogenides(TMDC) family of compounds. TMDCs are characterized by planes held together by Van der Waals interaction similarly to 2D perovskite. The optical and electrical properties rising from the strong intra layer and weak inter layers in this layered family of compounds are unique. Therefore, they have attracted the interest of researchers ranging from catalysis to optoelectronics.[143–147] MoS$_2$ is viewed as an analog of graphene. It can be a semiconductor in the 2H symmetry phase. It has an indirect bandgap when bulk and a direct bandgap in monolayers with visible excitonic transitions at room temperature. While in the 1T phase, it exhibits metallic properties.[148–154] MoS$_2$ monolayers could absorb 5–10% incident sunlight within 1 nm in thickness, far exceeding that of traditional

semiconductors. It has been successfully implemented in hetero-structured devices and even in ultrathin solar cells, demonstrating a power density orders of magnitude higher than the best existing ultrathin solar cells, opening the path for the development of light detection and harvesting in atomically thin devices.[155, 156]

MoS$_2$ and derivatives were used as a transport layer in high efficiency PSC device. The low cost of the material compared to more traditional IITM such as Spiro-OMeTAD offer an interesting alternative without compromising the efficiency. In addition, it as also been used as buffer layers for an increased cell lifetime.[142, 157, 158] Behind that what drives the material operation is the light-matter interaction. The deep investigation of the photoinduced species and dynamics is therefore a requirement for designing a synergistic relation between MoS$_2$ and perovskite. A plethora of reports regarding different optical characteristics of MoS$_2$ exist. They revealed the effect of the number of layers on carriers and quantum yield, the formation of biexcitons, trions, and more.[151, 153, 159–162] The dynamics of the photocarriers was also extensively studied up to one nanosecond. Excitons in monolayer MoS$_2$ have exceptionally large binding energies and dominate the optical properties within the material. Exploring the relaxation behavior of excitons is crucial for understanding the fundamental physics as well as the performance of MoS$_2$-based optoelectronic devices. The dominant processes of carrier relaxation in bulk MoS$_2$ are dominated by both carrier-carrier and carrier-phonon scattering, while that in mono-layer MoS$_2$ is dominated by defect-assisted scattering.[163–165] The inter band relaxation processes in monolayer MoS$_2$ are much shorter than those in bulk MoS$_2$. This suggests that nonradiative relaxation processes rather than radiative ones dominate the exciton dynamics in monolayer MoS$_2$. In addition, the carrier lifetime of MoS$_2$ increases with the number of layers since the defect-assisted recombination at the surface becomes significant. Upon photoexcitation, exciton-exciton annihilation (hundreds of femtoseconds) is observed, followed by the trapping of the excitons by surface states (a few picoseconds), and inter band carrier-phonon scattering (tens of picoseconds). Moreover, absorption due to mid-gap defects can also be observed, depending on the quality of the sample, such

as if grown by CVD. Exciton dynamics deplete over hundreds of ps time scale, which is the typical time window so far investigated by standard ultrafast transient spectroscopy. However, revealing the photophysics over a more extended timescale can open the view to processes such as trapping/detrapping and carrier dynamics. The longer timescale measurements over one nanosecond were neglected. However, they can provide valuable physical insights into the design and development of complex 2D devices dominated by free carrier such as in a buffer layer in a PSC and is thus the aim of the presented work.

5.1 Exploratory study on the origin of long living photo-excitations in single flakes of MoS_2

In this study, we provide a complete picture of photoexcited state dynamics in few layers thick MoS_2 samples probing for the first time the photoexcited species and their subsequent dynamic evolution in a time frame from 200fs up to $100\mu s$. We reveal that rich photoinduced dynamics, so far neglected, happen at a long timescale. We are identifying the presence of long-living charges of utmost relevance, the wide range of the MoS_2 potential field of application.[143-147]

5.1.1 Sample characterization

Figure 5.1-1a) shows a picture of the artificial MoS_2 crystal (2H-phase), which was exfoliated in liquid-phase through sonication in IPA, as described in the Method section. The ultraviolet-violet (UV-vis) absorbance spectrum of the LPE-produced MoS_2 nanoflakes dispersion is shown in Figure 5.1-1a, which reveals four main peaks. More in detail, the peaks around 673 nm and 611 nm are associated with the direct transitions from the valance band to the conduction band at the K-point of the Brillouin zone of layered MoS_2, known (A and B transitions, respectively). The broad absorption bands centered at 444 nm and 403 nm are attributed to the C and D inter-band transitions between
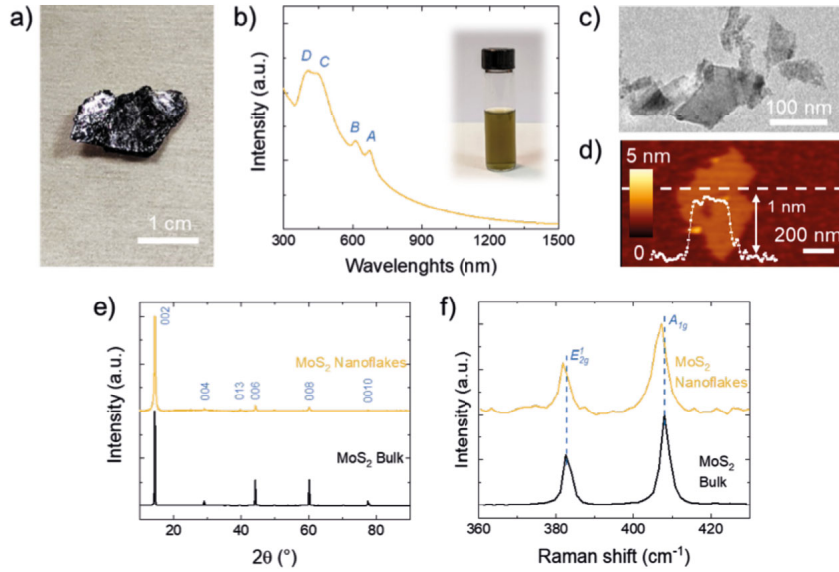
Figure 5.1-1: (a) Photograph of a 2H-MoS$_2$ crystal. (b) Absorbance spectra of the LPE-produced MoS$_2$ nanoflakes dispersion, together with its photograph. (c) TEM and (d) AFM images of representative MoS$_2$ nanoflakes. e) XRD patterns and f) Raman spectra of MoS$_2$ bulk crystals and nanoflakes. The XRD peaks are named according to the reference card for the 2H-MoS$_2$ (JCPDS card No. 37-1492).

the density of state peaks in the valence and conduction bands of 2H (semiconducting) phases.[159, 166–168] The morphology of the LPE-produced MoS$_2$ Moflakes was evaluated through TEM and AFM analyses (Figure 5.1-1 c,d). The MoS$_2$ nanoflakes have irregular flat shapes with straight borders, as observed in previous studies.[169–171] The data statistical analysis Figure S1,2 indicates that the lateral size and thickness values of the MoS$_2$ nanoflakes follow log-normal distributions peaking at 57.2 nm and 1.7 nm, respectively. Since the MoS$_2$ monolayer thickness measured by AFM is in the range of 0.70.8 nm, our results indicate that the LPE-produced MoS$_2$ nanoflakes mainly consist of single-/few-layer flakes.[172, 173] Figure 5.1-1e reports the XRD pattern of both MoS$_2$ bulk crystals and the MoS$_2$ nanoflakes. The samples shows the same diffraction peaks, which match those of the reference card of the 2H-phase of the MoS$_2$ (JCPDS card No. 37-1492). These results prove that the LPE process does not alter the crystallinity of the bulk materials. Compared to MoS$_2$ bulk crystals, the intensity of the (002) peak is signifi-

cantly more pronounced relative to the other peaks, indicating the exfoliated nanoflakes preferentially orient parallel to the substrate.[169, 174] The crystallinity of the samples was further confirmed by Raman spectroscopy measurements (Figure 5.1-1f). According to the symmetry space groups symmetry of MoS_2 bulk crystals (P3m1, point group: D6h) and exfoliated MoS_2 flakes (P3m1 for an even number of layers, and P6m2 -point group: D3h- for single-layer and systems with an odd number of layers), the samples show two main peaks, i.e., $E^1_{2g}(\Gamma)$ and $E_{2g}(\Gamma)$.31,32 In particular, $E^1_{2g}(\Gamma)$ is first-order modes at the Brillouin zone center, while $A_{1g}(\Gamma)$ represent the in-plane displacement of Mo and S atoms and the out-of-plane displacement of S atoms, respectively. As shown in Fig. 5.1-1h, the $E^1_{2g}(\Gamma)$ mode of the exfoliated MoS_2 flakes exhibits a softening compared to the one of the bulk MoS_2. The redshift of the $E^1_{2g}(\Gamma)$ mode is attributed to the dielectric screening of long-range Coulomb MoS_2 inter layer interaction.33 This effect confirms further the exfoliation of the MoS_2 bulk crystals into nanoflakes.

5.1.2 Ultrafast spectroscopy

Figure 5.1-2a shows the abortion spectra of MoS_2 around the A and B excitons. Their respective position is marked by the two dotted lines at 610nm and 670nm for the A and B excitons, respectively. Figure 5.1-2b presents the TA spectra with a 400nm excitation at $10\mu J/cm^2$ at selected delays in the picosecond time range: from 0.1 to 100ps(Setup description in annex S5.1.1). We see two positive features at the two exciton positions that are moving to a shorter wavelength at longer delays. Around the two positive features, negative features are visible. Figure 5.1-2c shows as well the TA spectra of MoS_2 but at a longer time frame. It presents spectra from 0.1 ns(same as 100ps) up to 1000 ns. The two positive features are still visible over the entire time range. They, as well, continue to blue shift as time passes. The negative peaks are also still present. In figure 5.1-2d we present the color map of the complete TA experiment from 0.1ps up to $100\mu s$ on a log scale. In this figure, we can follow the entire signal. From the rise, all the way to the decay after $1\mu s$. The two excitonic features are represented by two red traces. The
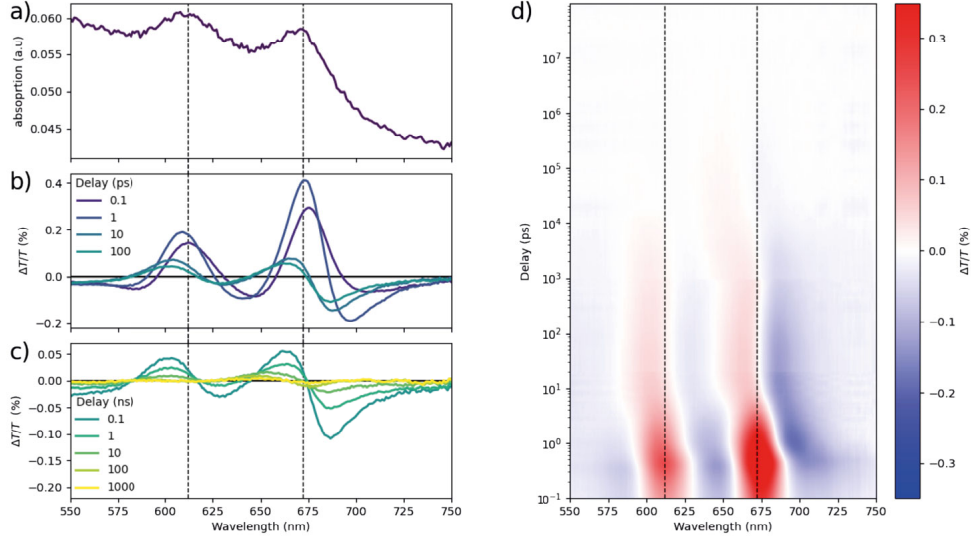
Figure 5.1-2: (a) Absorption spectra of few-layer MoS_2 nanoflake thin film. Dotted lines represent the position of the A and B exciton at $\sim$670nm and $\sim$610nm respectively (b) TA spectra with 400nm excitation at $10\mu J/cm^2$ of few-layer MoS_2 nanoflake thin film at selected early delays(0.1-100 ps). (c) TA at late delays(0.1-1000 ns). (d) color map of the complete TA experiment. The positive amplitude is in red and the negative in blue.

dotted lines represent the excitonic absorption position of figure 5.1-2A. Their respective blue shift overtime is also clearly visible and is of about 25nm between 1ps and $1\mu s$. Interestingly we can see on the A exciton position($\sim$675nm) that the shift occurs in two steps. The first up between 0.1ps and 10ps, and the second between 1ns and 100ns. A similar behavior is visible for the B exciton as well.

Going back to the early time spectra of figure 5.1-2b, we assigned the two positive features to the photobleaching(PB) of the A and B excitonic transition. The negative band at 700nm and 580 nm are assigned to a broadening induced by carriers.[163,175-178] The shift of the two positive peak maximums has been previously reported and assigned to the presence of free charges. In addition, at early time, a redshift of the absorption due to excitons induced bandgap renormalizations was also reported.[178,179] Publications

on TA experiments of MoS_2 focuses on the early time dynamics. The excited state of MoS_2 in the time window is thus very well described. The blue shift of the PB peaks is assigned to free carriers in the conduction band.[167] The signal of the exciton bleaching and the free carrier is spectrally very close. As the exciton decays in 100's of picoseconds, only the free carrier remains, effectively shifting the signal over time.

The negative band below the PB is a photoinduced absorption(PIA) by the free carrier. Population analysis previously reported assigned a longer than recorded signals with a time constant over 1ns to free carrier. However, to the best of our knowledge, there is no report of optical experiments going beyond a few nanoseconds that monitor the complete signal of the carriers.
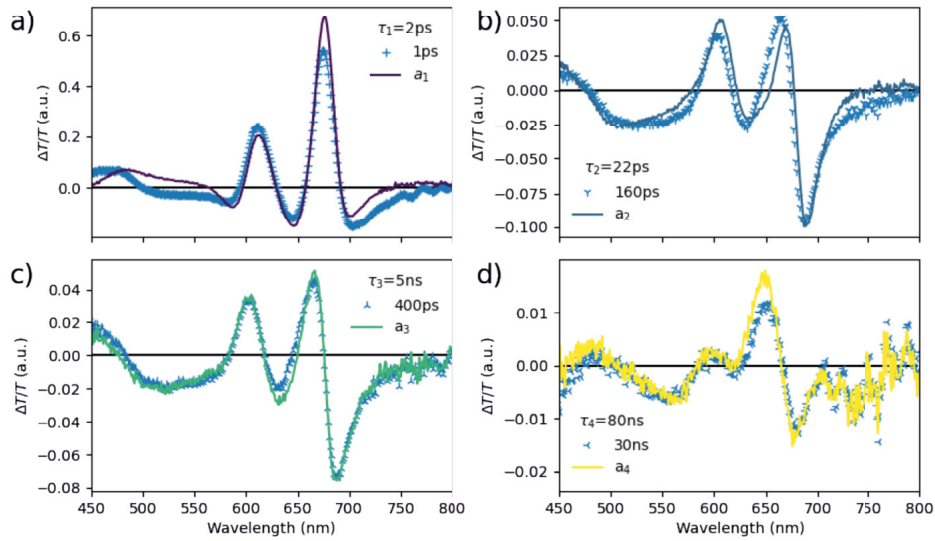
5.1.3 Global analysis

Figure 5.1-3: Global analysis results of the MoS_2 TA experiment done with a sum of four exponential decays. Each amplitude is displayed in one quadrant with the respective lifetime and an overlay of the MoS_2 spectra at a selected delay.

To deconvolute the dynamic of the different photogenerated species, a global analysis

using four exponentials has been performed(eq.5.1).

$$y(\lambda, t) = a_1(\lambda)e^{-\frac{t}{\tau_1}} + a_2(\lambda)e^{-\frac{t}{\tau_2}} + a_3(\lambda)e^{-\frac{t}{\tau_3}} + a_4(\lambda)e^{-\frac{t}{\tau_4}} \qquad (5.1)$$

It consists in fitting the decay at each wavelength with the same time constants, only fitting the amplitude (pre-exponential factor) of the different exponential. With this method we can identify the different processes involve and their related amplitude and time constant. A sum of four exponential was necessary to fit the signal over the complete time range. Figure 5.1-3a)-d) present the different amplitude of each exponential of the global analysis. Following the fit using four exponential, we extract four time constants related to each. The lifetimes are listed in Table 5.1-1 After the rise of the signal, we can

τ_1	τ_2	τ_3	τ_4
2ps	22ps	5ns	80ns

Table 5.1-1: Table of lifetime of the global analysis

identify a first, fast, relaxation of a picosecond (∼2ps), a second, intermediate, relaxation of tens of picosecond (∼22ps), a third, slow, process of a few nanoseconds (∼5ns) and finally a fourth, very slow, close to a hundred nanoseconds (∼80ns). Looking at figure 5.1-3 we can see that each lifetime can represent the complete spectra at different delays backing the correctness of the fit. More specifically quadrant a) of figure 5.1-3 shows that the amplitude of exp_1 with a lifetime of 1ps match reasonably well the spectra at 1p delay. Similarly quadrant b)-d) each present in order of increased lifetime the match with an increased delayed spectrum. Looking at photo-bleaching of excitons A at 675nm, we can see that quadrant a) shows a positive amplitude. Moving along quadrant b),c) and d) we can see the amplitude going negative. The previous report of the short timescale dynamics(up to 1ns) of MoS_2 combined with this phenomenon tells us that the first two lifetimes of the global analysis are related to the exciton.[163, 164] More precisely to excitons

cooling, excitons trapping in bellow gap states and recombination. As formerly mentions, free carriers are expected to have a negative signal and are responsible for the spectral shift we see in figure 5.1-2d). The Transition from a positive signal to a negative close to the exciton bleaching peak is thus assigned the result of free carrier. Following the logic, the two slower lifetimes of the global analysis, 5ns and 80ns, both being negative around the exciton photo-bleaching peak, can be assigned to the free carrier dynamics.
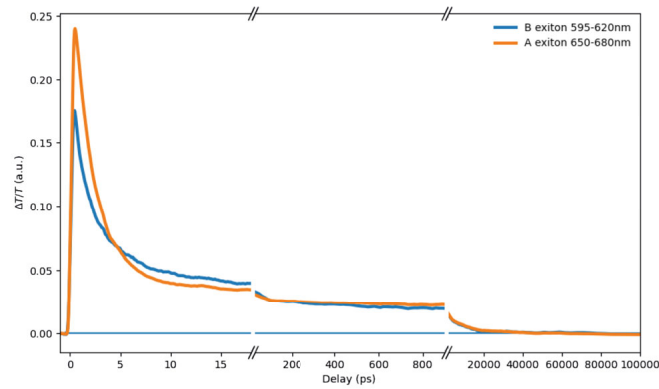
Figure 5.1-4: Average for the A and B exciton signal between 650-680nm and 595-620nm respectively

Figure 5.1-4 displays the average of the signals between 650-680nm corresponding to the A exciton photo-bleaching peak and between 595-620nm for the B exciton PB centered around tree time scales. At an early time, 0-20ps, it shows the rise of both exciton and the early decay. The two signals are, as expected, following different dynamics. In the second timescale, 20ps-1ns, the two dynamics become more similar. Finally, in the last time scale, 1ns-100ns, the two signal are the same. The transition from different dynamics to a similar one suggests that the underlying phenomena resulting in the signal changes. The two excitons are responsible for the different early time dynamics. This is in perfect agreement with literature. The longest time, however, has not been under investigation. So far, the proposed phenomena behind signal longer than 1ns in MoS2 was free carriers. The similitude in the dynamics comforts the assignment of the slowest lifetime to the

dynamics of free carriers. Nonetheless, accrediting an exact mechanism for the two time constant are impossible. Possible explanations can be proposed. Of course, a trivial explanation would be that trapping is at the origin of the late time dynamics. But we can go further. Given that our flakes are less than 100nm in lateral size and that exciton diffusion was reported to be more the 300nm, it is very likely that an exciton can diffuse to the edge of the flakes. Thus, it is reasonable to suggest that at least one of the two slow time-constants is related to an edge state/trap.[180,181] A complementary explanation that would explain the two different time constant, is the presence of metallic states at the edge of the flake. It has been reported that depending on the type of edge, the electronic properties of the latter change and can have metallic characteristics.[182] A metallic state would explain the longest time constant as a charge in this state could last up to μs. The different edge types could result in different edge states with different related lifetimes. Finally the distribution of flake thikness showing some bimodal character(see figure S5.1-1), the two time constants could be the result of two "sets" of flack thicknesses.

5.2 Conclusion

In this chapter, we have explored the dynamic of photo-generated carriers in few-layers nanoflakes of MoS_2. We have measured, to our knowledge, for the first time, the complete dynamics from excitation of complete recombination of carriers in MoS_2. Four time-constants were extracted using a global analysis. The fastest two were assigned to exciton dynamics and the slowest two to free carrier. Different explanations regarding free carrier recombination have been proposed involving different types of edge states and flake sizes yielding different time constants. The comprehension of the carrier dynamics in MoS_2 is a must have for use in a PSC device. The device being dominated by free carrier, it is crucial to understand how they will behave when interacting the material bulk or edge. This can enable a smarter buffer material design leading to an improve stability and efficiency of perovskite solar cells.

CHAPTER 6

Conclusions and Outlooks

This thesis was aimed at the exploration and comprehension of the 2D perovskite as a new material for optoelectronic device. More specifically, understanding the carrier dynamics to better leverage the increased stability of the material to improve HOPVs. I start with Chapter 2 describing the methods and analysis tools used to probe materials. Chapter 3 follows by the in-depth exploration of new 2D perovskite carrier dynamics. After that, Chapter 4 focuses on the interface of 2D perovskite with 3D perovskite for improved device characteristics. Chapter 5 explores the dynamics of the free carriers of in few layer MoS_2 nanoflakes

More in detail,chapter 2 introduces the spectroscopic methods used to probe the material. It briefly describes the working principle and use case for the optical steady state techniques. It continues by an in-depth description of time-resolved absorption spectroscopy(TAS). What this technique is all about as well as what it allows to uncover in the studied material. Along TAS, the fluorescence decay measurement (TCSPC) is also detailed. Finally, this chapter introduced the analytical method for processing the data from TAS as well as models to interpret it.

Chapter 3 starts by introducing a set of new 2D perovskite made with highly fluorined cations. It explores the mechanical as well as optical properties of this fluorined 2d

perovskite family. The stability as well as excitonic properties are explored. Following that, the chapter moves to the extensive analysis of one member of the 2D fluorined perovskite called A43. Here, ultrafast spectroscopy and electro-absorption, revealing the presence of long-lasting correlated electron–hole pairs. Such states have a marked charge-transfer character, as revealed by the persistent Stark effect in the form of a second derivative in electro-absorption. This effect is the result of the unique fluorinated cation electrostatic effect as well as the steric hindrance of the later.

Chapter 4 follows with studies on 2D/3D bilayer. It starts by reviling the impact of 2D crystal alignment on top of the 2D in driving interface charge-recombination dynamics. The 2D crystal growth and orientation are manipulated by specific fluorination of phenethylammonium (PEA), used here as the organic cation backbone of the 2D component. By means of time-resolved optoelectronic analysis from the femto- to microsecond regions, we demonstrate a static function of the 2D layer as an electron barrier and homogeneous surface passivant, together with a dynamic role in retarding back charge recombination. Furthermore, we have explored the evolution of the 2D/3D interface and revealed that the leaking of MA in the 2D layer is undeniably a mechanism to prevent for highly efficient solar cells. This study reveals that larger cations perform better in this regard and should be considered in the development of future highly efficient and stable solar cells. Consecutively, the thermal stress on 2D-3D cells were studied using X-ray scattering and by thermally cycling cells. We revealed that the 2D perovskite crystal layer undergoes a structural transformation to a higher dimensional, and at the same time protects the 3D layer underneath.

Chapter 5 offers a study on the excited state dynamics of MoS_2, a member of the 2D layer transition metal dichalcogenide, very similar in structure to the 2D perovskites with the potential to replace transport layer. We have explored the entire excited state dynamics, from picosecond up to the complete decay of carriers 10 microseconds later. We have uncovered for the first time a lifetime for free carriers and proposed a recombination mechanism involving edge state giving rise to different time constants.

Summing up, during the last four years I have studied new 2D perovskites designed to be more water resistant. I have reviled the unique excited state of this new 2D perovskite. Then, I have studied the interface of 2D with 3D perovskite, showing the importance of the choice of cation and its impact on bilayer cell performance. Alongside this, I have inquired lead-free perovskite for devices and finally I have probed the long-lived excited state of MoS_2.

Looking forward, I believe that the incorporation of the 2D perovskite in or on the 3D perovskite will become the norm for high efficiency devices and most likely the way forward for a commercial HOPV. This, of course, lies on the fundamental understanding of the optoelectronic properties of 2D and 3d perovskites. From this fundamental understanding of the photophysics of these materials will arise the best synergy for the integration of one with the other. I can see that new, fine-tuned 2D perovskites will be designed with specific properties to accomplish its task in the most optimal way. The synergistic nature of the relationship between 2D perovskite and 3D perovskite renders the integration of one to the other make it the path to follow for a transition toward a commercial product and make HOPV the solar technology of the 21st century.

CHAPTER 7

Acknowledgement

First of all, I would like to thank Pr.Giulia Grancini and Pr.Mohammad Khaja Nazeeruddin for allowing me to pursue my PhD in the GMF group. I would like to thank them for supervision and guidance throughout my research. I would like to thank my colleagues for their invaluable contribution, help in my research as well as their cheerfulness, making my stay in GMF truly enjoyable.

A special mention to Albertus Sutanto and Ines Benito-Garcia for their scientific contributions, to Alexander Fedorovskiy for the everlasting scientific discussion and exploration of the local climbing area, to Nadja for our joyful discussions, and of course Géraldine and Isabel, our administrative secretaries for their incredible help,invaluable assistance,cheerful discussion, and general good spirit.

I would like to acknowledge all EPFL Valais team, from Robin and Stephan from the mechanical workshop, Patrick from the electronic workshop, Cédric and Jean from the IT department, and Laurent and Annabelle from the chemical store for the valuable help along my four years stay.

Finally, I would like to thanks my family and friends for supporting throughout my studies and my PhD for so many year. This is the end of a long academic journey that started on the September 2012 at the bachelor introduction day. Without the support of

my parents this would not have been possible. Without my friend Alex, Corine, Gontran and Matthieu to only name a few this journey would have not been as fun. And Without my love the future would not have looked so bright.

CHAPTER 8

Bibliography

[1] Meyer L.A. and R.K. Pachauri. Climate Change 2014: Synthesis Report. Contribution of Working Groups I, II and III to the Fifth Assessment Report of the Intergovernmental Panel on Climate Change. Technical report, IPCC, Geneva,Switzerland, 2014.

[2] Sander A. Mann, Mariska J. De Wild-Scholten, Vasilis M. Fthenakis, Wilfried G.J.H.M. Van Sark, and Wim C. Sinke. The energy payback time of advanced crystalline silicon PV modules in 2020: A prospective study, 11 2014.

[3] NREL. Best Research-Cell Efficiency Chart.

[4] Jian Gong, Seth B. Darling, and Fengqi You. Perovskite photovoltaics: Life-cycle assessment of energy and environmental impacts. *Energy and Environmental Science*, 8(7):1953–1968, 7 2015.

[5] P A M D Irac. On the theory of quantum mechanics. *Proceedings of the Royal Society of London. Series A, Containing Papers of a Mathematical and Physical Character*, 112(762):661–677, 10 1926.

[6] Alberto Zannoni. On the Quantization of the Monoatomic Ideal Gas. *arXiv: Statistical Mechanics*, 12 1999.

[7] N. F. Mott. Conduction in polar crystals. II. The conduction band and ultra-violet absorption of alkali-halide crystals. *Transactions of the Faraday Society*, 34(0):500–506, 1 1938.

[8] Gregory H. Wannier. The structure of electronic excitation levels in insulating crystals. *Physical Review*, 52(3):191–197, 8 1937.

[9] J. Frenkel. On the transformation of light into heat in solids. i. *Physical Review*, 37(1):17–44, 1931.

[10] D. L. Dexter and Mark (Anthony Mark) Fox. *Optical properties of solids*, volume 7. Oxford University Press, 2nd edition, 2010.

[11] R. J. Elliott. Intensity of optical absorption by excitons. *Physical Review*, 108(6):1384–1389, 12 1957.

[12] R. N. Hall. Electron-hole recombination in germanium [21], 7 1952.

[13] W. Shockley and W. T. Read. Statistics of the recombinations of holes and electrons. *Physical Review*, 87(5):835–842, 9 1952.

[14] George Hamilton and Hugo Sanabria. Multiparameter fluorescence spectroscopy of single molecules. In *Spectroscopy and Dynamics of Single Molecules*, chapter 6, pages 269–333. Elsevier, 2019.

[15] R. Paschotta. Band gap. In *Encyclopedia of Laser Physics and Technology*. Wiley-VCH, 2008.

[16] Mark Fox and Radu Ispasoiu. Quantum Wells, Superlattices, and Band-Gap Engineering. In *Springer Handbook of Electronic and Photonic Materials*, pages 1021–1040. Springer US, 2006.

[17] R Tsu and L Esaki. Superlatice and negative differential conductivity in semiconductor. *IBM Journal of Research and Development*, 14(1):61–65, 1970.

[18] Severin N. Habisreutinger, Nakita K. Noel, and Henry J. Snaith. Hysteresis Index: A Figure without Merit for Quantifying Hysteresis in Perovskite Solar Cells. *ACS Energy Letters*, 3(10):2472–2476, 2018.

[19] William Shockley and Hans J. Queisser. Detailed balance limit of efficiency of p-n junction solar cells. *Journal of Applied Physics*, 32(3):510–519, 3 1961.

[20] P C Choubey, A Oudhia, and R Dewangan. Recent research in science and technology : an international refereed journal for all aspects of science research. *Recent Research in Science and Technology*, 4(8):99–101, 2009.

[21] Shruti Sharma, Kamlesh Kumar Jain, and Ashutosh Sharma. Solar Cells: In Research and Applications—A Review. *Materials Sciences and Applications*, 06(12):1145–1155, 12 2015.

[22] Akihiro Kojima, Kenjiro Teshima, Yasuo Shirai, and Tsutomu Miyasaka. Organometal halide perovskites as visible-light sensitizers for photovoltaic cells. *Journal of the American Chemical Society*, 131(17):6050–6051, 5 2009.

[23] Carlo Motta, Fedwa El-Mellouhi, Sabre Kais, Nouar Tabet, Fahhad Alharbi, and Stefano Sanvito. Revealing the role of organic cations in hybrid halide perovskite CH3 NH3PbI3. *Nature Communications*, 6(1):1–7, 4 2015.

[24] V. M. Goldschmidt. Die Gesetze der Krystallochemie. *Die Naturwissenschaften*, 14(21):477–485, 5 1926.

[25] Federico Brivio, Keith T. Butler, Aron Walsh, and Mark Van Schilfgaarde. Relativistic quasiparticle self-consistent electronic structure of hybrid halide perovskite photovoltaic absorbers. *Physical Review B - Condensed Matter and Materials Physics*, 89(15):155204, 4 2014.

[26] Constantinos C. Stoumpos, Christos D. Malliakas, and Mercouri G. Kanatzidis. Semiconducting tin and lead iodide perovskites with organic cations: Phase transitions, high mobilities, and near-infrared photoluminescent properties. *Inorganic Chemistry*, 52(15):9019–9038, 8 2013.

[27] Aurélien M.A. Leguy, Pooya Azarhoosh, M. Isabel Alonso, Mariano Campoy-Quiles, Oliver J. Weber, Jizhong Yao, Daniel Bryant, Mark T. Weller, Jenny Nelson, Aron Walsh, Mark Van Schilfgaarde, and Piers R.F. Barnes. Experimental and theoretical optical properties of methylammonium lead halide perovskites. *Nanoscale*, 8(12):6317–6327, 3 2016.

[28] Anna Amat, Edoardo Mosconi, Enrico Ronca, Claudio Quarti, Paolo Umari, Md K. Nazeeruddin, Michael Gratzel, and Filippo De Angelis. Cation-induced band-gap tuning in organohalide perovskites: Interplay of spin-orbit coupling and octahedra tilting. *Nano Letters*, 14(6):3608–3616, 6 2014.

[29] Samuel D. Stranks and Paulina Plochocka. The influence of the Rashba effect. *Nature Materials*, 17(5):381–382, 5 2018.

[30] Fan Zheng, Liang Z. Tan, Shi Liu, and Andrew M. Rappe. Rashba spin-orbit coupling enhanced carrier lifetime in CH 3 NH 3 PbI 3. *Nano Letters*, 15(12):7794–7800, 12 2015.

[31] Thomas Kirchartz and Uwe Rau. Decreasing Radiative Recombination Coefficients via an Indirect Band Gap in Lead Halide Perovskites. *Journal of Physical Chemistry Letters*, 8(6):1265–1271, 3 2017.

[32] Qianqian Lin, Ardalan Armin, Ravi Chandra Raju Nagiri, Paul L. Burn, and Paul Meredith. Electro-optics of perovskite solar cells. *Nature Photonics*, 9(2):106–112, 2 2015.

[33] Kenichiro Tanaka, Takayuki Takahashi, Takuma Ban, Takashi Kondo, Kazuhito Uchida, and Noboru Miura. Comparative study on the excitons in lead-halide-based perovskite-type crystals CH3NH3PbBr3 CH3NH 3PbI3. *Solid State Communications*, 127(9-10):619–623, 9 2003.

[34] Valerio D'Innocenzo, Giulia Grancini, Marcelo J.P. P. Alcocer, Ajay Ram Srimath Kandada, Samuel D. Stranks, Michael M. Lee, Guglielmo Lanzani, Henry J. Snaith, Annamaria Petrozza, Valerio D'Innocenzo, Giulia Grancini, Marcelo J.P. P. Alcocer, Ajay Ram Srimath Kandada, Samuel D. Stranks, Michael M. Lee, Guglielmo Lanzani, Henry J. Snaith, and Annamaria Petrozza. Excitons versus free charges in organo-lead tri-halide perovskites. *Nature Communications*, 5(1), 4 2014.

[35] Michele Saba, Francesco Quochi, Andrea Mura, and Giovanni Bongiovanni. Excited State Properties of Hybrid Perovskites. *Accounts of Chemical Research*, 49(1):166–173, 1 2016.

[36] S. B. Nam, D. C. Reynolds, C. W. Litton, R. J. Almassy, T. C. Collins, and C. M. Wolfe. Free-exciton energy spectrum in GaAs. *Physical Review B*, 13(2):761–767, 1 1976.

[37] Ho-Wa Li, Zhiqiang Guan, Yuanhang Cheng, Taili Lui, Qingdan Yang, Chun-Sing Lee, Song Chen, and Sai-Wing Tsang. On the Study of Exciton Binding Energy with Direct Charge Generation in Photovoltaic Polymers. *Advanced Electronic Materials*, 2(11):1600200, 11 2016.

[38] NREL. National Renewable Energy Laboratory, 2020.

[39] Handong Jin, Elke Debroye, Masoumeh Keshavarz, Ivan G. Scheblykin, Maarten B J Roeffaers, Johan Hofkens, Julian A. Steele, Maarten B.J. Roeffaers, Johan Hofkens, and Julian A. Steele. No Title, 2 2020.

[40] Mehran Samiee, Siva Konduri, Balaji Ganapathy, Ranjith Kottokkaran, Hisham A. Abbas, Andrew Kitahara, Pranav Joshi, Liang Zhang, Max Noack, and Vikram Dalal. Defect density and dielectric constant in perovskite solar cells. *Applied Physics Letters*, 105(15), 2014.

[41] Zhenyi Ni, Chunxiong Bao, Ye Liu, Qi Jiang, Wu Qiang Wu, Shangshang Chen, Xuezeng Dai, Bo Chen, Barry Hartweg, Zhengshan Yu, Zachary Holman, and Jin-song Huang. Resolving spatial and energetic distributions of trap states in metal halide perovskite solar cells. *Science*, 367(6484):1352–1358, 2020.

[42] Fang Yuan, Zhaoxin Wu, Hua Dong, Jun Xi, Kai Xi, Giorgio Divitini, Bo Jiao, Xun Hou, Shufeng Wang, and Qihuang Gong. High Stability and Ultralow Threshold Amplified Spontaneous Emission from Formamidinium Lead Halide Perovskite Films. *Journal of Physical Chemistry C*, 121(28):15318–15325, 2017.

[43] M. H. Chan, S. K. So, K. T. Chan, and F. G. Kellert. Defect density measurements of low temperature grown molecular beam epitaxial GaAs by photothermal deflection spectroscopy. *Applied Physics Letters*, 67(6):834–836, 1995.

[44] David B. Mitzi. Templating and structural engineering in organic-inorganic perovskites. *Journal of the Chemical Society, Dalton Transactions*, 1(1):1–12, 1 2001.

[45] Teruya Ishihara, Jun Takahashi, and Takenari Goto. Optical properties due to electronic transitions in two-dimensional semiconductors (CnH2n+1NH3)2PbI4. *Physical Review B*, 42(17):11099–11107, 12 1990.

[46] T. Ishihara, X. Hong, J. Ding, and A. V. Nurmikko. Dielectric confinement effect for exciton and biexciton states in PbI4-based two-dimensional semiconductor structures. *Surface Science*, 267(1-3):323–326, 1 1992.

[47] Marine E. F. Bouduban, Valentin I. E. Queloz, Valentina M. Caselli, Kyung Taek Cho, Ahmad R. Kirmani, Sanghyun Paek, Cristina Roldan-Carmona, Lee J. Richter, Jacques E. Moser, Tom J. Savenije, Mohammad Khaja Nazeeruddin, and Giulia Grancini. Crystal Orientation Drives the Interface Physics at Two/Three-Dimensional Hybrid Perovskites. *The Journal of Physical Chemistry Letters*, pages 5713–5720, 9 2019.

[48] Kyung Taek Cho, Yi Zhang, Simonetta Orlandi, Marco Cavazzini, Iwan Zimmermann, Andreas Lesch, Nouar Tabet, Gianluca Pozzi, Giulia Grancini, and Mohammad Khaja Nazeeruddin. Water-Repellent Low-Dimensional Fluorous Perovskite as Interfacial Coating for 20% Efficient Solar Cells. *Nano Letters*, 18(9):5467–5474, 8 2018.

[49] Yuri I. Dolzhenko, Tamotsu Inabe, and Yusei Maruyama. In Situ X-Ray Observation on the Intercalation of Weak Interaction Molecules into Perovskite-Type Layered Crystals (C9H19NH3)2PbI4 and (C10H21NH3)2CdCl4, 1986.

[50] Teruya Ishihara, Jun Takahashi, and Takenari Goto. Exciton state in two-dimensional perovskite semiconductor (C10H21NH3)2PbI4. *Solid State Communications*, 69(9):933–936, 3 1989.

[51] Juan Tirado, Cristina Roldán Carmona, Fabio A. Muñoz Guerrero, Gemay Bonilla Arboleda, Maryline Ralaiarisoa, Giulia Grancini, Valentin I.E. Queloz, Norbert Koch, Mohammad Khaja Nazeeruddin, and Franklin Jaramillo. Copper sulfide nanoparticles as hole-transporting-material in a fully-inorganic blocking layers n-i-p perovskite solar cells: Application and working insights. *Applied Surface Science*, 478:607–614, 6 2019.

[52] Michael M. Lee, Joël Teuscher, Tsutomu Miyasaka, Takurou N. Murakami, and Henry J. Snaith. Efficient hybrid solar cells based on meso-superstructured organometal halide perovskites. *Science*, 338(6107):643–647, 11 2012.

[53] Fabrizio Giordano, Antonio Abate, Juan Pablo Correa Baena, Michael Saliba, Taisuke Matsui, Sang Hyuk Im, Shaik M. Zakeeruddin, Mohammad Khaja Nazeeruddin, Anders Hagfeldt, and Michael Graetzel. Enhanced electronic properties in mesoporous TiO2 via lithium doping for high-efficiency perovskite solar cells. *Nature Communications*, 7:1–6, 2016.

[54] Chun Huang, Peng Lin, Nianqing Fu, Chang Liu, Baomin Xu, Kaiwen Sun, Danyang Wang, Xierong Zeng, and Shanming Ke. Facile fabrication of highly efficient ETL-free perovskite solar cells with 20% efficiency by defect passivation and interface engineering. *Chemical Communications*, 55(19):2777–2780, 2019.

[55] Timur Sh. Atabaev. Stable HTM-free organohalide perovskite-based solar cells. *Materials Today: Proceedings*, 4(3):4919–4923, 2017.

[56] Zeinab Safari, Mahmood Borhani Zarandi, and Mohamad Reza Nateghi. Improved environmental stability of HTM free perovskite solar cells by a modified deposition route. *Chemical Papers*, 73(11):2667–2678, 2019.

[57] Giulia Grancini, C. Roldán-Carmona, I. Zimmermann, E. Mosconi, X. Lee, D. Martineau, S. Narbey, F. Oswald, F. De Angelis, M. Graetzel, and Mohammad Khaja Nazeeruddin. One-Year stable perovskite solar cells by 2D/3D interface engineering. *Nature Communications*, 8:15684, 6 2017.

[58] J. Tauc, R. Grigorovici, and A. Vancu. Optical Properties and Electronic Structure of Amorphous Germanium. *physica status solidi (b)*, 15(2):627–637, 1966.

[59] Eline M. Hutter, Giles E. Eperon, Samuel D. Stranks, and Tom J. Savenije. Charge Carriers in Planar and Meso-Structured Organic-Inorganic Perovskites: Mobilities, Lifetimes, and Concentrations of Trap States. *Journal of Physical Chemistry Letters*, 6(15):3082–3090, 8 2015.

[60] Samuel D. Stranks, Victor M. Burlakov, Tomas Leijtens, James M. Ball, Alain Goriely, and Henry J. Snaith. Recombination Kinetics in Organic-Inorganic Perovskites: Excitons, Free Charge, and Subgap States. *Physical Review Applied*, 2(3):034007, 9 2014.

[61] D. H.K. Murthy, Armantas Melianas, Zheng Tang, Gytis Juška, Kestutis Arlauskas, Fengling Zhang, Laurens D.A. Siebbeles, Olle Inganäs, and Tom J. Savenije. Origin of reduced bimolecular recombination in blends of conjugated polymers and fullerenes. *Advanced Functional Materials*, 23(34):4262–4268, 9 2013.

[62] Kenichiro Tanaka, Takayuki Takahashi, Takashi Kondo, Kenichi Umeda, Kazuhiro Ema, Tsutomu Umebayashi, Keisuke Asai, Kazuhito Uchida, and Noboru Miura. Electronic and excitonic structures of inorganic-organic perovskite-type quantum-well crystal (C4H9NH3)2PbBr4. *Japanese Journal of Applied Physics, Part 1: Regular Papers and Short Notes and Review Papers*, 44(8):5923–5932, 2005.

[63] E. A. Muljarov, S. G. Tikhodeev, N. A. Gippius, and Teruya Ishihara. Excitons in self-organized semiconductor/insulator superlattices: PbI-based perovskite compounds. *Physical Review B*, 51(20):14370–14378, 5 1995.

[64] Jacky Even, Laurent Pedesseau, and Claudine Katan. Understanding quantum confinement of charge carriers in layered 2D hybrid perovskites. *ChemPhysChem*, 15(17):3733–3741, 12 2014.

[65] Claudine Katan, Nicolas Mercier, and Jacky Even. Quantum and Dielectric Confinement Effects in Lower-Dimensional Hybrid Perovskite Semiconductors. *Chemical Reviews*, 119(5):3140–3192, 3 2019.

[66] F. O. Saouma, C. C. Stoumpos, J. Wong, M. G. Kanatzidis, and J. I. Jang. Selective enhancement of optical nonlinearity in two-dimensional organic-inorganic lead iodide perovskites. *Nature Communications*, 8(1):742, 12 2017.

[67] Yaxin Zhai, Sangita Baniya, Chuang Zhang, Junwen Li, Paul Haney, Chuan-Xiang Xiang Sheng, Eitan Ehrenfreund, and Zeev Valy Vardeny. Giant Rashba splitting in 2D organic-inorganic halide perovskites measured by transient spectroscopies. *Science Advances*, 3(7), 7 2017.

[68] Eric Amerling, Sangita Baniya, Evan Lafalce, Chuang Zhang, Zeev Valy Vardeny, and Luisa Whittaker-Brooks. Electroabsorption Spectroscopy studies of (C4H9NH3)2PbI4 Organic-Inorganic Hybrid Perovskite Multiple Quantum-Wells. *The Journal of Physical Chemistry Letters*, 8(18):4557–4564, 9 2017.

[69] D. A B Miller, D. S. Chemla, T. C. Damen, A. C. Gossard, W. Wiegmann, T. H. Wood, and C. A. Burrus. Band-edge electroabsorption in quantum well structures: The quantum-confined stark effect. *Physical Review Letters*, 53(22):2173–2176, 1984.

114

[70] Inés García-Benito, Claudio Quarti, Valentin I.E. Queloz, Simonetta Orlandi, Iwan Zimmermann, Marco Cavazzini, Andreas Lesch, Sergio Marras, David Beljonne, Gianluca Pozzi, Mohammad Khaja Nazeeruddin, and Giulia Grancini. Fashioning Fluorous Organic Spacers for Tunable and Stable Layered Hybrid Perovskites. *Chemistry of Materials*, 30(22):8211–8220, 11 2018.

[71] J.A Gladysz and Dennis P Curran. Fluorous chemistry: from biphasic catalysis to a parallel chemical universe and beyond. *Tetrahedron*, 58(20):3823–3825, 5 2002.

[72] John A. Gladysz, Dennis P. Curran, and István T. Horváth. *Handbook of fluorous chemistry*. Wiley-VCH Verlag GmbH & Co. KGaA, 2005.

[73] David B. Mitzi, David R. Medeiros, and Patrick R.L. Malenfant. Intercalated organic-inorganic perovskites stabilized by fluoroaryl-aryl interactions. *Inorganic Chemistry*, 41(8):2134–2145, 4 2002.

[74] Y. Wei, J. S. Lauret, L. Galmiche, P. Audebert, and E. Deleporte. Strong exciton-photon coupling in microcavities containing new fluorophenethylamine based perovskite compounds. *Optics Express*, 20(9):10399, 4 2012.

[75] Y. Wei, P. Audebert, L. Galmiche, J. S. Lauret, and E. Deleporte. Synthesis, optical properties and photostability of novel fluorinated organic-inorganic hybrid (R-NH3)2PbX4 semiconductors. *Journal of Physics D: Applied Physics*, 46(13):135105, 4 2013.

[76] Yi Wei, Pierre Audebert, Laurent Galmiche, Jean Sébastien Lauret, and Emmanuelle Deleporte. Photostability of 2D organic-inorganic hybrid perovskites. *Materials*, 7(6):4789–4802, 2014.

[77] Claudia Lermer, Susanne T. Birkhold, Igor L. Moudrakovski, Peter Mayer, Leslie M. Schoop, Lukas Schmidt-Mende, and Bettina V. Lotsch. Toward fluorinated spacers for MAPI-derived hybrid perovskites: Synthesis, characterization, and phase transitions of (FC2H4NH3)2PbCl4. *Chemistry of Materials*, 28(18):6560–6566, 9 2016.

[78] Enzheng Shi, Yao Gao, Blake P. Finkenauer, A. Akriti, Aidan H. Coffey, and Letian Dou. Two-dimensional halide perovskite nanomaterials and heterostructures, 8 2018.

[79] Constantinos C. Stoumpos, Duyen H. Cao, Daniel J. Clark, Joshua Young, James M. Rondinelli, Joon I. Jang, Joseph T. Hupp, and Mercouri G. Kanatzidis. Ruddlesden-Popper Hybrid Lead Iodide Perovskite 2D Homologous Semiconductors. *Chemistry of Materials*, 28(8):2852–2867, 5 2016.

[80] Andreas Pospischil, Marco M. Furchi, and Thomas Mueller. Solar-energy conversion and light emission in an atomic monolayer p-n diode. *Nature Nanotechnology*, 9(4):257–261, 2014.

[81] Isabella Poli, Salvador Eslava, and Petra Cameron. Tetrabutylammonium cations for moisture-resistant and semitransparent perovskite solar cells. *Journal of Materials Chemistry A*, 5(42):22325–22333, 2017.

[82] Shivam Singh, Bosky Sharma, Gangadhar Banappanavar, Amrita Dey, Sudip Chakraborty, K. L. Narasimhan, Parag Bhargava, and Dinesh Kabra. Investigation on Organic Molecule Additive for Moisture Stability and Defect Passivation via Physisorption in CH3NH3PbI3 Based Perovskite. *ACS Applied Energy Materials*, 1(5):1870–1877, 5 2018.

[83] Duyen H Cao, Constantinos C Stoumpos, Omar K Farha, Joseph T Hupp, and Mercouri G Kanatzidis. 2D Homologous Perovskites as Light-Absorbing Materials for Solar Cell Applications. *Journal of the American Chemical Society*, 137(24):7843–7850, 2015.

[84] Lingling Mao, Hsinhan Tsai, Wanyi Nie, Lin Ma, Jino Im, Constantinos C. Stoumpos, Christos D. Malliakas, Feng Hao, Michael R. Wasielewski, Aditya D. Mohite, and Mercouri G. Kanatzidis. Role of Organic Counterion in Lead- and Tin-Based Two-Dimensional Semiconducting Iodide Perovskites and Application in Planar Solar Cells. *Chemistry of Materials*, 28(21):7781–7792, 11 2016.

[85] G. A. Mousdis, G. C. Papavassiliou, C. P. Raptopoulou, and A. Terzis. Preparation and characterization of [H3N(CH2)6NH3]PbI4 and similar compounds with a layered perovskite structure. *Journal of Materials Chemistry*, 10(2):515–518, 2000.

[86] K. Gauthron, J-S. Lauret, L. Doyennette, G. Lanty, A. Al Choueiry, S. J. Zhang, A. Brehier, L. Largeau, O. Mauguin, J. Bloch, and E. Deleporte. Optical spectroscopy of two-dimensional layered (C_6H_5C_2H_4-NH_3)_2-PbI_4 perovskite. *Optics Express*, 18(6):5912, 3 2010.

[87] Naoki Kawano, Masanori Koshimizu, Yan Sun, Natsuna Yahaba, Yutaka Fujimoto, Takayuki Yanagida, and Keisuke Asai. Effects of organic moieties on luminescence properties of organic-inorganic layered perovskite-type compounds. *Journal of Physical Chemistry C*, 118(17):9101 9106, 5 2014.

[88] Machteld E. Kamminga, Hong-Hua Fang, Marina R. Filip, Feliciano Giustino, Jacob Baas, Graeme R. Blake, Maria Antonietta Loi, and Thomas T. M. Palstra. Confinement Effects in Low-Dimensional Lead Iodide Perovskite Hybrids. *Chemistry of Materials*, 28(13):4554–4562, 7 2016.

[89] R. T. Williams and K. S. Song. The self-trapped exciton. *Journal of Physics and Chemistry of Solids*, 51(7):679–716, 1990.

[90] Edward P. Booker, Tudor H. Thomas, Claudio Quarti, Michael R. Stanton, Cameron D. Dashwood, Alexander J. Gillett, Johannes M. Richter, Andrew J. Pearson, Nathaniel J.L.K. Davis, Henning Sirringhaus, Michael B. Price, Neil C. Greenham, David Beljonne, Siân E. Dutton, and Felix Deschler. Formation of Long-Lived Color Centers for Broadband Visible Light Emission in Low-Dimensional Layered Perovskites. *Journal of the American Chemical Society*, 139(51):18632–18639, 2017.

[91] Ke Zhao Du, Qing Tu, Xu Zhang, Qiwei Han, Jie Liu, Stefan Zauscher, and David B. Mitzi. Two-Dimensional Lead(II) Halide-Based Hybrid Perovskites Templated by Acene Alkylamines: Crystal Structures, Optical Properties, and Piezoelectricity. *Inorganic Chemistry*, 56(15):9291–9302, 8 2017.

[92] Yi Zhang, Giulia Grancini, Zhaofu Fei, Erfan Shirzadi, Xuehui Liu, Emad Oveisi, Farzaneh Fadaei Tirani, Rosario Scopelliti, Yaqing Feng, Mohammad Khaja Nazeeruddin, Paul J. Dyson, Mohammad Khaja Nazeeruddin, and Paul J. Dyson. No Title. *Nano Energy*, 58:105–111, 4 2019.

[93] Matthew D. Smith, Adam Jaffe, Emma R. Dohner, Aaron M. Lindenberg, and Hemamala I. Karunadasa. Structural origins of broadband emission from layered Pb-Br hybrid perovskites. *Chemical Science*, 8(6):4497–4504, 2017.

[94] Vishwanath H. Dalvi and Peter J. Rossky. Molecular origins of fluorocarbon hydrophobicity. *Proceedings of the National Academy of Sciences of the United States of America*, 107(31):13603–13607, 8 2010.

[95] Sarah Decato, Troy Bemis, Eric Madsen, and Sandro Mecozzi. Synthesis and characterization of perfluoro tert butyl semifluorinated amphiphilic polymers and their potential application in hydrophobic drug delivery. *Polymer Chemistry*, 5(22):6461–6471, 11 2014.

[96] Valentin I.E. Queloz, Marine E.F. Bouduban, Ines García-Benito, Alexander Fedorovskiy, Simonetta Orlandi, Marco Cavazzini, Gianluca Pozzi, Harsh Trivedi, Doru C. Lupascu, David Beljonne, Jaques E. Moser, Mohammad Khaja Nazeeruddin, Claudio Quarti, and Giulia Grancini. Spatial Charge Separation as the Origin of Anomalous Stark Effect in Fluorous 2D Hybrid Perovskites. *Advanced Functional Materials*, 30(28):2000228, 7 2020.

[97] Hadis Morkoc. *Handbook of Nitride Semiconductors and Devices*, volume 1. Wiley-VCH Verlag GmbH & Co. KGaA, 3 2009.

[98] Xiaoyang Zhu, Nicholas R. Monahan, Zizhou Gong, Haiming Zhu, Kristopher W. Williams, and Cory A. Nelson. Charge Transfer Excitons at van der Waals Interfaces. *Journal of the American Chemical Society*, 137(26):8313–8320, 7 2015.

[99] Jean-Marc Vincent. Recent advances of fluorous chemistry in material sciences. *Chemical Communications*, 48(93):11382, 10 2012.

[100] Stefanie Neutzner, Félix Thouin, Daniele Cortecchia, Annamaria Petrozza, Carlos Silva, and Ajay Ram Srimath Kandada. Exciton-polaron spectral structures in two-dimensional hybrid lead-halide perovskites. *Physical Review Materials*, 2018.

[101] Félix Thouin, David A. Valverde Chávez, Claudio Quarti, Daniele Cortecchia, Ilaria Bargigia, David Beljonne, Annamaria Petrozza, Carlos Silva, Ajay Ram Srimath Kandada, David A. Valverde-Chávez, Claudio Quarti, Daniele Cortecchia, Ilaria Bargigia, David Beljonne, Annamaria Petrozza, Carlos Silva, and Ajay Ram Srimath Kandada. Phonon coherences reveal the polaronic character of excitons in two-dimensional lead-halide perovskites. *Nature Materials*, 18(4):349–356, 4 2018.

[102] Vidya Kattoor, Kamlesh Awasthi, Efat Jokar, Eric Wei-Guang Guang Diau, and Nobuhiro Ohta. Integral Method Analysis of Electroabsorption Spectra and Electrophotoluminescence Study of (C4H9NH3)2PbI4 Organic-Inorganic Quantum Well. *The Journal of Physical Chemistry C*, 122(46):26623–26634, 11 2018.

[103] M. A. G. Halliwell. Handbook of semiconductors. Vol. 2. Optical properties of solids edited by M. Balkanski. *Journal of Applied Crystallography*, 13(6):637–638, 12 1980.

[104] G. Walters, M. Wei, O. Voznyy, R. Quintero-Bermudez, A. Kiani, D.-M. Smilgies, R. Munir, A. Amassian, S. Hoogland, and E. Sargent. The quantum-confined Stark effect in layered hybrid perovskites mediated by orientational polarizability of confined dipoles. *Nature Communications*, 9(1):4214, 2018.

[105] Kenichiro Tanaka, Takayuki Takahashi, Takashi Kondo, Tsutomu Umebayashi, Keisuke Asai, and Kazuhiro Ema. Image charge effect on two-dimensional excitons in an inorganic-organic quantum-well crystal. *Physical Review B - Condensed Matter and Materials Physics*, 71(4):045312, 2005.

[106] Paolo Giannozzi, Stefano Baroni, Nicola Bonini, Matteo Calandra, Roberto Car, Carlo Cavazzoni, Davide Ceresoli, Guido L. Chiarotti, Matteo Cococcioni, Ismaila Dabo, Andrea Dal Corso, Stefano De Gironcoli, Stefano Fabris, Guido Fratesi, Ralph Gebauer, Uwe Gerstmann, Christos Gougoussis, Anton Kokalj, Michele Lazzeri, Layla Martin-Samos, Nicola Marzari, Francesco Mauri, Riccardo Mazzarello, Stefano Paolini, Alfredo Pasquarello, Lorenzo Paulatto, Carlo Sbraccia, Sandro Scandolo, Gabriele Sclauzero, Ari P. Seitsonen, Alexander Smogunov, Paolo Umari, and Renata M. Wentzcovitch. QUANTUM ESPRESSO: A modular and open-source software project for quantum simulations of materials. *Journal of Physics Condensed Matter*, 21(39), 2009.

[107] David G. Billing and Andreas Lemmerer. Synthesis, characterization and phase transitions in the inorganic-organic layered perovskite-type hybrids [(Cn H2n + 1NH 3)2PbI4], n = 4, 5 and 6. *Acta Crystallographica Section B: Structural Science*, 63(5):735–747, 9 2007.

[108] Jeremy L. Knutson, James D. Martin, and David B. Mitzi. Tuning the band gap in hybrid tin iodide perovskite semiconductors using structural templating. *Inorganic Chemistry*, 44(13):4699–4705, 6 2005.

[109] Laurent Pedesseau, Daniel Sapori, Boubacar Traore, Roberto Robles, Hong Hua Fang, Maria Antonietta Loi, Hsinhan Tsai, Wanyi Nie, Jean Christophe Blancon, Amanda Neukirch, Sergei Tretiak, Aditya D. Mohite, Claudine Katan, Jacky Even, and Mikaël Kepenekian. Advances and Promises of Layered Halide Hybrid Perovskite Semiconductors. *ACS Nano*, 10(11):9776–9786, 2016.

[110] Claudio Quarti, Nadège Marchal, and David Beljonne. Tuning the Optoelectronic Properties of Two-Dimensional Hybrid Perovskite Semiconductors with Alkyl Chain Spacers. *Journal of Physical Chemistry Letters*, 9(12):3416–3424, 6 2018.

[111] Luigi Bonati and Michele Parrinello. Silicon Liquid Structure and Crystal Nucleation from Ab Initio Deep Metadynamics. *Physical Review Letters*, 121(26):265701, 12 2018.

[112] Maria Monica Castellanos, Arnold McAuley, and Joseph E. Curtis. Investigating Structure and Dynamics of Proteins in Amorphous Phases Using Neutron Scattering. *Computational and Structural Biotechnology Journal*, 15:117–130, 1 2017.

[113] Claudio Quarti, Edoardo Mosconi, James M. Ball, Valerio D'Innocenzo, Chen Tao, Sandeep Pathak, Henry J. Snaith, Annamaria Petrozza, and Filippo De Angelis. Structural and optical properties of methylammonium lead iodide across the tetragonal to cubic phase transition: Implications for perovskite solar cells. *Energy and Environmental Science*, 9(1):155–163, 1 2016.

[114] Elizabeth Brunk and Ursula Rothlisberger. Mixed Quantum Mechanical/Molecular Mechanical Molecular Dynamics Simulations of Biological Systems in Ground and Electronically Excited States. *Chemical Reviews*, 115(12):6217–6263, 2015.

[115] Hyosung Choi, Jaeki Jeong, Hak Beom Kim, Seongbeom Kim, Bright Walker, Gi Hwan Kim, and Jin Young Kim. Cesium-doped methylammonium lead iodide perovskite light absorber for hybrid solar cells. *Nano Energy*, 7:80–85, 7 2014.

[116] Claudio Quarti, Edoardo Mosconi, and Filippo De Angelis. Structural and electronic properties of organo-halide hybrid perovskites from ab initio molecular dynamics. *Physical Chemistry Chemical Physics*, 17(14):9394–9409, 4 2015.

[117] Silvia G. Motti, Daniele Meggiolaro, Samuele Martani, Roberto Sorrentino, Alex J. Barker, Filippo De Angelis, and Annamaria Petrozza. Defect Activity in Lead Halide Perovskites, 11 2019.

[118] Tik Lun Leung, Ho Won Tam, Fangzhou Liu, Jingyang Lin, Alan Man Ching Ng, Wai Kin Chan, Wei Chen, Zhubing He, Ivor Lončarić, Luca Grisanti, Chao Ma, Kam Sing Wong, Ying Suet Lau, Furong Zhu, Željko Skoko, Jasminka Popović, and Aleksandra B. Djurišić. Mixed Spacer Cation Stabilization of Blue-Emitting n = 2 Ruddlesden–Popper Organic–Inorganic Halide Perovskite Films. *Advanced Optical Materials*, 8(4):1901679, 2 2019.

[119] Alexander W. Achtstein, Anatol V. Prudnikau, Maxim V. Ermolenko, Leonid I. Gurinovich, Sergey V. Gaponenko, Ulrike Woggon, Alexander V. Baranov, Mikhail Yu. Leonov, Ivan D. Rukhlenko, Anatoly V. Fedorov, and Mikhail V. Artemyev. Electroabsorption by 0D, 1D, and 2D nanocrystals: A comparative study of CdSe colloidal quantum dots, nanorods, and nanoplatelets. *ACS Nano*, 8(8):7678–7686, 8 2014.

[120] Yani Chen, Yong Sun, Jiajun Peng, Junhui Tang, Kaibo Zheng, and Ziqi Liang. 2D Ruddlesden–Popper Perovskites for Optoelectronics. *Advanced Materials*, 30(2):1703487, 1 2018.

[121] Kyung Tack Cho, Giulia Grancini, Yonghui Lee, Emad Oveisi, Jaehoon Ryu, Osbel Almora, Manuel Tschumi, Pascal Alexander Schouwink, Gabseok Seo, Sung Heo, Jucheol Park, Jyongsik Jang, Sanghyun Paek, Germà Garcia-Belmonte, and Mohammad Khaja Nazeeruddin. Selective growth of layered perovskites for stable and efficient photovoltaics. *Energy and Environmental Science*, 11(4):952–959, 4 2018.

[122] Giulia Grancini, Ajay Ram Srimath Kandada, Jarvist M. Frost, Alex J. Barker, Michele De Bastiani, Marina Gandini, Sergio Marras, Guglielmo Lanzani, Aron Walsh, and Annamaria Petrozza. Role of microstructure in the electron-hole interaction of hybrid lead halide perovskites. *Nature Photonics*, 2015.

[123] Qi Jiang, Yang Zhao, Xingwang Zhang, Xiaolei Yang, Yong Chen, Zema Chu, Qiufeng Ye, Xingxing Li, Zhigang Yin, and Jingbi You. Surface passivation of perovskite film for efficient solar cells. *Nature Photonics*, 13(7):460–466, 7 2019.

[124] Eline M. Hutter, Jan-Jaap Jaap Hofman, Michiel L. Petrus, Michiel Moes, Ruben D. Abellón, Pablo Docampo, and Tom J. Savenije. Charge Transfer from Methylammonium Lead Iodide Perovskite to Organic Transport Materials: Efficiencies, Transfer Rates, and Interfacial Recombination. *Advanced Energy Materials*, 7(13):1602349, 7 2017.

[125] Roberto Brenes, Dengyang Guo, Anna Osherov, Nakita K. Noel, Christopher Eames, Eline M. Hutter, Sandeep K. Pathak, Farnaz Niroui, Richard H. Friend, M. Saiful Islam, Henry J. Snaith, Vladimir Bulović, Tom J. Savenije, and Samuel D. Stranks. Metal Halide Perovskite Polycrystalline Films Exhibiting Properties of Single Crystals. *Joule*, 1(1):155–167, 9 2017.

[126] Shuyan Shao, Jian Liu, Giuseppe Portale, Hong-Hua Hua Fang, Graeme R. Blake, Gert H. ten Brink, L. Jan Anton Koster, and Maria Antonietta Loi. Highly Reproducible Sn-Based Hybrid Perovskite Solar Cells with 9% Efficiency. *Advanced Energy Materials*, 8(4):1702019, 2 2018.

[127] Ryosuke Arai, Masahiro Yoshizawa-Fujita, Yuko Takeoka, and Masahiro Rikukawa. Orientation Control of Two-Dimensional Perovskites by Incorporating Carboxylic Acid Moieties. *ACS Omega*, 2(5):2333–2336, 5 2017.

[128] Xinqian Zhang, Gang Wu, Shida Yang, Weifei Fu, Zhongqiang Zhang, Chen Chen, Wenqing Liu, Jielin Yan, Weitao Yang, and Hongzheng Chen. Vertically Oriented 2D Layered Perovskite Solar Cells with Enhanced Efficiency and Good Stability. *Small*, 13(33):1700611, 9 2017.

[129] Alexander Z. Chen, Michelle Shiu, Jennifer H. Ma, Matthew R. Alpert, Depei Zhang, Benjamin J. Foley, Detlef M. Smilgies, Seung Hun Lee, and Joshua J. Choi. Origin of vertical orientation in two-dimensional metal halide perovskites and its effect on photovoltaic performance. *Nature Communications*, 9(1):1–7, 2018.

[130] Lingling Mao, Constantinos C. Stoumpos, and Mercouri G. Kanatzidis. Two-Dimensional Hybrid Halide Perovskites: Principles and Promises. *Journal of the American Chemical Society*, 141(3):1171–1190, 1 2019.

[131] Albertus A. Sutanto, Nikita Drigo, Valentin I.E. Queloz, Inés Garcia-Benito, Ahmad R. Kirmani, Lee J. Richter, Pascal A. Schouwink, Kyung Tack Cho, Sanghyun Paek, Mohammad Khaja Nazeeruddin, and Giulia Grancini. Dynamical evolution of the 2D/3D interface: A hidden driver behind perovskite solar cell instability. *Journal of Materials Chemistry A*, 8(5):2343–2348, 2020.

[132] Albertus A. Sutanto, Rodrigo Szostak, Nikita Drigo, Valentin I.E. Queloz, P. E. Marchezi, J. C. Germino, Hélio C.N. Tolentino, Mohammad Khaja Nazeeruddin, Ana Flavia Nogueira, and Giulia Grancini. In Situ Analysis Reveals the Role of 2D Perovskite in Preventing Thermal-Induced Degradation in 2D/3D Perovskite Interfaces. *Nano Letters*, 20(5):3992–3998, 5 2020.

[133] Wei Peng, Jun Yin, Kang Ting Ho, Olivier Ouellette, Michele De Bastiani, Banavoth Murali, Omar El Tall, Chao Shen, Xiaohe Miao, Jun Pan, Erkki Alarousu, Jr Hau He, Boon S. Ooi, Omar F. Mohammed, Edward Sargent, and Osman M. Bakr. Ultralow Self-Doping in Two-dimensional Hybrid Perovskite Single Crystals. *Nano Letters*, 17(8):4759–4767, 2017.

[134] Silvia G. Motti, Timothy Crothers, Rong Yang, Yu Cao, Renzhi Li, Michael B. Johnston, Jianpu Wang, and Laura M. Herz. Heterogeneous Photon Recycling and Charge Diffusion Enhance Charge Transport in Quasi-2D Lead-Halide Perovskite Films. *Nano Letters*, 19(6):3953–3960, 6 2019.

[135] Giulia Grancini, Sergio Marras, Mirko Prato, Cinzia Giannini, Claudio Quarti, Filippo De Angelis, Michele De Bastiani, Giles E. Eperon, Henry J. Snaith, Liberato Manna, and Annamaria Petrozza. The impact of the crystallization processes on the structural and optical properties of hybrid perovskite films for photovoltaics. *Journal of Physical Chemistry Letters*, 5(21):3836–3842, 11 2014.

[136] Li Na Quan, Mingjian Yuan, Riccardo Comin, Oleksandr Voznyy, Eric M. Beauregard, Sjoerd Hoogland, Andrei Buin, Ahmad R. Kirmani, Kui Zhao, Aram Amassian, Dong Ha Kim, and Edward H. Sargent. Ligand-Stabilized Reduced-Dimensionality Perovskites. *Journal of the American Chemical Society*, 138(8):2649–2655, 3 2016.

[137] Raphael F. Moral, Luiz Gustavo Bonato, José Carlos Germino, Willian Xerxes Coelho Oliveira, Rupini Kamat, Junwei Xu, Christopher J. Tassone, Samuel D. Stranks, Michael F. Toney, and Ana Flávia Nogueira. Synthesis of Polycrystalline Ruddlesden-Popper Organic Lead Halides and Their Growth Dynamics. *Chemistry of Materials*, 31(22):9472–9479, 11 2019.

[138] Saikumar Nair and Jignasa V. Gohel. A Review on Contemporary Hole Transport Materials for Perovskite Solar Cells. In *Green Energy and Technology*, pages 145–168. Springer Science and Business Media Deutschland GmbH, 2020.

[139] Muge Acik and Seth B. Darling. Graphene in perovskite solar cells: Device design, characterization and implementation. *Journal of Materials Chemistry A*, 4(17):6185–6235, 4 2016.

[140] Selvakumar Pitchaiya, Muthukumarasamy Natarajan, Agilan Santhanam, Vijayshankar Asokan, Akila Yuvapragasam, Venkatraman Madurai Ramakrishnan, Subramaniam E. Palanisamy, Senthilarasu Sundaram, and Dhayalan Velauthapillai. A review on the classification of organic/inorganic/carbonaceous hole transporting materials for perovskite solar cell application. *Arabian Journal of Chemistry*, 13(1):2526–2557, 1 2020.

[141] Nitesh Kumar Singh, Anshul Agarwal, Tirupathiraju Kanumuri, and Tarun Varshney. A study of an inorganic-organic HTM on the implementation of lead based PSC Device. In *2020 IEEE Students' Conference on Engineering and Systems, SCES 2020*. Institute of Electrical and Electronics Engineers Inc., 7 2020.

[142] Leyla Najafi, Babak Taheri, Beatriz Martín-García, Sebastiano Bellani, Diego Di Girolamo, Antonio Agresti, Reinier Oropesa-Nuñez, Sara Pescetelli, Luigi Vesce, Emanuele Calabrò, Mirko Prato, Antonio E. Del Rio Castillo, Aldo Di Carlo, and Francesco Bonaccorso. MoS2 Quantum Dot/Graphene Hybrids for Advanced Interface Engineering of a CH3NH3PbI3 Perovskite Solar Cell with an Efficiency of over 20%. *ACS Nano*, 12(11):10736–10754, 11 2018.

[143] Hai Li, Jumiati Wu, Zongyou Yin, and Hua Zhang. Preparation and applications of mechanically exfoliated single-layer and multilayer MoS2 and WSe2 nanosheets. *Accounts of Chemical Research*, 47(4):1067–1075, 2014.

[144] Wensi Zhang, Panpan Zhang, Zhiqiang Su, and Gang Wei. Synthesis and sensor applications of MoS2-based nanocomposites. *Nanoscale*, 7(44):18364–18378, 2015.

[145] Xiaoyun Yu, Mathieu S. Prévot, Néstor Guijarro, and Kevin Sivula. Self-assembled 2D WSe 2 thin films for photoelectrochemical hydrogen production. *Nature Communications*, 6(May), 2015.

[146] Xiaoyun Yu, Mathieu S. Prévot, and Kevin Sivula. Multiflake thin film electronic devices of solution processed 2D MoS2 enabled by sonopolymer assisted exfoliation and surface modification. *Chemistry of Materials*, 26(20):5892–5899, 2014.

[147] Qing Hua Wang, Kourosh Kalantar-Zadeh, Andras Kis, Jonathan N. Coleman, and Michael S. Strano. Electronics and optoelectronics of two-dimensional transition metal dichalcogenides. *Nature Nanotechnology*, 7(11):699–712, 2012.

[148] K S Novoselov, D Jiang, F Schedin, T J Booth, V V Khotkevich, S V Morozov, and A K Geim. Two-dimensional atomic crystals. *Proceedings of the National Academy of Sciences of the United States of America*, 102(30):10451–10453, 2005.

[149] B. Radisavljevic, A. Radenovic, J. Brivio, V. Giacometti, and A. Kis. Single-layer MoS2 transistors. *Nature Nanotechnology*, 6(3):147–150, 2011.

[150] H. S.S. Ramakrishna Matte, A. Gomathi, Arun K. Manna, Dattatray J. Late, Ranjan Datta, Swapan K. Pati, and C. N.R. Rao. MoS2 and WS2 analogues of graphene. *Angewandte Chemie - International Edition*, 49(24):4059–4062, 2010.

[151] Branimir Radisavljevic, Michael Brian Whitwick, and Andras Kis. Integrated circuits and logic operations based on single-layer MoS 2. *ACS Nano*, 5(12):9934–9938, 2011.

[152] Yijin Zhang, Jianting Ye, Yusuke Matsuhashi, and Yoshihiro Iwasa. Ambipolar MoS 2 thin flake transistors. *Nano Letters*, 12(3):1136–1140, 2012.

[153] Andrea Splendiani, Liang Sun, Yuanbo Zhang, Tianshu Li, Jonghwan Kim, Chi Yung Chim, Giulia Galli, and Feng Wang. Emerging photoluminescence in monolayer MoS2. *Nano Letters*, 10(4):1271–1275, 2010.

[154] A. K. Geim and I. V. Grigorieva. Van der Waals heterostructures. *Nature*, 499(7459):419–425, 2013.

[155] Marco Bernardi, Maurizia Palummo, and Jeffrey C. Grossman. Extraordinary sunlight absorption and one nanometer thick photovoltaics using two-dimensional monolayer materials. *Nano Letters*, 13(8):3664–3670, 2013.

[156] Xiaoping Hong, Jonghwan Kim, Su Fei Shi, Yu Zhang, Chenhao Jin, Yinghui Sun, Sefaattin Tongay, Junqiao Wu, Yanfeng Zhang, and Feng Wang. Ultrafast charge transfer in atomically thin MoS2/WS2 heterostructures. *Nature Nanotechnology*, 9(9):682 686, 2014.

[157] Andrea Capasso, Fabio Matteocci, Leyla Najafi, Mirko Prato, Joka Buha, Lucio Cinà, Vittorio Pellegrini, Aldo Di Carlo, and Francesco Bonaccorso. Few-Layer MoS $_2$ Flakes as Active Buffer Layer for Stable Perovskite Solar Cells. *Advanced Energy Materials*, 6(16):1600920, 8 2016.

[158] Saman Kohnehpoushi, Pariya Nazari, Bahram Abdollahi Nejand, and Mehdi Eskandari. MoS2: A two-dimensional hole-transporting material for high-efficiency, low-cost perovskite solar cells. *Nanotechnology*, 29(20):205201, 3 2018.

[159] Kin Fai Mak, Changgu Lee, James Hone, Jie Shan, and Tony F. Heinz. Atomically thin MoS2: A new direct-gap semiconductor. *Physical Review Letters*, 105(13):2–5, 2010.

[160] Edbert J. Sie, Alex J. Frenzel, Yi Hsien Lee, Jing Kong, and Nuh Gedik. Inter-valley biexcitons and many-body effects in monolayer MoS2. *Physical Review B - Condensed Matter and Materials Physics*, 92(12):1–8, 2015.

[161] C. H. Lui, A. J. Frenzel, D. V. Pilon, Y. H. Lee, X. Ling, G. M. Akselrod, J. Kong, and N. Gedik. Trion-induced negative photoconductivity in monolayer MoS2. *Physical Review Letters*, 113(16):1–5, 2014.

[162] Saptarshi Das, Hong Yan Chen, Ashish Verma Penumatcha, and Joerg Appenzeller. High performance multilayer MoS2 transistors with scandium contacts. *Nano Letters*, 13(1):100–105, 2013.

[163] Hongyan Shi, Rusen Yan, Simone Bertolazzi, Jacopo Brivio, Bo Gao, Andras Kis, Debdeep Jena, Huili Grace Xing, and Libai Huang. Exciton dynamics in suspended monolayer and few-layer MoS2 2D crystals. *ACS Nano*, 7(2):1072–1080, 2013.

[164] Sangwan Sim, Jusang Park, Jeong Gyu Song, Chihun In, Yun Shik Lee, Hyungjun Kim, and Hyunyong Choi. Exciton dynamics in atomically thin MoS2: Interexcitonic interaction and broadening kinetics. *Physical Review B - Condensed Matter and Materials Physics*, 88(7):1–5, 2013.

[165] Haining Wang, Changjian Zhang, and Farhan Rana. Ultrafast dynamics of defect-assisted electron-hole recombination in monolayer MoS2. *Nano Letters*, 15(1):339–345, 2015.

[166] J. Kopaczek, M. P. Polak, P. Scharoch, K. Wu, B. Chen, S. Tongay, and R. Kudrawiec. Direct optical transitions at K- and H-point of Brillouin zone in bulk MoS2, MoSe2, WS2, and WSe2. *Journal of Applied Physics*, 119(23):235705, 6 2016.

[167] Weijie Zhao, R. M. Ribeiro, Minglin Toh, Alexandra Carvalho, Christian Kloc, A. H. Castro Neto, and Goki Eda. Origin of indirect optical transitions in few-layer MoS2, WS2, and WSe2. *Nano Letters*, 13(11):5627–5634, 11 2013.

[168] H. Zhang, S. B. Lu, J. Zheng, J. Du, S. C. Wen, D. Y. Tang, and K. P. Loh. Molybdenum disulfide (MoS_2) as a broadband saturable absorber for ultra-fast photonics. *Optics Express*, 22(6):7249, 3 2014.

[169] Sebastiano Bellani, Leyla Najafi, Andrea Capasso, Antonio Esau Del Rio Castillo, Maria Rosa Antognazza, and Francesco Bonaccorso. Few-layer MoS2flakes as a hole-selective layer for solution-processed hybrid organic hydrogen-evolving photocathodes. *Journal of Materials Chemistry A*, 5(9):4384–4396, 7 2017.

[170] Leyla Najafi, Sebastiano Bellani, Beatriz Martín-García, Reinier Oropesa-Nunez, Antonio Esau Del Rio Castillo, Mirko Prato, Iwan Moreels, and Francesco Bonaccorso. Solution-Processed Hybrid Graphene Flake/2H-MoS2 Quantum Dot Heterostructures for Efficient Electrochemical Hydrogen Evolution. *Chemistry of Materials*, 29(14):5782–5786, 2017.

[171] Antonio Agresti, Sara Pescetelli, Alessandro Lorenzo Palma, Beatriz Martín-García, Leyla Najafi, Sebastiano Bellani, Iwan Moreels, Mirko Prato, Francesco Bonaccorso, and Aldo Di Carlo. Two-Dimensional Material Interface Engineering for Efficient Perovskite Large-Area Modules. *ACS Energy Letters*, 4(8):1862–1871, 8 2019.

[172] Hai Li, Zongyou Yin, Qiyuan He, Hong Li, Xiao Huang, Gang Lu, Derrick Wen Hui Fam, Alfred Iing Yoong Tok, Qing Zhang, and Hua Zhang. Fabrication of Single- and Multilayer MoS2 Film-Based Field-Effect Transistors for Sensing NO at Room Temperature. *Small*, 8(1):63–67, 1 2012.

[173] Yi-Hsien Lee, Xin-Quan Zhang, Wenjing Zhang, Mu-Tung Chang, Cheng-Te Lin, Kai-Di Chang, Ya-Chu Yu, Jacob Tse-Wei Wang, Chia-Seng Chang, Lain-Jong Li, and Tsung-Wu Lin. Synthesis of Large-Area MoS ₂ Atomic Layers with Chemical Vapor Deposition. *Advanced Materials*, 24(17):2320–2325, 5 2012.

[174] Leyla Najafi, Sebastiano Bellani, Reinier Oropesa-Nuñez, Alberto Ansaldo, Mirko Prato, Antonio Esau Del Rio Castillo, and Francesco Bonaccorso. Engineered MoSe ₂ -Based Heterostructures for Efficient Electrochemical Hydrogen Evolution Reaction. *Advanced Energy Materials*, 8(16):1703212, 6 2018.

[175] Demetra Tsokkou, Xiaoyun Yu, Kevin Sivula, and Natalie Banerji. The Role of Excitons and Free Charges in the Excited-State Dynamics of Solution-Processed Few-Layer MoS2 Nanoflakes. *Journal of Physical Chemistry C*, 120(40):23286–23292, 10 2016.

[176] Zhaogang Nie, Run Long, Linfeng Sun, Chung Che Huang, Jun Zhang, Qihua Xiong, Daniel W. Hewak, Zexiang Shen, Oleg V. Prezhdo, and Zhi Heng Loh. Ultrafast carrier thermalization and cooling dynamics in few-layer MoS2. *ACS Nano*, 8(10):10931–10940, 2014.

[177] Kyle J. Czech, Blaise J. Thompson, Schuyler Kain, Qi Ding, Melinda J. Shearer, Robert J. Hamers, Song Jin, and John C. Wright. Measurement of Ultrafast Excitonic Dynamics of Few-Layer MoS2 Using State-Selective Coherent Multidimensional Spectroscopy. *ACS Nano*, 9(12):12146–12157, 2015.

[178] Tetiana Borzda, Christoph Gadermaier, Natasa Vujicic, Peter Topolovsek, Milos Borovsak, Tomaz Mertelj, Daniele Viola, Cristian Manzoni, Eva A.A. Pogna, Daniele Brida, Maria Rosa Antognazza, Francesco Scotognella, Guglielmo Lanzani, Giulio Cerullo, and Dragan Mihailovic. Charge photogeneration in few-layer MoS2. *Advanced Functional Materials*, 25(22):3351–3358, 2015.

[179] Paul D. Cunningham, Kathleen M. McCreary, Aubrey T. Hanbicki, Marc Currie, Berend T. Jonker, and L. Michael Hayden. Charge Trapping and Exciton Dynamics in Large-Area CVD Grown MoS2. *Journal of Physical Chemistry C*, 120(10):5819–5826, 2016.

[180] Ali Javey, Shiekh Zia Uddin, Hyungjin Kim, Monica Lorenzon, Matthew Yeh, Der Hsien Lien, Edward S. Barnard, Han Htoon, and Alexander Weber-Bargioni. Neutral exciton diffusion in monolayer MoS2. *ACS Nano*, 14(10):13433–13440, 2020.

[181] J. Huang, M. Lorenzon, J. H. Kang, P. Chen, X. Duan, E. Barnard, C. W. Wong, and A. Weber-Bargioni. Exciton Diffusion in a Monolayer MoS2-WS2 Lateral Heterostructure. *2019 Conference on Lasers and Electro-Optics, CLEO 2019 - Proceedings*, 2:29–30, 2019.

[182] Miguel Tinoco, Louis Maduro, and Sonia Conesa-Boj. Metallic edge states in zig-zag vertically-oriented MoS2 nanowalls. *Scientific Reports*, 9(1):1–7, 2019.

[183] David Vanderbilt. Soft self-consistent pseudopotentials in a generalized eigenvalue formalism. *Physical Review B*, 41(11):7892–7895, 1990.

[184] John P. Perdew, Kieron Burke, and Matthias Ernzerhof. Generalized gradient approximation made simple. *Physical Review Letters*, 77(18):3865–3868, 1996.

[185] Stefan Grimme. Semiempirical GGA-type density functional constructed with a long-range dispersion correction. *Journal of Computational Chemistry*, 27(15):1787–1799, 11 2006.

[186] Hendrik J. Monkhorst and James D. Pack. Special points for Brillouin-zone integrations. *Physical Review B*, 13(12):5188–5192, 1976.

[187] M. J. Frisch, G. W. Trucks, H. B. Schlegel, G. E. Scuseria, M. A. Robb, J. R. Cheeseman, G. Scalmani, V. Barone, G. A. Petersson, H. Nakatsuji, X. Li, M. Caricato, A. V. Marenich, J. Bloino, B. G. Janesko, R. Gomperts, B. Mennucci, H. P. Hratchian, J. V. Fox, and D. J. Fox. Gaussian 16 Revison C01, 2016.

[188] Jessica E Kroeze, Tom J. Savenije, and Martien J. W. Vermeulen. Contactless Determination of the Photoconductivity Action Spectrum, Exciton Diffusion Length, and Charge Separation Efficiency in Polythiophene-Sensitized TiO 2 Bilayers. *The Journal of Physical Chemistry B*, 107:7696–7705, 2003.

CHAPTER 9

List of publications

1. Sutanto, A. A. et al. Isomeric Carbazole-Based Hole-Transporting Materials: Role of the Linkage Position on the Photovoltaic Performance of Perovskite Solar Cells. Chem. Mater. 33, 3286–3296 (2021).

2. Romano, V. et al. Two-Step Thermal Annealing: An Effective Route for 15 % Efficient Quasi-2D Perovskite Solar Cells. Chempluschem 1–6 (2021). doi:10.1002/cplu. 202000777

3. Sutanto, A. A. et al. Phosphine Oxide Derivative as a Passivating Agent to Enhance the Performance of Perovskite Solar Cells. ACS Appl. Energy Mater. (2021). doi:10.1021/ acsaem. 0c02472

4. Fedorovskiy, A. E., Queloz, V. I. E. & Nazeeruddin, M. K. Beyond Tolerance Factor : Using Deep Learning for Prediction Formability of ABX3 Perovskite Structures. Adv. Theory Simulations 1–6 (2021). doi:10.1002/adts.202100021

5. Kanda, H. et al. Band-bending induced passivation: High performance and stable perovskite solar cells using a perhydropoly(silazane) precursor. Energy Environ. Sci. (2020). doi:10.1039/c9ee02028d

6. Xia, R. et al. An Efficient Approach to Fabricate Air-Stable Perovskite Solar Cells via Addition of a Self-Polymerizing Ionic Liquid. Adv. Mater. (2020). doi:10.1002/adma.202003801

7. Kim, H. et al. Self-Crystallized Multifunctional 2D Perovskite for Efficient and Stable Perovskite Solar Cells. Adv. Funct. Mater. 30, 1910620 (2020).

8. García-Benito, I. et al. Fluorination of Organic Spacer Impacts on the Structural and Optical Response of 2D Perovskites. Front. Chem. (2020). doi:10.3389/ fchem. 2019.00946

9. Pisanu, A. et al. Exploring the role of halide mixing in lead-free BZA2SnX4 two dimensional hybrid perovskites. J. Mater. Chem. A 8, 1875–1886 (2020).

10. Chiara, R. et al. Green-Emitting Lead-Free Cs4SnBr6 Zero-Dimensional Perovskite Nanocrystals with Improved Air Stability. J. Phys. Chem. Lett. 11, 618–623 (2020).

11. Sutanto, A. A. et al. In Situ Analysis Reveals the Role of 2D Perovskite in Preventing Thermal-Induced Degradation in 2D/3D Perovskite Interfaces. Nano Lett. 20, 3992–3998 (2020).

12. Queloz, V. I. E. et al. Spatial Charge Separation as the Origin of Anomalous Stark Effect in Fluorous 2D Hybrid Perovskites. Adv. Funct. Mater. 30, 2000228 (2020).

13. Sutanto, A. A. et al. Dynamical evolution of the 2D/3D interface: A hidden driver behind perovskite solar cell instability. J. Mater. Chem. A 8, 2343–2348 (2020).

14. Bouduban, M. E. F. et al. Crystal Orientation Drives the Interface Physics at Two/Three-Dimensional Hybrid Perovskites. J. Phys. Chem. Lett. 5713–5720 (2019). doi:10.1021/acs.jpclett.9b02224

15. Cho, K. T. et al. Perovskite Solar Cells: 18% Efficiency Using Zn(II) and Cu(II) Octakis(diarylamine)phthalocyanines as Hole-Transporting Materials. ACS Appl. Energy Mater. (2019). doi:10.1021/acsaem.9b00637

16. Tirado, J. et al. Copper sulfide nanoparticles as hole-transporting-material in a fully-inorganic blocking layers n-i-p perovskite solar cells: Application and working insights. Appl. Surf. Sci. 478, 607–614 (2019).

17. Sutanto, A. A. et al. Pushing the limit of Cs incorporation into FAPbBr3 perovskite to enhance solar cells performances. APL Mater. 7, (2019).

18. García-Benito, I. et al. Fashioning Fluorous Organic Spacers for Tunable and Stable Layered Hybrid Perovskites. Chem. Mater. 30, 8211–8220 (2018).

19. Lee, H. J. et al. A Facile Preparative Route of Nanoscale Perovskites over Mesoporous Metal Oxide Films and Their Applications to Photosensitizers and Light Emitters. Adv. Funct. Mater. 1803801 (2018). doi:10.1002/adfm.201803801

20. Pantaler, M. et al. Hysteresis-Free Lead-Free Double-Perovskite Solar Cells by Interface Engineering. ACS Energy Lett. 3, 1781–1786 (2018).

CHAPTER 10

Appendix

S3.1 Fashioning Fluorous Organic Spacers for Tunable and Stable Layered Hybrid Perovskites

S3.1.1 Materials and Methods

All available chemicals and solvents were purchased from commercial sources and were used without any further purification. (N-hydroxyalkyl)amino phthalimides 1a-c,69,70 N-allyl phthalimide 3,71 and 2-(4,4,5,5,6,6,7,7,8,8,9,9,9-tridecafluoro- 2-iodo-nonyl)-isoindole-1,3-dione 472 were prepared as described in the literature. Reactions were monitored by thin layer chromatog- raphy (TLC) that was conducted on plates precoated with silica gel Si 60-F254 (Merck, Germany). Column chromatography was conducted by using silica gel Si 60, 230-400 mesh, 0.040-0.063 mm (Merck, Darmstadt, Germany). 1H and 13C NMR spectra were recorded on a Bruker Avance 400 (400 and 100.6 MHz, respectively); chemical shifts are indicated in parts per million downfield from SiMe4, using the residual proton ($CHCl_3$ = 7.26 ppm, CHD_2SOCD_3 = 2.50 ppm, CHD2OD = 3.33 ppm) and carbon ($CDCl_3$ = 77.0 ppm, (CD3)2SO = 40.45 ppm, CD3OD = 49.10 ppm) solvent resonances as the internal reference. 19F NMR spectra were recorded on a Bruker AC 300

spectrometer (282 MHz) and a Bruker Avance 400 (377 MHz). Coupling constant values J are given in Hz. Elemental analyses were carried out by the Departmental Service of Microanalysis.

UV-vis Absorption. UV-Vis steady-state absorption spectra were acquired with a Perkins Elmer lambda 950s UV/Vis spectrophotometer using an integrating sphere to account for optical losses outside of the active layer.

Photoluminescence. Steady state and time resolved photoluminescence measurement where carried out on Horiba a Fluorolog-3, with a PMT as detector. The excitation source for the TCSPC is a Horiba nanoLED- 370 with an excitation wavelength of 369 nm, a pulse duration of 1.3 ns and a repetition rate of 100 KHz. PL at different intensity was performed using an Expla PL 2230 laser coupled to a PG400 OPG. The spectra are recorded with a Horiba synapse CCD detector coupled to a monochromator.

Scanning electron microscope (SEM). SEM images were taken by using high-resolution scanning electron microscope ZEISS Merlin. X-ray diffraction (XRD). XRD patterns were recorded by X-ray diffractometer (Bruker D8) with Cu kα radiation. Contact angle measurements using DI water as solvent were performed with a drop shape analyzer DSA-30S (Kruss).

S3.1.2   Synthesis of Fluorous Cations and Preparation of 2D HPs

We designed a series of primary ammonium iodides sharing a common three-block, perfluoroalkyl tail-alkylene linker-NH3+I-, structure. Within this basic arrangement, variations in the nature of the fluorinated tail and linker allows us to obtain cationic moieties of different molecular length, cross sectional area, and rigidity. The fluorous ammonium salts were obtained through straightforward synthetic elaborations of commercially available perfluoroalky- lated building-blocks. The set of fluorous ammonium iodides A4n characterized by the presence of the nonafluoro-tert- butyloxy tail were prepared using a two-step procedure based on rabai's synthesis of branched fluorous amines (Scheme 1).40 In brief, condensation under Mitsunobu conditions of the readily available (N-hydroxyalkyl)amino

phthalimide deriva- tives 1a-c with perfluoro-tert-butanol afforded the correspond- ing perfluoro-tert-butyl ethers 2a-c, from which the A4n salts were released by hydrazinolysis followed by acidic workup in the presence of aqueous hydrogen iodide. The linear alkyl ammonium salt L containing a n-perfluorohexyl unit was likewise prepared by hydrazinolysis of a phthalimide derivative obtained via a different route, also shown in Scheme 1. In this case, the masked amine 5 was obtained by addition of perfluorohexyl iodide to N-allyl phthalimide 3 in the presence of zinc, followed by dehalogenation of intermediate 4 Deprotection of 5 by reaction with hydrazine in refluxing methanol and subsequent treatment with aqueous hydrogen iodide afforded the desired ammonium salt. For the sake of simplicity, hereafter we classify them in two categories: the branched family, consisting of a fluorinated ending group and ammonium moiety separated by an ethylene, propylene or butylene group, named A42, A43, and A44, respectively, and the linear cation, L, consisting of six carbon atoms in the linear fluorous tail and three -CH2 units inserted between the fluorous tail and the NH3+ head (Scheme 1 and Figure 1a). The A42, A43, A44, and L-based PbI4-2D HPs were obtained in the form of thin films and single crystals. For thin films, the precursor solutions were prepared by mixing a 2:1 molar ratio of the corresponding cation and PbI2 in DMSO. Different conditions for the film deposition were examined to improve the film quality, varying composition ratios of the precursors, treatments of the substrates (cleaning treating, hot- casting)41 and antisolvents (chlorobenzene, toluene, trifluor- otoluene).42,43 In our case, the use of an one-step deposition method with chlorobenzene as antisolvent provided the best protocol to obtain smooth thin films, along with annealing at 100 °C for 10 min (see top view morphology from scanning electron microscope images in Supporting Information (SI) Figure S1). On the other hand, single crystals were obtained by heating stoichiometric amounts of the organic cations and lead iodide in hydriodic acid at a concentration of ∼0.1 M at 100 °C for 1 day (see SI for further details). As a result, the newly synthesized cations infiltrate in between the inorganic PbI6 layers, forming a pure 2D HP (n − 1), as shown in Figure 1b for the (A42)2PbI4

S3.1.3 General Procedure for the Mitsunobu Reaction

In a flamedried Schlenk tube equipped with a magnetic stirrer (N- hydroxyalkyl)amino phthalimide 1 (10 mmol) and PPh3 (12 mmol) were suspended in dry Et2O (50 mL) under nitrogen. After cooling at 0 °C, perfluoro-tert-butanol (10 mmol) was added followed by the dropwise addition of a solution of diisopropyl azodicarboxylate (DIAD, 12 mmol) in dry Et2O (8 mL) in 5 min. The mixture was left to attain room temperature and then stirred overnight. The mixture was filtered, the solvent was removed at reduced pressure, and the residue purified by column chromatography.

2-[2-(Nonafluoro-tert-butyloxy)-ethyl]isoindole-1,3-dione (2a). This product was obtained using the standard Mitsunobu procedure starting from 1a(1.91 g, 10 mmol) and perfluoro-tert-butanol (1.4 mL, 10 mmol). Crude material was purified by column chromatography (silica gel, petroleum ether/diethyl ether 4/1) to give the title compound (3.26 g, 79.6% yield) as a white solid. 1H NMR (400 MHz, CDCl$_3$) δ = 7.88 (dd, 3J = 5.4, 3.1, 2H), 7.74 (dd, 3J = 5.5, 3.1, 2H), 4.27 (t, 3J = 5.5, 2H), 4.01 (t, 3J = 5.5, 2H). 13C NMR (100.6 MHz, CDCl$_3$) δ 167.8, 134.2, 131.8, 123.4, 120.1 (q, 1JCF = 293.9), 79.8 (m), 66.6, 37.4. 19F NMR (282 MHz, CDCl$_3$) δ = -71.01 (s). Anal. Calcd for C14H8F9NO3: C 41.09, H 1.97, N 3.42. Found: C 41.05,H 1.96, N 3.40.

2-[3-(Nonafluoro-tert-butyloxy)-propyl]isoindole-1,3-dione (2b). This product was obtained using the standard Mitsunobu procedure starting from 1b(2.05 g, 10 mmol) and perfluoro-tert-butanol (1.4 mL, 10 mmol). Crude material was purified by chromatography (silica gel, petroleum ether/diethyl ether 4/1) to give the title compound (3.50 g 82.8% yield) as a white solid. 1H NMR (400 MHz, CDCl$_3$) δ = 7.84 (dd, 3J = 5.4, 3.0, 2H), 7.71 (dd, 3J = 5.5, 3.0, 2H), 4.11 (t, 3J = 6.0, 2H), 3.81 (t, 3J = 7.0, 2H), 2.10 (quintet, 3J = 6.4, 2H). 13C NMR (100.6 MHz, CDCl$_3$) δ 168.3, 134.1, 132.2, 123.4, 120.3 (q, 1JCF =290.7), 79.7 (m), 67.8, 34.9, 28.9. 19F NMR (282 MHz, CDCl$_3$) δ = -70.82 (s). Anal. Calcd for C15H10F9NO3: C 42.57, H 2.38, N 3.31. Found: C 42.53, H 2.39, N 3.30.

2-[4-(Nonafluoro-tert-butyloxy)-butyl]isoindole-1,3-dione (2c). This product was obtained using the standard Mitsunobu procedure starting from 1c(2.19 g, 10 mmol) and perfluoro-tert-butanol (1.4 mL, 10 mmol). Crude material was purified by chromatography (silica gel, petroleum ether/diethyl ether 4/1) to give the title compound (3.58 g, 81.9% yield) as a white solid. 1H NMR (400 MHz, CDCl$_3$) δ = 7.84 (dd, 3J = 5.4, 3.0, 2H), 7.71 (dd, 3J = 5.4, 3.1, 2H), 4.04 (t, 3J = 5.8, 2H), 3.72 (t, 3J = 6.8, 2H), 1.90-1.61 (m, 4H). 13C NMR (100.6 MHz, CDCl$_3$) δ 168.5, 134.1, 132.2, 123.4, 120.5 (q, 1JCF = 291.8),80.0 (m), 69.2, 37.4, 27.2, 24.8. 19F NMR (377 MHz, CDCl$_3$) δ = -71.35 (s). Anal. Calcd for C16H12F9NO3: C 43.95, H 2.77, N 3.20. Found: C 43.88, H 2.76, N 3.22.

2-(4,4,5,5,6,6,7,7,8,8,9,9,9-Tridecafluorononyl)isoindole-1,3- dione (5). To a solution of iodide 4 (4 g, 6.32 mmol) and Et3N(1 mL, 7.17 mmol) in dry THF (7 mL) in a stainless steel reactor, 10% Pd/C (125 mg) was added. The reactor was pressurized with H2 (4 atm) at room temperature. After 24 h, the pressure was released and the mixture was filtered through a short pad of Celite and concentrated under vacuum. The residue was purified by chromatog- raphy (silica gel, petroleum ether/methylene chloride 7/3) affording the title compound (2.89 g, 90.4% yield) as a white solid. 1H NMR (400 MHz, CDCl$_3$) δ = 7.86 (dd, 3J = 5.4, 3.0, 2H), 7.73 (dd, 3J = 5.4, 3.1, 2H), 3.78 (t, 3J = 6.9, 2H), 2.29-2.07 (m, 2H), 2.07-1.93 (m, 2H). 13C NMR (100.6 MHz, CDCl$_3$) δ 168.3, 134.3, 132.1, 123.5, 121-105 (m, C6F13), 37.2, 28.8 (t, 1JCF = 22.7), 20.1. 19F NMR (377 MHz, CDCl$_3$) δ = -81.77 (t, 3J = 10.1, 3F), -115.24 (m, 2F), -122.94 (m, 2F), -123.89 (m, 2F), -124.38 (m, 2F), -127.14 (m, 2F). Anal. Calcd for C17H10F13NO2: C 40.25, H 1.99, N 2.76. Found: C 40.38, H 1.98, N 2.74.

S3.1.4   General Procedure for the Hydrazinolysis of Phthalimide Derivatives

To a solution of phthalimide derivative (1 mmol) in MeOH (2 mL), hydrazine monohydrate (1.2 mmol, 60 μL) was added and the solution refluxed for 3 h. After cooling, the mixture was filtered through a Buchner funnel to remove the solid phthalhy- drazide. The clear

methanolic solution was treated with 50% aqueous HI (0.18 mL, 1.2 mmol). The solution was stirred overnight at room temperature. The solvent was removed at reduced pressure and the residue was dissolved in the minimal amount of MeOH and precipitated from diethyl ether. After filtration, the solid material was dried under vacuum. 2-(Nonafluoro-tert-butyloxy)ethylamine hydroiodide (A42). Hy- drazinolysis of 2a(3.00 g, 7.33 mmol) afforded the title compound (2.34 g, 78.4% yield) as a white solid. 1H NMR (400 MHz, DMSO) δ = 7.82 (s, 3H), 4.27 (t, 3J = 5.2, 2H), 3.17 (t, 3J = 5.2, 2H). 13C NMR (100.6 MHz, DMSO) δ = 119.8 (q, 1JCF = 293.3), 79.2 (m), 67.0, 38.6. 19F NMR (282 MHz, CDCl$_3$) δ = -70.97 (s). 3-(Nonafluoro-tert-butyloxy)propylamine hydroiodide (A43). Hydrazinolysis of 2b(3.00 g, 7.08 mmol) afforded the title compound (2.28 g, 76.5% yield) as a white solid. 1H NMR (400 MHz, DMSO) δ = 7.56 (s, 3H), 4.18 (t, 3J = 6.2, 2H), 2.96-2.80 (m, 2H), 2.06-1.80 (m, 2H). 13C NMR (100.6 MHz, DMSO) δ = 119.9 (q, 1JCF = 291.8), 79.36 (m), 67.78, 35.53, 27.49. 19F NMR (282 MHz, CDCl$_3$) δ = -70.97 (s). 4-(Nonafluoro-tert-butyloxy)butylamine hydroiodide (A44). Hy- drazinolysis of 3c(2.04 g, 4.67 mmol) afforded the title compound (1.33 g, 65.5% yield) as a white solid. 1H NMR (400 MHz, MeOD) δ = 4.15 (d, 3J = 5.3, 2H), 3.10-2.86 (m, 2H), 1.83-1.72 (m, 4H). 13C NMR (100.6 MHz, MeOD) δ 120.4 (q, 1JCF = 292.9), 81.0 (m), 70.9, 40.4, 27.84, 25.06. 19F NMR (377 MHz, CDCl$_3$) δ = -72.70 (s). 4,4,5,5,6,6,7,7,8,8,9,9,9-Tridecafluorononylamine hydroiodide (L). Hydrazinolysis of 5(1.00 g, 1.97 mmol) afforded the title compound (0.75 g, 65.5% yield) as a white solid. 1H NMR (400 MHz, DMSO) δ = 7.71 (s, 3H), 2.94 (s br, 2H), 2.39 (m, 2H), 1.81 (m, 2H). 13C NMR (100.6 MHz, DMSO) δ 121-107 (m, C6F13), 37.9, 26.9 (t, 1JCF = 21.2), 18.3. 19F NMR (377 MHz, DMSO) δ = -81.22 (t, 3J = 10.0, 3F), -114.56 (m, 2F), -122.73 (m, 2F), -123.67 (m, 2F), -124.19 (m, 2F), -126.78 (m, 2F).
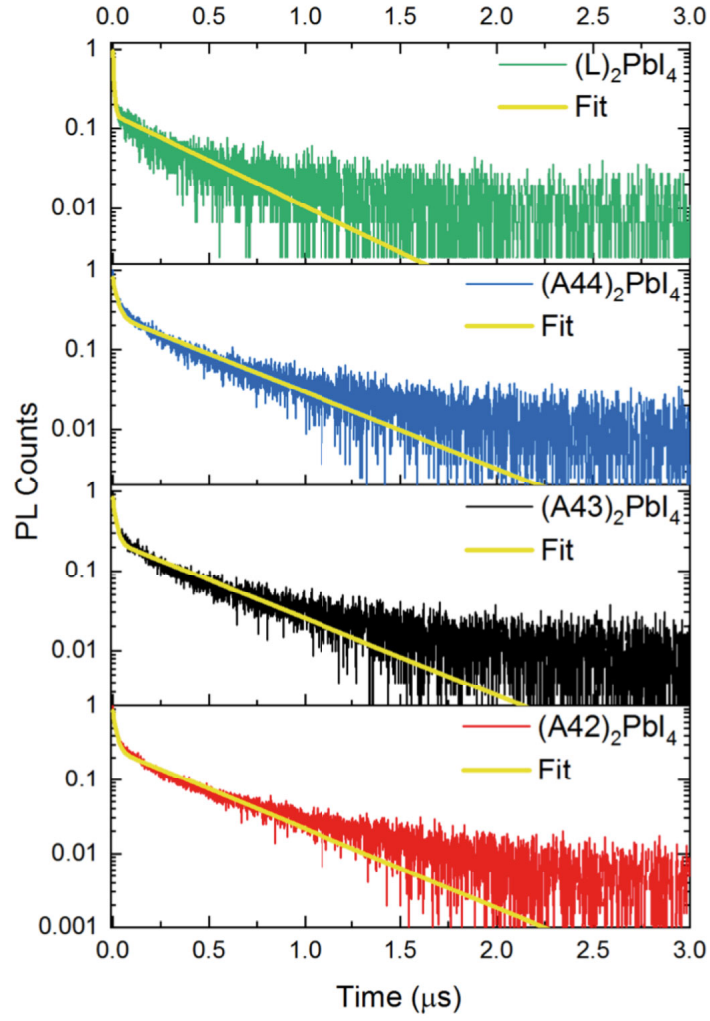
Figure S3.1-1: The PL decay fitted with a bi-exponential function for $(A43)_2PbI_4$, $(A43)_2PbBr_4$ and $(L)_2PbI_4$, $(L)_2PbBr_4$.
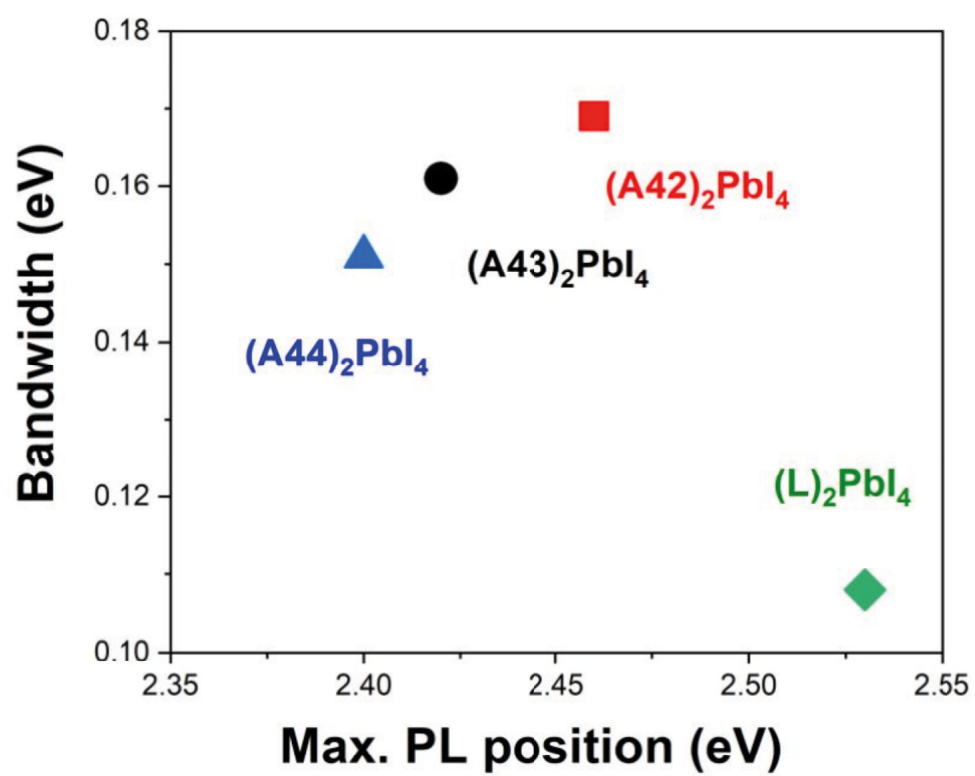
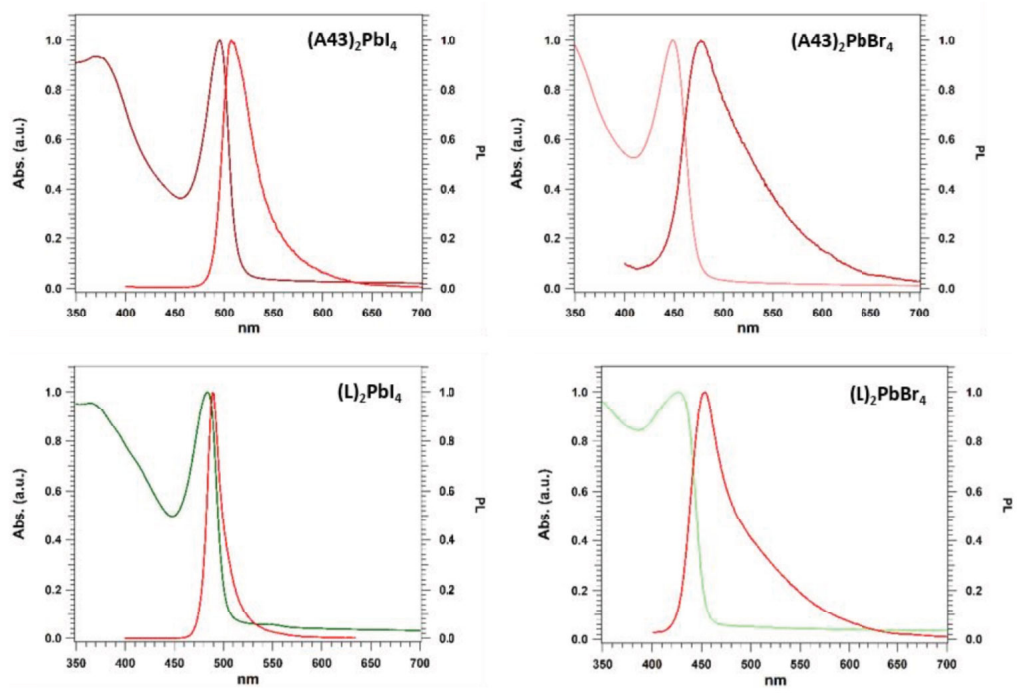Figure S3.1-2: Maximum PL peak position and its corresponding bandwidth for each 2D HP.

Figure S3.1-3: Superposition of PL and absorption spectra for $(A43)_2PbI_4$, $(A43)_2PbBr_4$ and $(L)_2PbI_4$, $(L)_2PbBr_4$.

		$(A42)_2PbI_4$	$(A43)_2PbI_4$	$(A44)_2PbI_4$	$(L)_2PbI_4$
y0	Value	0	0	0	0
y0	Standard Error	0	0	0	0
A1	Value	0.60659	0.58485	0.54296	0.81415
A1	Standard Error	0.00431	0.00596	0.00582	0.00899
τ_1 (µs)	Value	18.43675	17.21476	22.55986	7.30728
τ_1 (µs)	Standard Error	0.2257	0.29525	0.42175	0.12902
A2	Value	0.25796	0.23633	0.26838	0.12607
A2	Standard Error	0.00137	0.00165	0.00198	0.00148
τ_2 (µs)	Value	404.2775	448.9582	453.41048	436.51256
τ_2 (µs)	Standard Error	2.53948	3.8192	3.89328	6.79758
Statistics	Reduced Chi-Sqr	1.08E-04	1.96E-04	2.37E-04	2.16E-04
Statistics	Adj. R-Square	0.97981	0.95754	0.96017	0.89413

Table S3.1-1: Superposition of PL and absorption spectra for $(A43)_2PbI_4$, $(A43)_2PbBr_4$ and $(L)_2PbI_4$, $(L)_2PbBr_4$.

	Excitonic peak (eV)	Band Gap (eV)	Max. PL (eV)	Excitonic binding energy (meV)
A42	2.53	2.9	2.46	380
A43	2.51	2.9	2.42	393
A44	2.49	2.9	2.40	420
L	2.57	2.7	2.53	130

Table S3.1-2: Superposition of PL and absorption spectra for $(A43)_2PbI_4$, $(A43)_2PbBr_4$ and $(L)_2PbI_4$, $(L)_2PbBr_4$.

S3.2   Spatial Charge Separation as the Origin of Anomalous Stark Effect in Fluorous Two-Dimensional Hybrid Perovskites

Methods

Sample preparation

To fabricate $(Fluo)_2PbI_4$ thin films, the precursor solution was prepared by mixing a 2:1 molar ratio of the corresponding ammonium salt ((CF3)3CO(CH2)3NH3I), synthesized as previously reported,[48] and PbI_2 in DMSO. We used the one-step deposition method using chlorobenzene as antisolvent. The thin film was annealed at 100°C for 15 minutes. This results in a 300nm thick film.

Characterization

Steady-state absorption spectra were acquired with a Perkins Elmer Lambda 950s UV/Vis spectrophotometer using an integrating sphere to account for optical losses outside of the active layer. Steady state and time resolved photoluminescence measurements were carried out on a Horiba a Fluorolog-3, with a PMT as detector. The excitation source for the TCSPC is a Horiba nanoLED-370 with an excitation wavelength of 369nm, a pulse duration of 1.3ns and a repetition rate of 100 MHz. Low temperature PL and absorption were performed in their respective instruments fitted with a OptistatND from Oxford Instruments.

X-Ray diffraction

XRD patterns were recorded by X-ray diffractometer (Bruker D8) with Cu $k\alpha$ radiation.

Nanosecond transient absorption

Nanosecond transient absorption measurements were carried out with a LP980 laser flash spectrometer (Edinburgh Instruments). It is based on a standard Transient Absorption setup where the sample is excited by a ns laser pulse and the time evolution of the differential absorption changes induced by the pump is monitored by a CW light source probe. The pump pulses are provided by a nanosecond tunable Ekspla NT340 laser (5 Hz repetition rate) The excitation wavelength was set at 420nm and the excitation density was tuned from 4 $\mu J/cm^2$ to 40 $\mu J/cm^2$ but negligible effects on the dynamics were observed on these time scales. The probe light is provided by a pulsed Xenon arc lamp. The sample was kept at a 45°angle to the excitation beam. The beams are focused onto the sample ensuring spatial overlap. The transmitted probe is spectrally filtered by a monochromator and detected. The detection systems is based on a set of photomultipliers (with both VIS and near-IR detection window) enabling one to collect the single-wavelength kinetic with higher sensitivity. The signal is finally recorded by a TDS 3032C digital signal analyzer. From the transmission change following photoexcitation the variation in the absorption is thus derived as

where Iprobe is the transmitted probe with excitation off and It is the transmitted probe after laser excitation. The system has a sensitivity of $5 \cdot 10^{-4}$ V and a temporal resolution of 5ns.

Electro-absorption

Electroabsorption spectroscopy measurements consist of detecting a probing light beam after its interaction with a sample subjected to an externally applied electric field done at room Temperature. In the present case, EAS measurements were performed on a common Ti:Sapphire amplified femtosecond laser system by Clark-MXR (CPA-2001), yielding 780-nm pulses at a repetition rate of 1 kHz. The probe beam was obtained by passing the 780-nm laser output through a sapphire plate yielding a white light continuum detected

over the 400-850 nm region. After being transmitted through the sample (transmittance mode, semi-transparent gold electrode) or being reflected off of its gold electrode (reflectance mode), the probe beam was dispersed in a grating spectrograph (SpectraPro 2500i, Princeton Instruments or SR163, Andor Technology) and finally detected shot by shot at a 1 kHz rate with a 512 x 58 pixel back-thinned CCD detector (S07030- 0906, Hamamatsu). Part of the probe beam was split before the sample into a reference beam reaching a second detector, which allowed for corrections for shot-to-shot fluctuations. The externally applied voltage was controlled by a function generator (AFG 2021, Tektronix), yielding square voltage pulses (100-μs pulse duration). The voltage pulses were modulated at 500 Hz, allowing to get the desired differential signal $\Delta A = A_{field} - A_{nofield}$. Multiple samples were measured under the same conditions, yielding consistent results.

Computation

Both the frozen glass annealing simulation (consisting in Born-Oppenheimer molecular dynamic simulations and subsequent structural relaxations at 0 K temperature) and the electronic structure calculations on slabs models have been performed using periodic Density Functional Theory (DFT) calculations, within the planewave/pseudopotential formalism, as implemented in the Quantum Espresso Suite.[106] All calculations are performed using a cutoff of 25 Ry and 200 Ry, for the expansion of the wavefunction and of the electron density, respectively, along with ultrasoft pseudopotentials[183] and PBE potential[184] for the description of the exchange-correlation energy. DFT-D2 scheme is used,[185] to improve the description of the van der Waals interactions between the organic molecular spacers.

Born-Oppenheimer Molecular Dynamics (BOMD) simulations and structural relaxations are performed on 2x2x1 supercells of the structural models of $(BUA)_2PbI_4$ and $(Fluo)_2PbI_4$ available from Refs[107] and,[70] respectively. BOMD simulations are performed using a time step of 20 a.u. (1 fs) at 600 K temperature for both $(BUA)_2PbI_4$ and $(Fluo)_2PbI_4$, so to widely explore the potential energy surface of the materials. To fur-

ther speed up the sampling of the potential energy surface, we decreased the effective masses to 10 a.u., for the inorganic atoms, 5 a.u for C, O, N, F and 2 a.u. for H. Notice that this is a common protocol in meta-dynamic simulations and does not affect the quality of the potential energy surface, since it does not influence the interatomic forces.[113] In light of the large size of the structural models employed (624 and 472 atoms respectively for $(BUA)_2PbI_4$ and $(Fluo)_2PbI_4$) the electronic structure is evaluated only at the Γ point of the reciprocal space. Slab calculations are carried out isolating one slab from the crystalline cells of $(BUA)_2PbI_4$ and $(Fluo)_2PbI_4$ providing 15 Åbetween the slab in the periodic cell and its periodic replica. For these calculations, we added the dipole correction, in light of the structural asymmetry introduced during the pull-out computational experiment. For these calculations, the reciprocal lattice is sampled using an automatic 4x4x1 grid,[186] with the less dense sampling associated to the direction of the plane stacking.
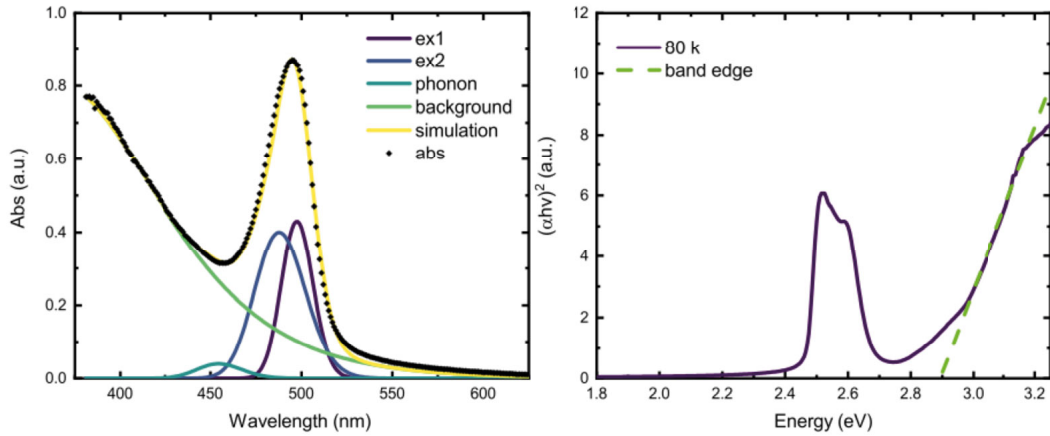

Figure S3.2-1: Fit of the absorption of $(Fluo)_2PbI_4$ at room temperature with 5 gaussians (left). Tauc plot of $(Fluo)_2PbI_4$ at 80K(right)
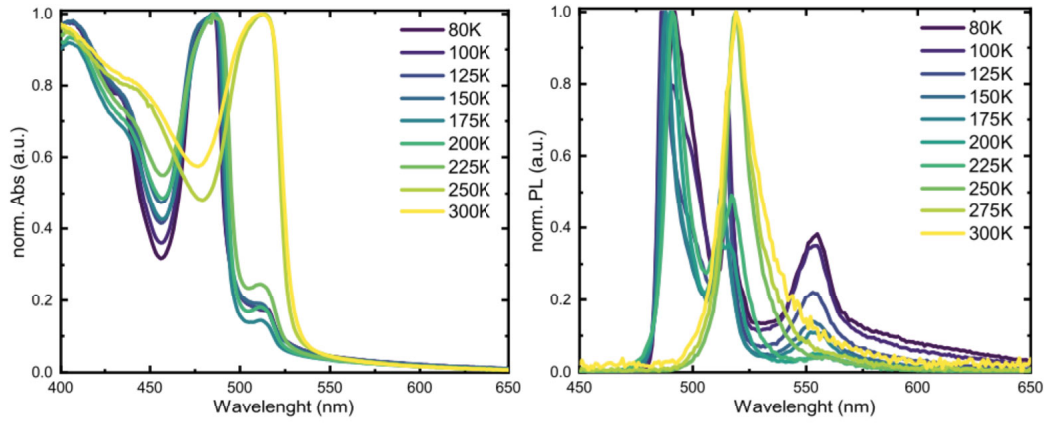
Figure S3.2-2: Normalized absorption vs temperature of $(BUA)_2PbI_4$ (left).PL vs temperature of $(BUA)_2PbI_4$ (right). Both in the absorption and PL spectra we can clearly see some discontinuities between two temperatures. This is the signature of phase transitions.
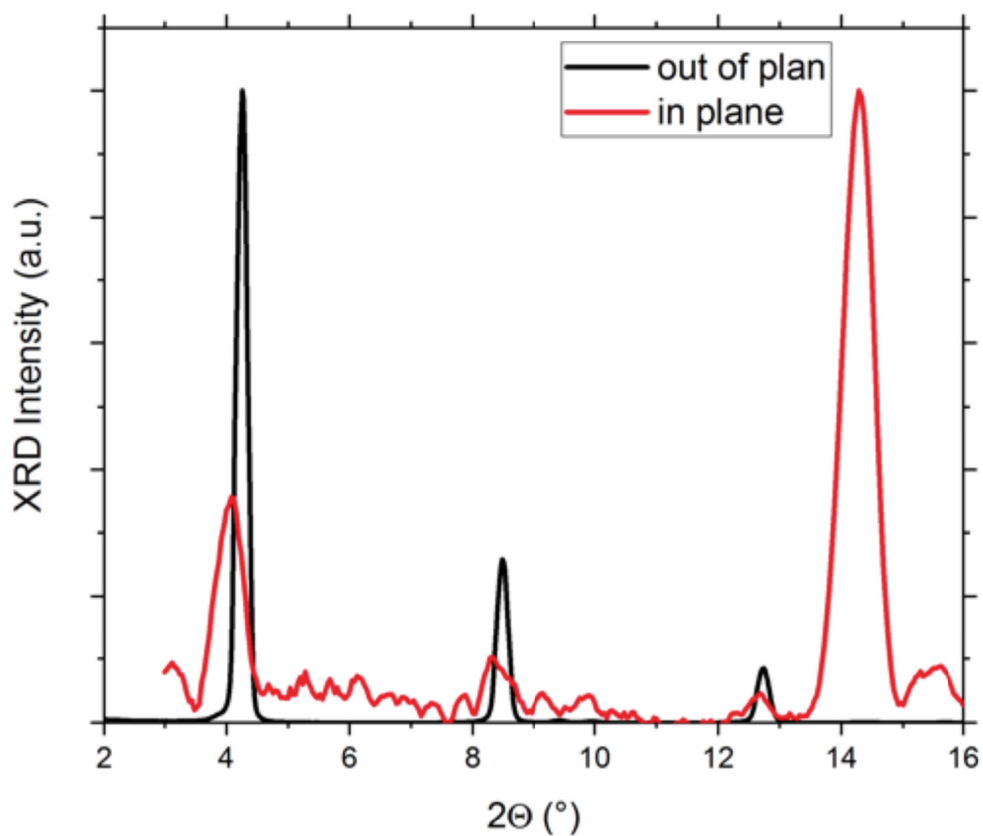
Figure S3.2-3: XRD of $(Fluo)_2PbI_4$ thin film showing two shape peaks at $2\theta = 4$ and 8.5. These two peaks are characteristic of 2D layered perovskites. More over the intensity of the out of plane peaks compare to the in plane ones suggest that the inorganic planes have a strong preferred orientation parallel to the substrate surface
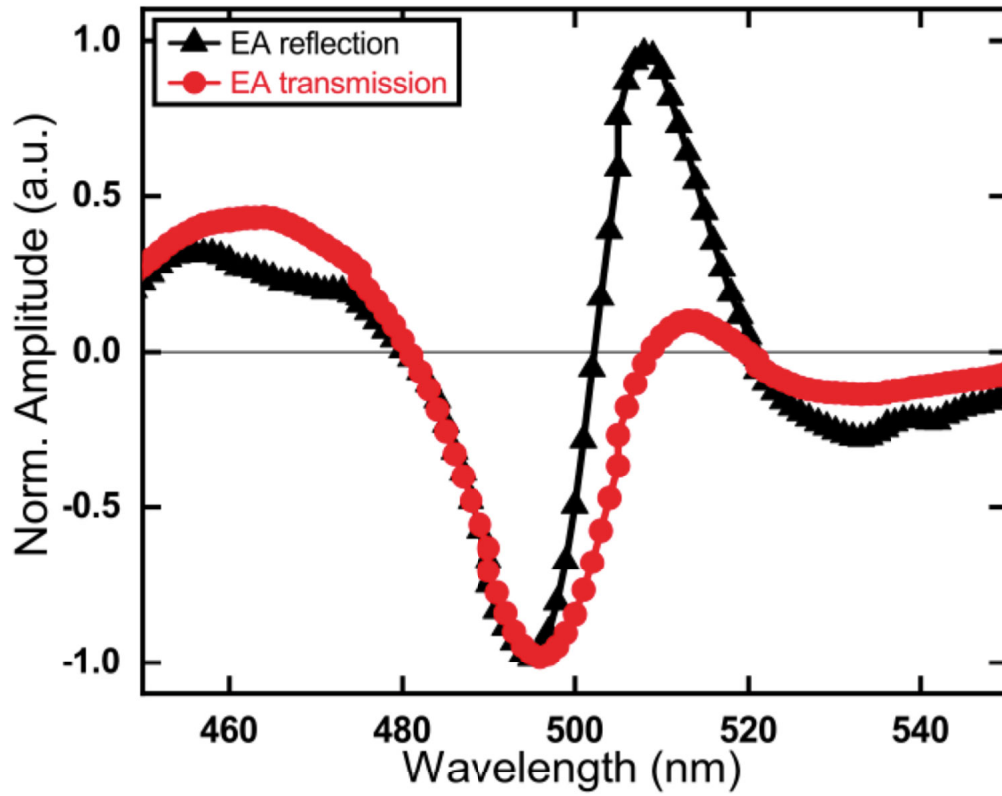
EA contribution to the signal

Figure S3.2-4: EA in reflection and transmission mode at 10V.

From perturbation theory, one can define the EA signal as (perturbative expansion in the field):

$$\Delta A = -\frac{\partial a}{\partial \epsilon} m_{0k} E - \frac{1}{2} \frac{\partial a}{\partial \epsilon} p_{0k} E^2 - \frac{\partial^2 a}{\partial \epsilon^2} (m_{0k} E)^2 + ... \qquad (S3.2-1)$$

Where A denotes the absorbance, E describes the applied electric field and m_{0k} and p_{0k} respectively correspond to the permanent dipole moment and polarizability changes upon the transition of interest (0 à k). Note that the first term (linear in the field) is expected to cancel out for isotropic samples.

EAS Measurements in Reflectance vs Transmittance EAS measurement have be done in both transmission and reflection mode(see Figure S3.2-4). The spectral difference come

from the gold electrode. In this case the reflection spectra can be considered as a double reflection. The transmission spectra amplitude around 515nm is attenuated because the probe beam has to go through the gold which absorb strongly close to this wavelength.

Global Analysis
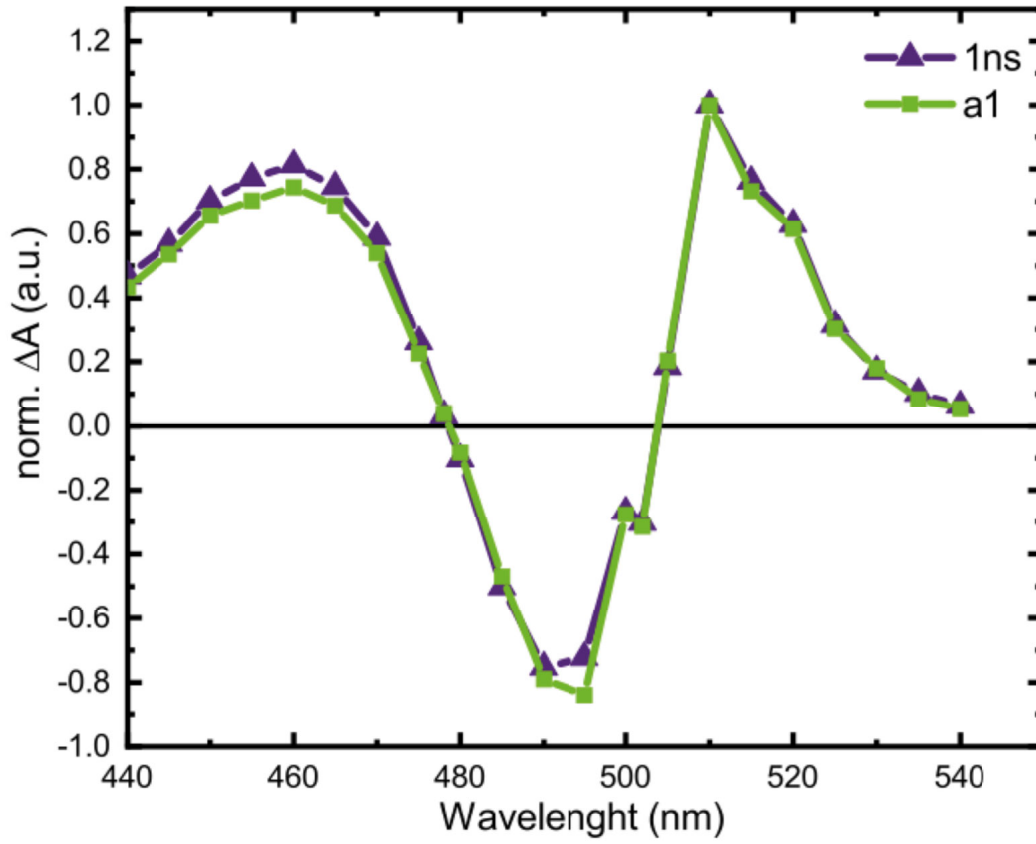
EA contribution to the signal

Figure S3.2-5: Superposition of the TA spectra at 1ns delay with the amplitude of the exponential fit from the global analysis, both normalized.

$$f(x) = a_1 e^{\frac{x}{\tau}} + c \qquad (S3.2\text{-}2)$$

To further analyze the spectral behavior and retrieve the associated time-constant, we

fitted the whole spectral evolution using a Global Analysis (GA) procedure. Representation of the data by the GA The spectral evolution over the whole frequency range can be fitted considering a exponential function with amplitudes represented figure S3.2-5 and time constant τ=932ns and a constant that act as a very long time constant much longer that our time window (Eq. S3.2-2). These observations indicate that the three features have the same dynamic, suggesting that one process is responsible for whole spectral evolution. Remarkably, it is the first time that such a long-lived signal has been reported for 2D HP
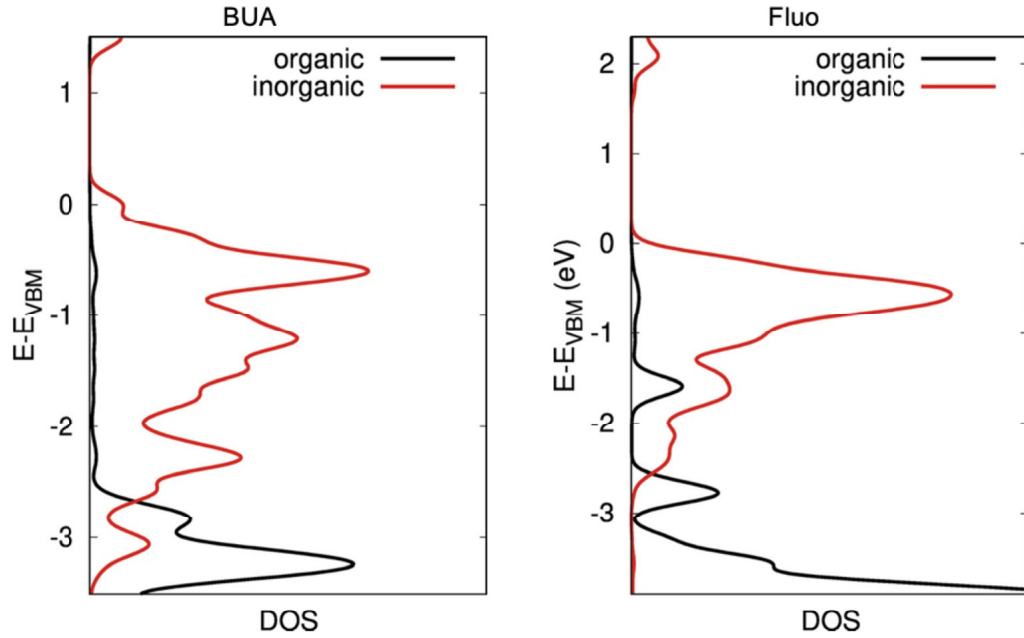
Figure S3.2-6: Partial Density of States (pDOS) from DFT calculations performed on reference 2DP $(BUA)_2PbI_4$ and $(Fluo)_2PbI_4$ materials. Calculations are carried out on the models from XRD experimental measurement. The zero energy corresponds to the valence band edge. The present pDOS distinguish between contributions from the inorganic lattice (red) and organic cation (black). Present calculations include Spin-Orbit Coupling (SOC).

	H	CH3	NH2	NH3+
		PBE		
BUA	0.00	0.00	0.15	8.42
Fluo	2.35	2.25	2.78	20.26
		B3LYP		
BUA	0.00	0.00	0.26	8.87
Fluo	2.53	2.45	2.94	20.02

Table S3.2-1: Molecular dipole associated to the buthylammonium (BUA) and Fluorinated (Fluo) organic spacers. The NH3+ group has been substituted with H, CH_3 and NH_2 (see Figure 3.2-3B of the main text) to preserve the neutrality of the molecule (the dipole is ill-defined for non-neutral systems). For the sake of completeness, also the molecular dipole for molecules containing the group NH_3^+ is reported. Dipoles are computed using Gaussian16,[187] adopting two exchange correlations functionals (PBE and B3LYP) along with 6-311G(d,p) triple zeta split basis set quality.

Experiment	Bands	0th derivative	1st derivative	2nd derivative
EA-simulated	Exciton only	/	0.30	0.17
Absorption	Exciton	/	0.30	0.16
	X	3.53	/	/
EA-real	Abs only	/	0.23	0.30
Absorption	Abs	/	0.24	0.29
	X	2.65	/	/
Nanosecond	Exciton only	/	0.31	0.16
TA x15	Exciton	/	0.33	0.15
	X	9.25	/	/

Table S3.2-2: Fit parameters for the nsTA and EA specra. The parameters correspong to the weight of each derivatives. Value below 10^{-4} were considered no significant and thus were removed(marked with a slash).
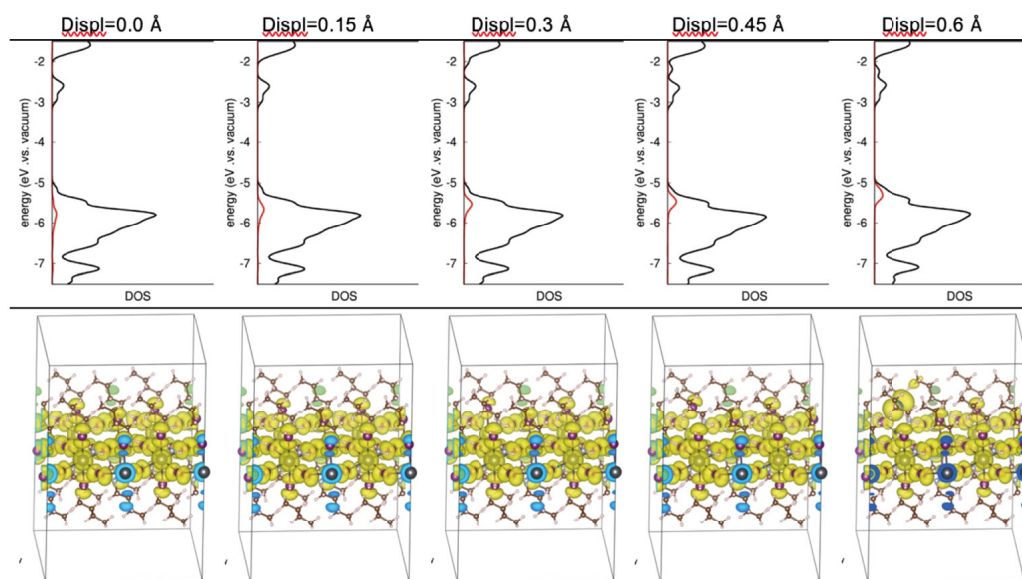
Figure S3.2-7: Result of progressive pull-out of one apical iodine, along with one organic cation, from the equilibrium position, for $(BUA)_2PbI_4$ 2D perovskite. Upper panel: total Density of States of (black line) and DOS associated with the apical Iodine (red line); bottom panel: crystalline orbital isodensity associated the apical iodine involved in the pullout.

Figure S3.2-8: Result of progressive pull-out of one apical iodine, along with one organic cation, from the equilibrium position, for $(Fluo)_2PbI_4$ 2D perovskite. Upper panel: total Density of States of (black line) and DOS associated to the apical Iodine (red line); bottom panel: crystalline orbital isodensity associated the apical iodine involved in the pullout.
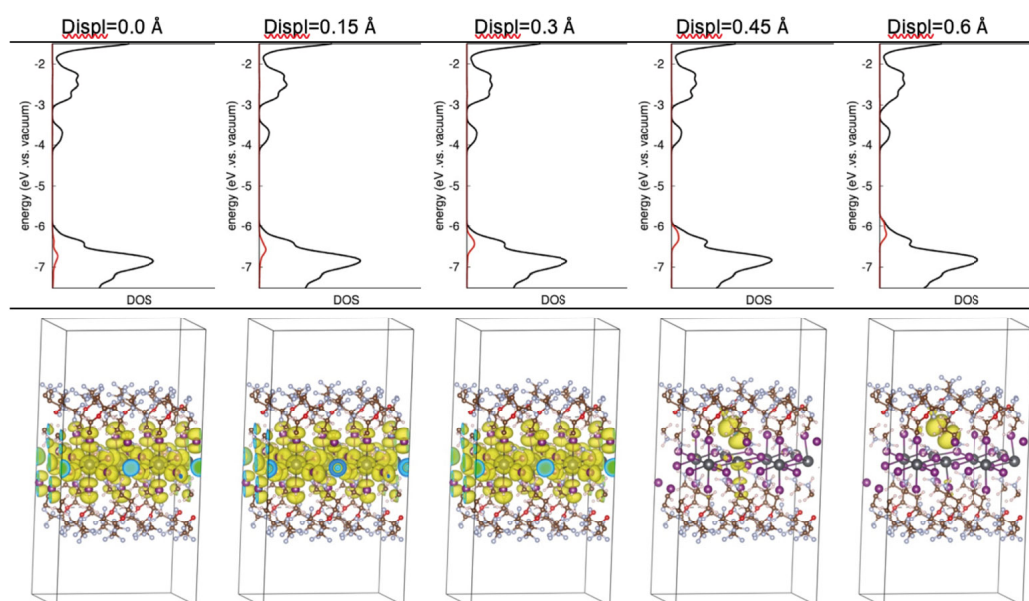
Figure S3.2-9: . Result of progressive pull-out of one apical iodine, along with one organic cation, from the equilibrium position, for (Fluo-H)$_2$PbI$_4$ 2D perovskite. The Fluo-H cation has the same structure as the Fluo but with fluorine atoms substituted by hydrogens. Upper panel: total Density of States of (black line) and DOS associated to the apical Iodine (red line); bottom panel: crystalline orbital isodensity associated the apical iodine involved in the pullout.
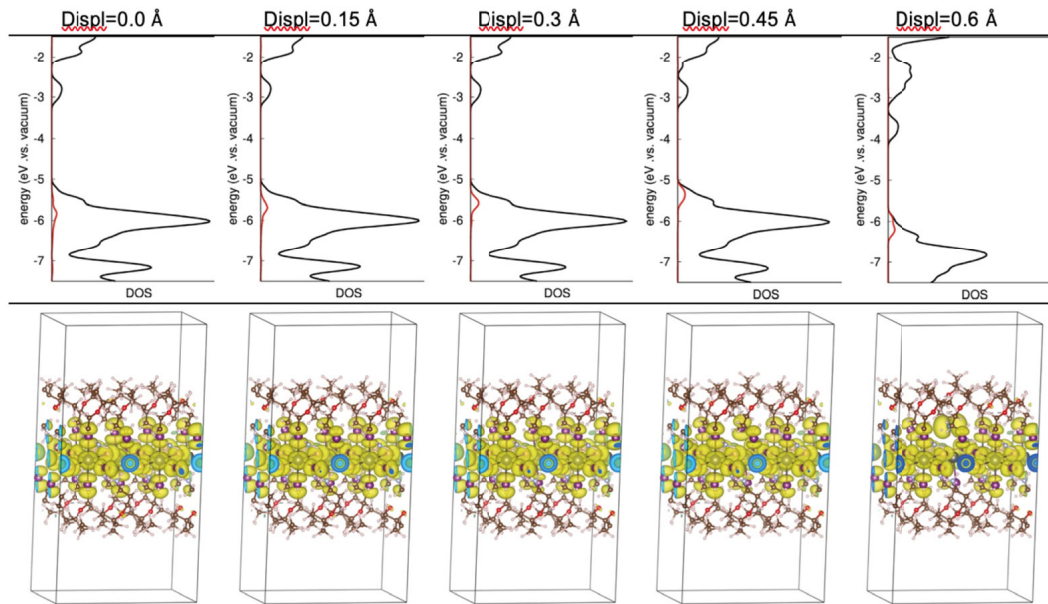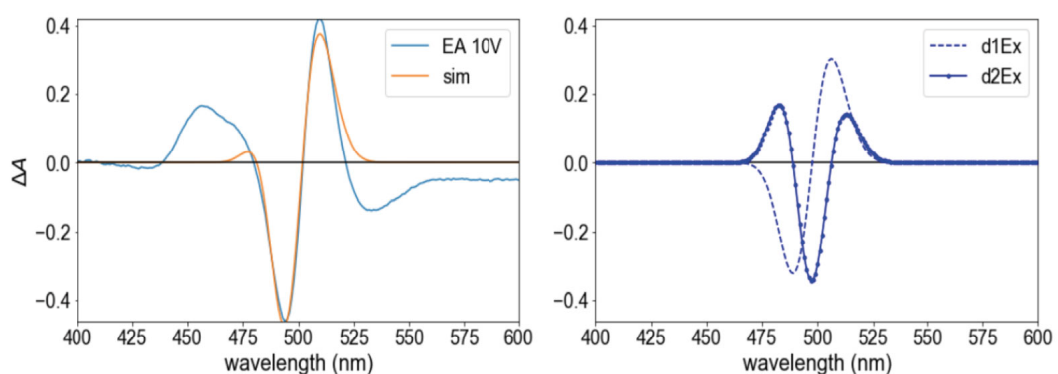

Figure S3.2-10: Simulation of EA without the introduction of the X phonon sideband

Figure S3.2-11: Simulation of the EA spectra using the real absorption (at 300K) 1st and 2nd derivatives and the addition of a X phonon sideband.
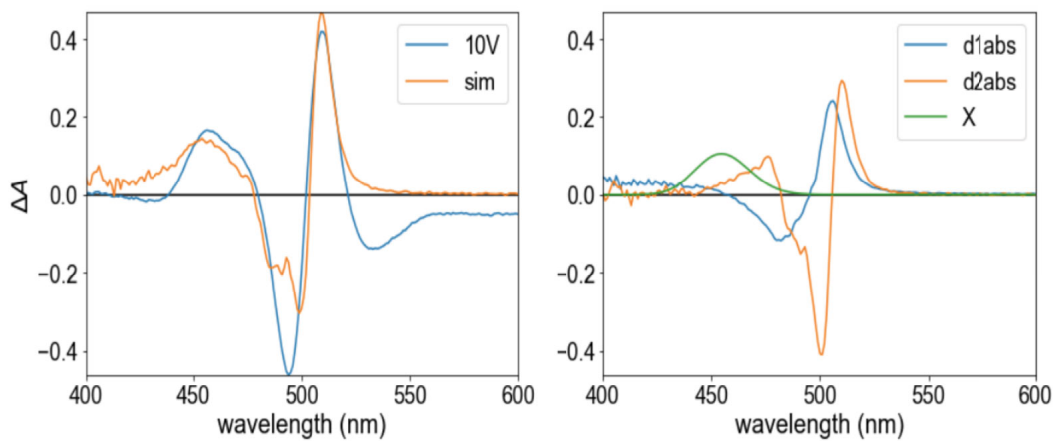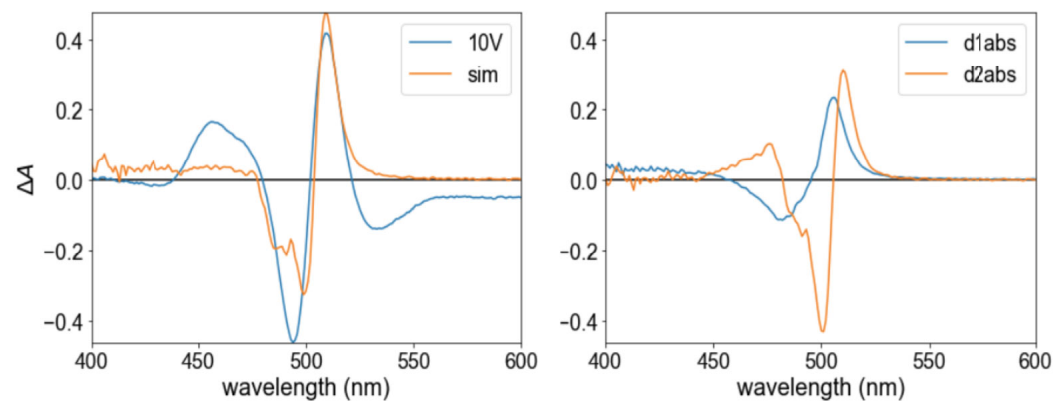

Figure S3.2-12: Simulation of the EA spectra using the real absorption (at 300K) 1st and 2nd derivatives without the addition of a phonon sideband.
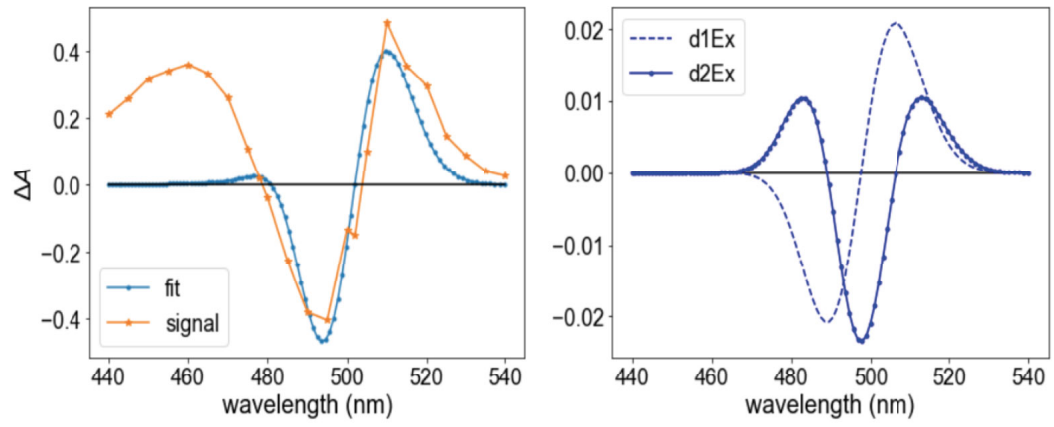
Figure S3.2-13: Simulation of the nsTA spectra without the introduction of the phonon sideband

S4.1 Crystal Orientation Drives the Interface Physics at Two/Three-Dimensional Hybrid Perovskites

S4.1.1 Material and Methods

Device Fabrication and Testing. Fluorine-doped tin oxide (FTO) glass substrates (Nippon sheet glass) were sequentially cleaned with a detergent solution, deionized water, acetone, and ethanol. A compact TiO_2 layer was coated on the cleaned FTO substrate heated at 450 °C by spray pyrolysis deposition. A precursor solution was prepared by diluting titanium diisopropoxide (Sigma-Aldrich) with isopropanol (0.6 mL; 10 mL). Thereafter, we prepared a bilayer electron transport layer with mesoporous TiO_2 and SnO2. Mesoporous TiO_2 films were prepared using a diluted TiO_2 paste (Dyesol 30 NR-D) solution. Films were prepared by spin-coating and sintered on a hot plate at 500 °C for 30 min. The SnO2 layer was prepared by spin-coating a precursor solution of $SnCl_4$ (Acros) dissolved in water. A 0.1 M $SnCl_4$ aqueous solution was spin-coated and sintered on a hot plate at 180 °C for 1 h. The lead excess (FAPbI3)0.85(MAPbBr3)0.15 precursor solution was prepared by mixing FAI (1.1 M), PbI_2 (1.15 M), MABr (0.2 M), and $PbBr_2$ (0.2 M) in a mixed solvent of DMF:DMSO = 4:1 (volume ratio). Another solution of CsPbI3 was also prepared as 1.15 M solution in DMF:DMSO (same volume ratio). For the triple cations mixed perovskite solution, $(FAPbI_3)0.85(MAPbBr_3)$ 0.15 and CsPbI3 solutions were mixed at a 10:1 vol % ratio. The perovskite precursor solution was spin coated at 33 x 2π rad s^{-1} (2000 rpm) for 10 s followed by 83 x 2π rad s^{-1} (5000 rpm) for 30 s. Trifluorotoluene (110 μL) was dropped on the spinning substrate at the 10 s point during the second step. The films were annealed at 100 °C for 60 min in a glovebox. For forming an additional 2D perovskite film on top of this perovskite film, substrates were treated with a PEAI (or FPEAI) isopropanol solution. A 100 mL sample of PEAI (or FPEAI) solution (10 mg/mL) was spin-coated on the 3D perovskite films at 83 x 2π rad s^{-1} (5000 rpm), which is similar to the antisolvent dropping method. The films

were annealed once more at 100 °C for 10 min to make a 2D perovskite layer on the 3D perovskite film. Spiro-OMeTAD was spin-coated at 67 x 2π rad s^{-1} (4000 rpm) for 20 s. A 70 mM spiro-OMeTAD solution was prepared by dissolving in chlorobenzene with 4-tert-butylpyridine, Li-TFSI in acetonitrile, and Co[t-BuPyPz]3[TFSI]3 (FK209) in acetonitrile at a molar ratio of Spiro:FK209:Li-TFSI:TBP of 1:0.03:0.5:3.3. Finally, 70 nm of Au was deposited by thermal evaporation as the back electrode.

The solar cell measurement was done using commercial solar simulators (Oriel, 450 W, Xenon, AAA class). The light intensity was calibrated with a Si reference cell equipped with an IR-cutoff filter (KG3, Newport) and it was recorded before each measurement. Current-voltage characteristics of the cells were obtained by applying an external voltage bias while measuring the current response with a digital source meter (Keithley 2400/2604). The voltage scan rate was 50 mV·s^{-1}, and no device preconditioning such as light soaking or forward voltage bias was applied before starting the measurement. The cells were masked with the active area of 0.16 cm2 to fix the active area and reduce the influence of the scattered light.

Transient Absorption measurements. Ultrafast transient absorbance (TA) spectra were acquired using femtosecond pump-probe spectroscopy with two different pump wavelengths: λ_{ex} = 390 nm and λ_{ex} = 600 nm. The 390 nm pump beam was obtained by frequency doubling the output of a chirped pulse amplified (CPA) Ti:sapphire laser (CPA-2001, Clark-MXR, 778 nm fundamental central wavelength, 120 fs pulse duration, 1 kHz repetition rate) in a BBO crystal, yielding 200 fs pulses. In turn, the 600 nm excitation beam was generated by directing the CPA output into a noncollinear parametric amplifier (NOPA) and then compressed by a pair of SF6 prisms, yielding 100 fs pulses. The probe beam was generated by directing a portion of the CPA fundamental output into a CaF_2 crystal, yielding a white light continuum measured over a (400-780) nm spectral domain. The probe fluence at the sample was much lower than that of the pump (39 μJ cm^{-2}). Similarly, the diameter of the probe beam was smaller to ensure

homogeneous excitation of the probed area. The dynamics of the photoinduced signals were obtained with a computer-controlled delay-line on the pump path. The probe beam was split before the sample into a beam going through the sample (signal beam) and a reference beam. Both signal and reference beams were directed to respective spectrographs (Princeton Instruments, Spectra Pro 2150i) and detected pulse-to-pulse with 512 x 58 pixel back-thinned charge-coupled-device cameras (Hamamatsu S07030-0906). The pump beam was chopped at half of the laser frequency (500 Hz), and a satisfying signal-to-noise ratio was obtained by typically averaging 3000 spectra. The time resolution of the experiment was 250 fs.

Steady-State Optical Measurement. Steady-state absorption spectra were acquired with a Perkins Elmer lambda 950s ultraviolet/Vis spectrophotometer using an integrating sphere to account for optical losses outside of the active layer. Steady-state and time-resolved photoluminescence measurement were carried out on a Horiba Fluorolog-3 instrument, with a photomultiplier tube as detector. The excitation source for the TCSPC was a Horiba nanoLED-370 with an excitation wavelength of 369 nm, a pulse duration of 1.3 ns, and a repetition rate of 1 MHz.

Time-Resolved Photoluminescence Measurements. For TRPC measurements the samples have been loaded into airtight resonant cavity (low intensity measurements) and open cell (high intensities) holders in a N2 filled glovebox. The traces have been measured upon pulsed (10 Hz, 3 ns full-width at half-maximum) photoexcitation at 650 nm from a Q-switched Nd:YAG laser ("Infinity 15-30", Coherent).[188] Excitation intensities have been varied in the range of 109-1012 photons/cm^2.

GIWAXS Measurements. GIWAXS measurements were carried out in reflection geometry at beamline 7.3.3 of the Advanced Light Source, Lawrence Berkeley National Laboratory. Samples were measured at a detector distance of 0.249 m using an X-ray wavelength of 1.240 Å, at 0.18°angle of incidence with respect to the substrate plane.

Calibration was performed with a silver behenate standard. Scattering intensity was detected by a PILATUS 2 M detector.(1) Nika software package was used to sector average the 2D GIWAXS images.(2) Data plotting was done in Igor Pro (Wavemetrics, Inc., Lake Oswego, OR, United States).

S4.1.2   Supplementary figures
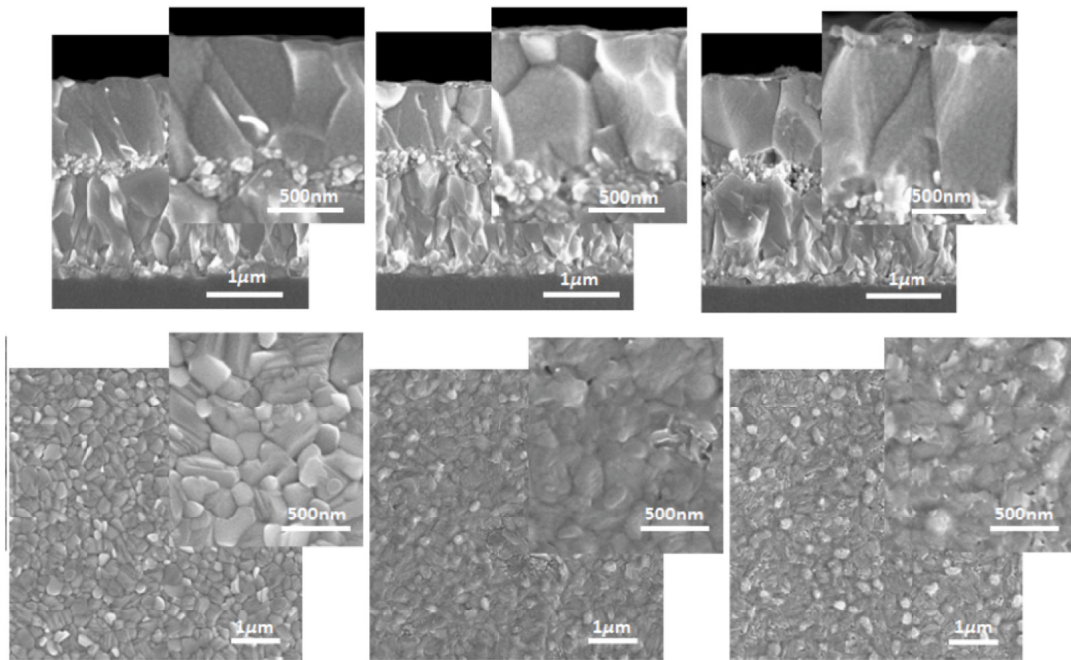
Figure S4.1-1: Top line: cross section SEM for for thin films of Ref3D, pure PEAI-2D, and FPEAI-2D. Bottom line: top view SEM image for the same samples.

390 nm excitation	τ(ps) PEA-2D/3D	τ(ps) FPEA-2D/3D	τ(ps) REF 3D
497 nm GSB	16 ± 5	17 ± 4	-
755 nm GSB	6 ± 1	6± 1	long

Table S4.1-1: Time constant of the monoexponential fits between 1.5 and 100 ps of the dynamics in Figure 4.1-2 d,e. Error bars are one standard deviation based on fit statistic
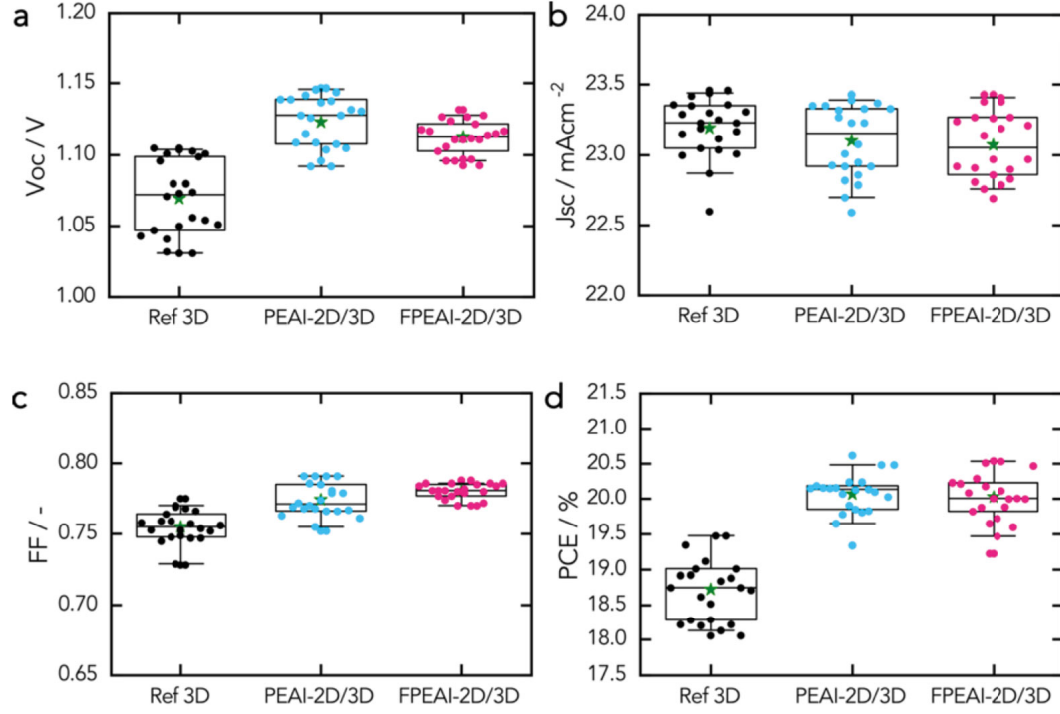
Figure S4.1-2: Device statistic (tukey boxplot) for the PEAI and FPEAI bilayer and the reference over 25 devices of each.

635 nm excitation	A1	t1 (ns)	A2	t2 (ns)
PEA-2D/3D	0.387±0.004	244±4	0.450±0.004	1401±10
FPEA-2D/3D	0.22±0.01	38±2	0.49±0.01	129±1
Ref-3D	0.052±0.02	96±1	0.22±0.02	40±2

Table S4.1-2: Biexponential fits parameters of the of the PL decay shown in Figure 4.1-3a. . Error bars are one standard deviation based on fit statistic
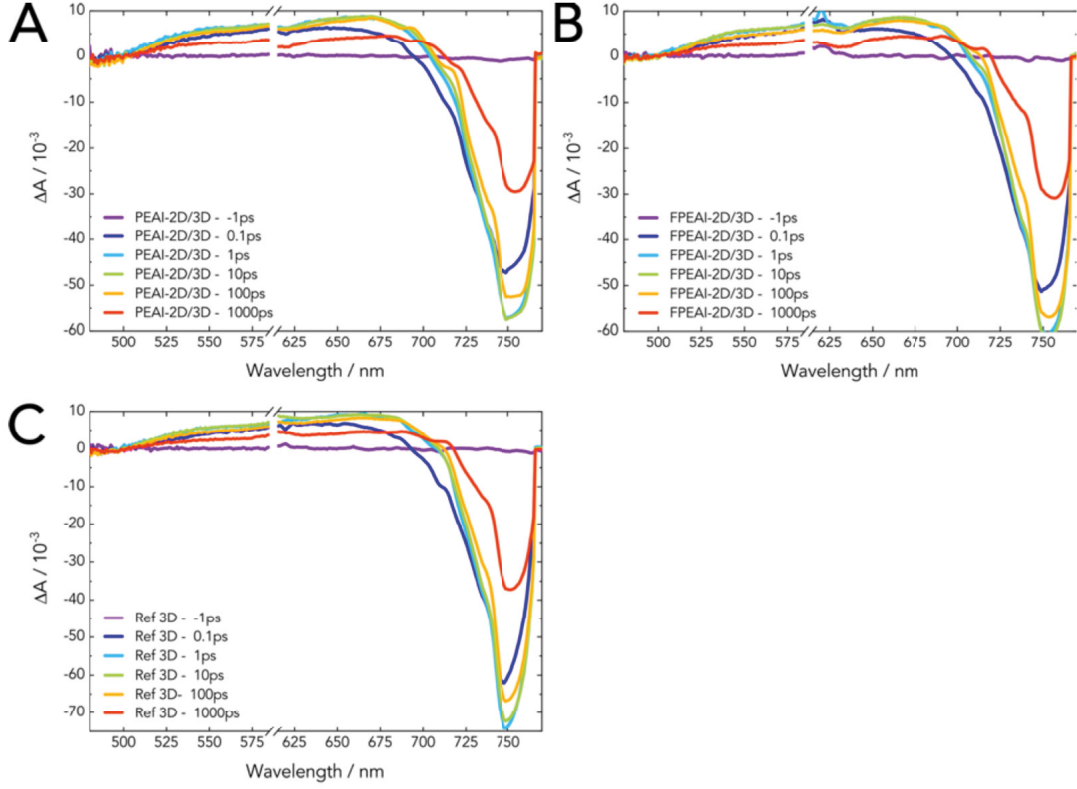
Figure S4.1-3: Femtosecond transient absorption spectra of (A) PEA-2D/3D, (B) FPEA-2D/3D, and (C) Ref-3D, excited at 600 nm generating a carrier density of 10^{18} cm^{-3} at selected time delays

635 nm excitation	A1	t1 (ns)	A2	t2 (ns)
HTM/PEA-2D/3D	0.5±0.01	97±1	0.2±0.01	675±6
HTM/FPEA-2D/3D	0.4±0.01	97±2	0.47±0.01	321±1

Table S4.1-3: Parameters of the biexponential fits of the PL decay shown in Figure 4.1-3c. . Error bars are one standard deviation based on fit statistic
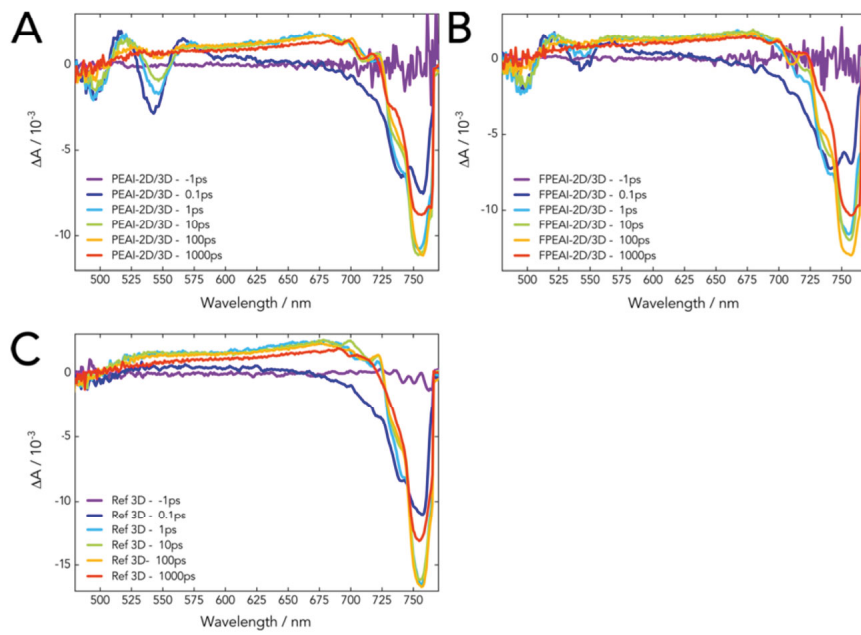
Figure S4.1-4: Femtosecond transient absorption spectra of (A) PEA-2D/3D, (B) FPEA-2D/3D, and (C) Ref-3D excited at 390 nm generating a carrier density of 10^{18} cm^{-3} at selected time delays.
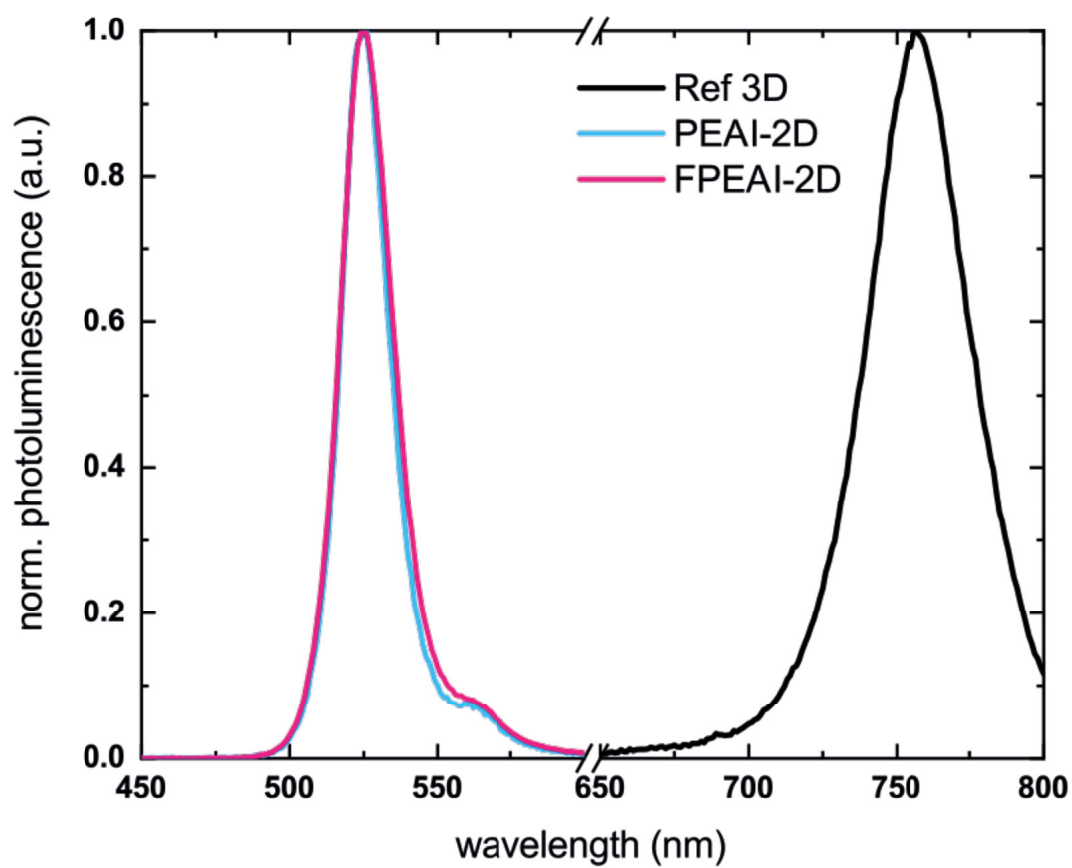
Figure S4.1-5: Photoluminescence spectra of pure 2D PEAI and FPEAI and 3D reference layer excited at 425 nm
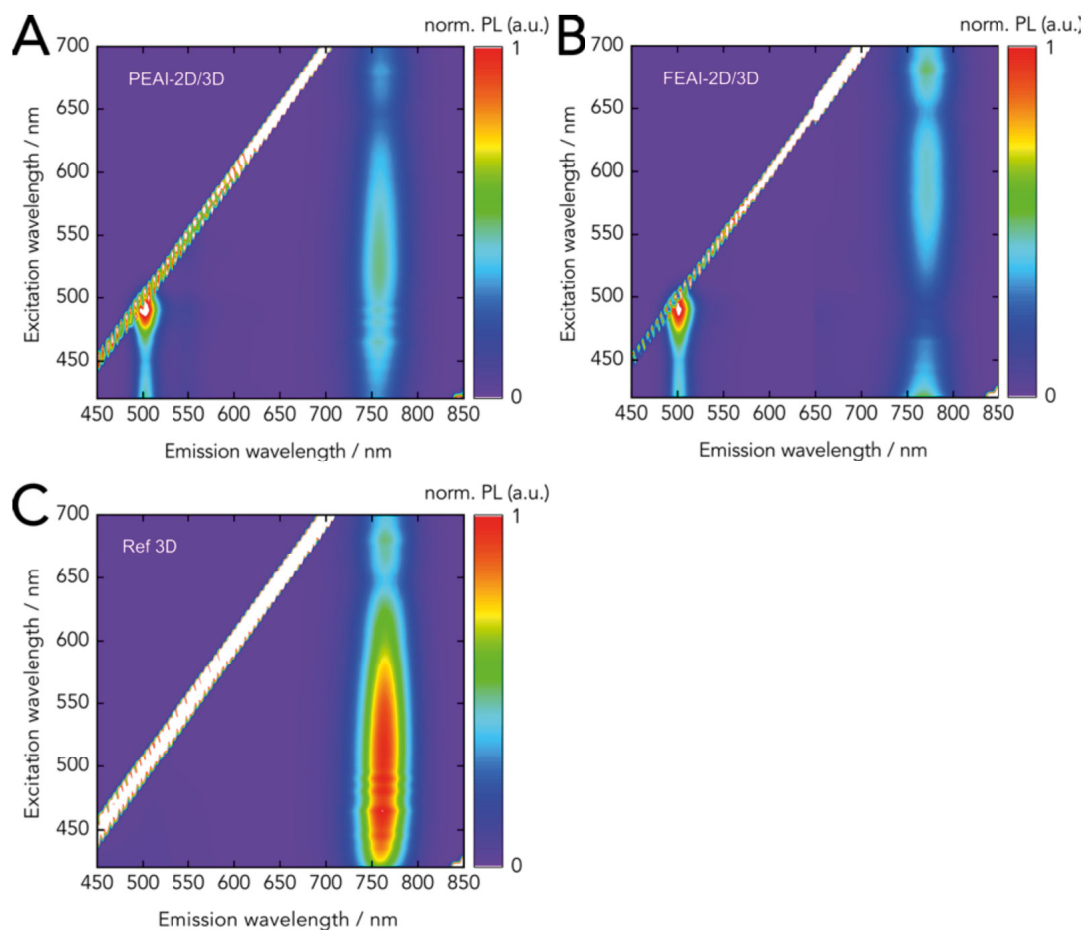
Figure S4.1-6: Photoluminescence excitation map of (A) PEAI-2D/3D, (B) FPEA-2D/3D and (C) 3D Ref. The samples are excited from the 2D layer. The trace at 500 nm correspond to the emission of the 2D layer and the one at 750 nm to the 3D layer underneath
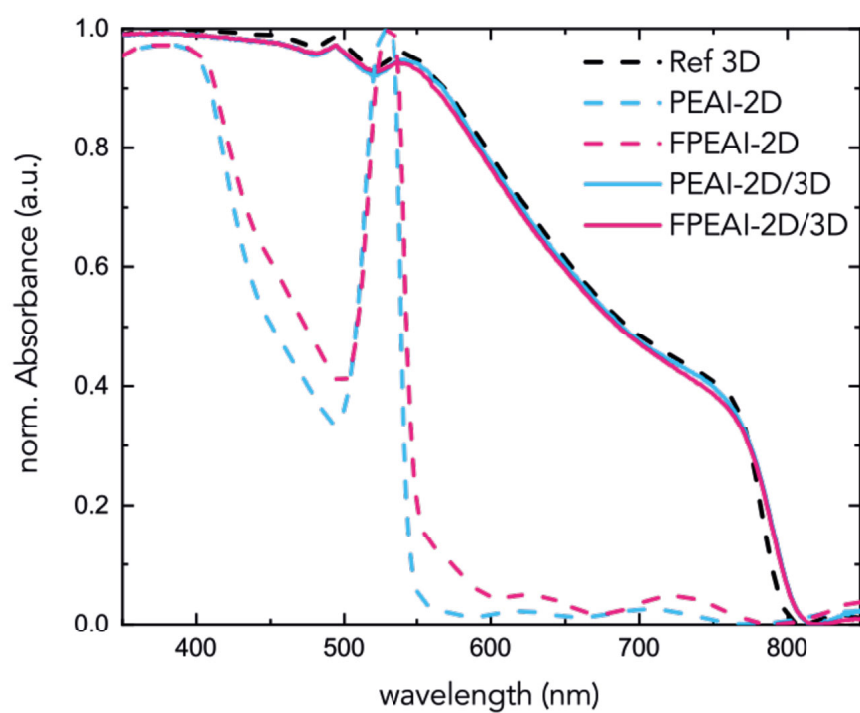
Figure S4.1-7: Absorption spectra of the bilayers(solid), and pure 2D and 3D layers (dashed)
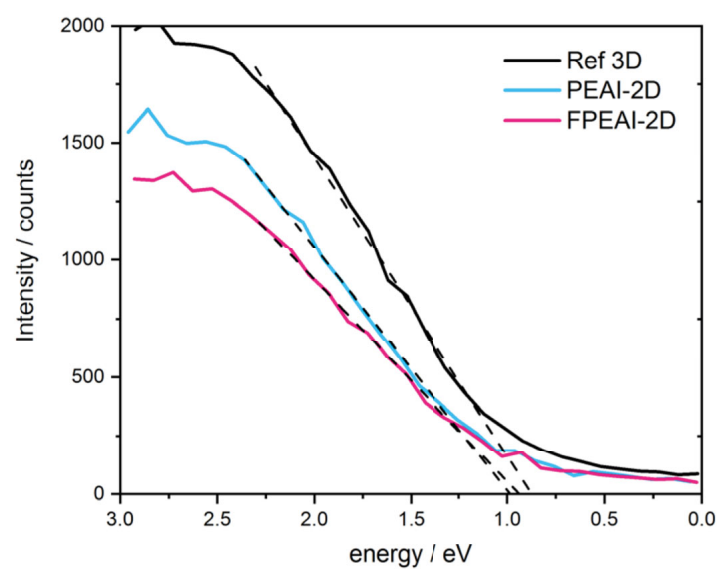
Figure S4.1-8: XPS spectrum zoom around the valence band for thin film of pure PEAI-2D, FPEAI-2D and Ref 3D with linear fit to extract the relative valence band energy.
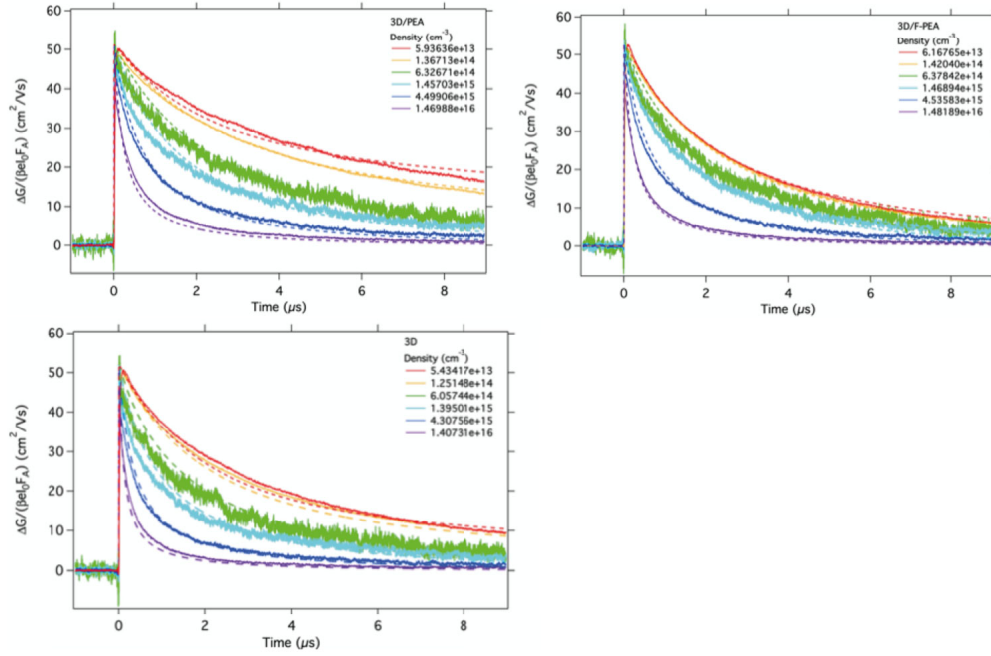
Figure S4.1-9: Intensity dependent TRMC measurements for Ref 3D, PEAI-2D/3D and FPEAI-2D/3D fitted with a kinetic model describes in Figure S4.1-11.
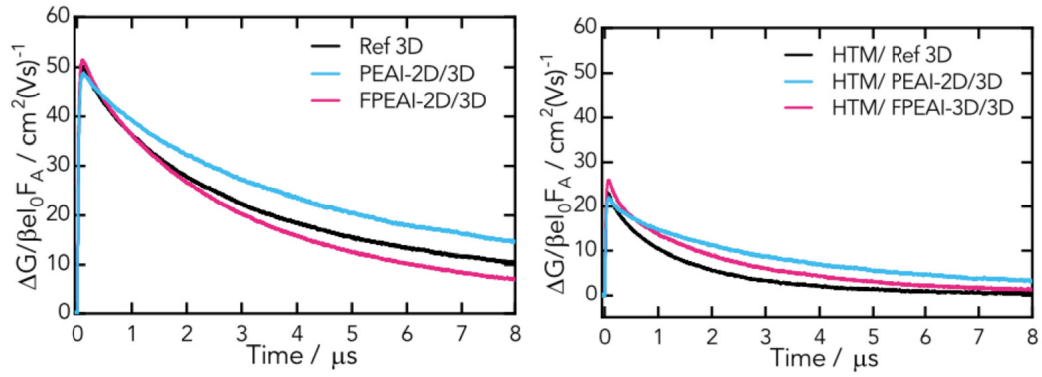
Figure S4.1-10: TRMC data for Ref 3D, PEAI-2D/3D and FPEAI-2D/3D with and without HTM as indicated in the legends, Excitation 600 nm generating a carrier density of 10^{14} cm^{-3}.
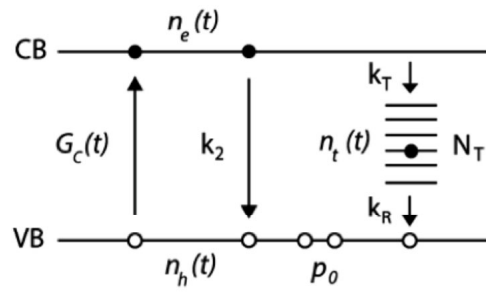
Figure S4.1-11: Schematic representation of the generation (Gc) and recombination processes accounted in the kinetic model described in Hutter et al.[59]

$$\frac{dn_{CB}}{dt} = \frac{dn_e}{dt} = G_c - k_2 n_e(n_h + p_0) - k_T n_e(N_T - n_T) - k_e n_e \qquad \text{(S4.1-3)}$$

$$\frac{dn_{VB}}{dt} = \frac{dn_h}{dt} = -G_c + k_2 n_e(n_h + p_0) + k_D n_t(N_h - p0) - k_h n_h \qquad \text{(S4.1-4)}$$

$$\frac{dn_t}{dt} = k_T n_e(N_T - n_T) - k_D n_t(n_h + p_0) \qquad \text{(S4.1-5)}$$

Parameters	3D	PEAI-2D/3D	FPEAU-2D/3D
kT $(cm^3 s^{-1})$	$2e^{-09}$	$1e^{-09}$	$2e^{-09}$
k2 $(cm^3 s^{-1})$	$6e^{-10}$	$2.8e^{-10}$	$3e^{-10}$
kD $(cm^3 s^{-1})$	$5e^{-10}$	$8e^{-10}$	$1e^{-10}$
NT (cm^{-3})	$2.5e^{+14}$	$5e^{+14}$	$3e^{+14}$
p0 (cm^{-3})	$9e^{+13}$	$5e^{+12}$	$1e^{+14}$

Table S4.1-4: S5 Fitting parameters of the kinetic model on the intensity dependence TRMC measurement for the tree samples.
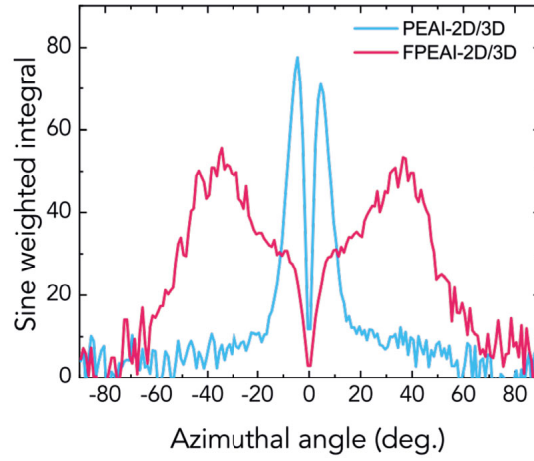
Figure S4.1-12: Sine weighted integral of the n=1 diffraction feature at 0.36 Å^{-1} in Figure 4.1-4 a,b of the bilayers showing a strong preferred orientation for PEAI-2D/3D

S4.2   Dynamical evolution of the 2D/3D interface: A hidden driver behind perovskite solar cell instability

S4.2.1   Methods

Synthesis of thiophene-based cations

A desired concentrated aqueous solution of HI (1.1 eq) was added dropwise to a stirred 1.0 mol/L ethanol solution of the corresponding thiophenealkylamine (1.0 eq) at 0°C. The mixture was allowed to gradually reach room temperature and then it was poured into an excess of diethyl ether (Et2O). The formed precipitate was collected and washed thoroughly with Et2O. The salts were recrystallized from EtOH-Et2O mixtures, providing with crystalline solids (yields $\sim$ 70 %).

Preparation of 2D/3D perovskite films and device fabrication

FTO-coated glass (Nippon sheet glass)1 was chemically etched using zinc powder and HCl solution, followed by cleaning using Hellmanex, water, acetone, and 2-propanol. A 30 nm thick compact TiO2 layer as electron transporting layer was deposited by spray pyrolysis using a titanium diisopropoxide bis(acetylacetonate) solution (Sigma-Aldrich) diluted in 2-propanol (1:15 v/v) at 450 °C. On top of the compact layer, a 100 nm thick mesoporous layer of TiO2 was deposited by spin coating TiO2 paste (GreatCellSolar, 30NR-D) diluted in ethanol (1:8 w/v) at 5000 rpm for 20 s followed by heating at 125 °C for 10 min and sintering at 500 °C for 20 min. A thin layer of passivating tin oxide of $\sim$20 nm was spin-coated by using tin (IV) chloride (Acros) solution (12 μL diluted in 988 μL water) at 3000 rpm for 30 s, followed by annealing at 100 °C for 10 min and 190 °C for 1 h. The prepared substrates were treated with UV-ozone for 15 min before perovskite deposition. A 1.3 mol/L [(FAPbI3)$_{0.87}$(MAPbBr3)$_{0.13}$]$_{0.92}$(CsPbI3)$_{0.08}$

perovskite solution with excess PbI2 (PbI2:FAI = 1.05:1) was prepared by mixing FAI (GreatCellSolar), MABr (GreatCellSolar), CsI (ABCR), PbI2 (TCI), and $PbBr_2$ (TCI) in DMF and DMSO (0.78:0.22 v/v). For the 2D perovskite n=1 (R_2PbI_4, R is the corresponding thiophene alkylammonium cation), the perovskite precursor solution was prepared by dissolving thiophene alkylammonium cation and PbI2 with the molar ratio of 2:1 in mixed solvent of DMF and DMSO (0.78:0.22 v/v). For the quasi 2D perovskite n=2 ($R_2MAPb_2I_7$), the perovskite precursor solution was prepared by dissolving thiophene alkylammonium cation, methylammonium iodide (MAI, GreatCellSolar), and PbI_2 with the molar ratio of 2:1:2 in mixed solvent of DMF and DMSO (0.78:0.22 v/v). The prepared perovskite precursor was then spin-coated on the prepared at 2000 rpm for 12 s and 5000 rpm for 30 s. Chlorobenzene was added as an anti-solvent at 15 s before the end of spin coating process. The films were subsequently annealed at 100 °C for 60 min. After cooling down to room temperature, 0.06 mol/L of thiophene alkyl ammonium iodide cations in 2-propanol was spin-coated dynamically by adding the solution during spinning at 4000 rpm for 30 s, followed by annealing at 100 °C for 6 min. Spiro OMeTAD was used as the hole-transporting materials (HTM). The HTM layer was prepared by dissolving 78.2 mg spiro-OMeTAD (Merck) in 1 mL chlorobenzene doped with 31.28 μL of 4-tert-butylpyridine (Sigma-Aldrich), 18.57 μL of Li- bis (trifluoromethanesulphonyl) imide (Aldrich) from the stock solution (196 mg in 379 μL acetonitrile), 13.69 μL of FK 209 Co(III) TFSI (GreatCellSolar) from the stock solution (99 mg in 263 μL acetonitrile). The doped spiro-OMeTAD solution was then deposited by spin- coating at 4000 rpm for 30 s. Finally, a 70 nm-thick gold counter electrode was thermally evaporated on top of HTM layer.

UV-VIS Absorption

The absorption spectra of the perovskite thin films were recorded with using an ultraviolet, visible, near-infrared spectrophotometer (PerkinElmer Lambda 950S).

Photoluminescence

Photoluminescence spectra of the perovskite thin films were measured and recorded using Fluorolog3-22 spectrofluorometer. The spectra were recorded upon excitation at 450 nm. For the 2D/3D films, the emissions were measured from both front side (2D perovskite side) and back side (3D perovskite side) of the film.

X-ray Diffraction (XRD)

XRD measurements were performed at room temperature with Bruker D8 Advance diffractometer and non-monochromated Cu radiation. For the 2D-3D films, the XRD patterns were obtained using grazing incident diffraction (GID) geometry with Bruker D8 Discover diffractometer and non-monochromated Cu radiation at the incident angle of 2.0 °. In situ X- ray diffraction was performed at 50°C in ambient atmosphere and using a custom-made high- temperature cell (temperature stability +/- 1 K), in Bragg Brentano geometry, with a Bruker D8 Discover diffractometer and non-monochromated Cu radiation. The data acquisition time for the entire pattern between 2 and $16°2\theta$ was approx. 15 minutes, in order to allow for comparison from PL experiments.

Scanning Electron Microscopy (SEM)

Cross-section and top surface SEM images were recorded by in-lens detector of FEI Teneo scanning electron microscope at high tension of 3 kV and 5 kV.

wide angle X-ray Grazing incidence scattering (GIWAXS) measurements

GIWAXS measurements were carried out in reflection geometry at the CMS beamline of the National Synchrotron Light Source II (NSLS II), a U.S. Department of office of the Science User for the DOE Office of Science by were measured at a of 0.153 m using X-ray wavelength of 1.24 A, at 0.16°angle of incidence with respect to the substrate plane. Scattering intensity was detected by a PILATUS 300K detector. Nika2 software package

was used to sector average the 2D Data plotting was done in Igor Pro (Wavemetrics, Inc., Lake Oswego, OR, USA).

Device characterization

The current density–voltage (J–V) curves were measured under 1 sun illumination (AM1.5G) by xenon lamp solar simulator (450 W, Oriel Sol3A, AAA class). The J-V measurements were carried out under ambient condition and room temperature. The light intensity was calibrated to 1 sun by using a Si reference equipped with an IR-cutoff (KG5) filter. An external voltage bias was applied and the current responses were measured at the same time using a digital source meter (Keithley 2400). An active area of 0.16 cm2 was determined by a metal 2 -1 mask with aperture of 0.16 cm . The J-V curves were scanned with the rate of 50 mV s without any preconditioning, such as light soaking or pre-biasing for a long time. For the light intensity dependent measurement, the J-V characteristics were obtained using a VeraSol LED solar simulator (Newport) under various light intensity. External quantum efficiency (EQE) measurement was carried out by using IQE200B (Oriel).

S4.2.2 Supplementary figures
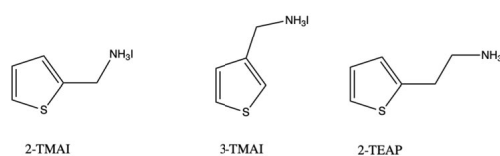
Figure S4.2-1: Molecular structure of 2-TMAI, 3-TMAI and 2-TEAI
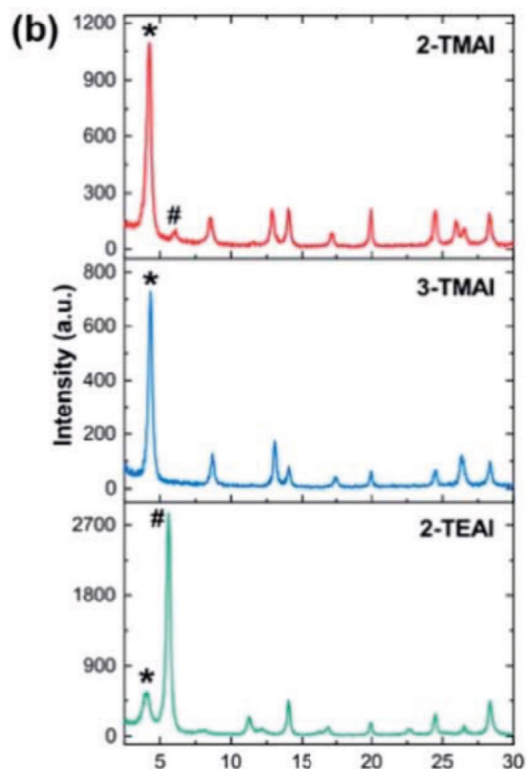
Figure S4.2-2: X-ray diffraction (XRD) pattern at the 2? incident angle of the 2D/3D film employing 2-TMAI, 3-TMAI and 2-TEAI cations in the 2D template. # and denote diffraction peaks of the 2D perovskite with n= 1 and n = 2, respectively.

S4.3 In Situ Analysis Reveals the Role of 2D Perovskite in Preventing Thermal-Induced Degradation in 2D /3D Perovskite Interfaces

S4.3.1 Material and methods

Preparation of 2D/3D perovskite films and device fabrication FTO-coated glass (Nippon sheet glass) was chemically etched using zinc powder and HCl solution, followed by cleaning using Hellmanex, water, acetone, and 2-propanol. A 30 nm thick compact TiO_2 layer as electron transporting layer was deposited by spray pyrolysis us-

ing a titanium diisopropoxide bis(acetylacetonate) solution (Sigma-Aldrich) diluted in 2-propanol (1:15 by volume fraction) at 450 °C. On top of the compact layer, a 100 nm thick mesoporous layer of TiO_2 was deposited by spin coating TiO_2 paste (GreatCellSolar, 30NR-D) diluted in ethanol (1:6.3 by mass fraction) at 5000 rpm for 20 s followed by heating at 125 °C for 10 min and sintering at 500 °C for 20 min. A thin layer of passivating tin oxide of ~20 nm was spin-coated by using tin (IV) chloride (Acros) solution (12 μL diluted in 988 μL water) at 3000 rpm for 30 s, followed by annealing at 100 °C for 10 min and 190 °C for 1 h. The prepared substrates were treated with UV- ozone for 15 min before perovskite deposition. A 1.3M $[(FAPbI3)_{0.87}(MAPbBr3)_{0.13}]_{0.92}(CsPbI3)_{0.08}$ perovskite solution with excess PbI2 (PbI2:FAI = 1.05:1) was prepared by mixing FAI (GreatCellSolar), MABr (GreatCellSolar), CsI (ABCR), PbI_2 (TCI), and $PbBr_2$ (TCI) in DMF and DMSO (0.78:0.22 v/v). The prepared perovskite precursor was then spin-coated on the prepared 2 substrates at 2000 rpm for 12 s and 5000 rpm for 30 s. Chlorobenzene was added as an anti-solvent at 15 s before the end of spin coating process. The films were subsequently annealed at 100 °C for 60 min. After cooling down to room temperature, a 100μL solution of the synthesized 2-TMAI or PEAI (GreatCellSolar) in 2-propanol (60 mM) was spin-coated dynamically by adding the solution during spinning at 4000 rpm for 30 s, followed by annealing at 100 °C for 6 min in order to form a 60 nm thick of 2D perovskite layer on top. For a complete device, a spiro OMeTAD layer as the hole-transporting materials (HTM) was deposited on top of the perovskite layer. 78.2 mg of spiro-OMeTAD (Merck) was dissolved in 1 mL chlorobenzene and doped with 31.28 μL of 4-tert- butylpyridine (Sigma-Aldrich), 18.57 μL of Li-bis (trifluoromethanesulphonyl) imide (Aldrich) from the stock solution (196 mg in 379 μL acetonitrile), 13.69 μL of FK 209 Co(III) TFSI (GreatCellSolar) from the stock solution (99 mg in 263 μL acetonitrile). The prepared spiro- OMeTAD solution was then spin-coated at 4000 rpm for 30 s. Finally, a 70 nm-thick gold counter electrode was thermally evaporated on top of HTM layer.

Photoluminescence and UV-Vis Absorption Photoluminescence spectra of the perovskite films were measured and recorded using Fluorolog3-22 spectrofluorometer. The emission was measured upon excitation at 450 nm. The absorption spectra of the perovskite thin films were measured in an ultraviolet, visible, near- infrared spectrophotometer (PerkinElmer Lambda 950S).

Time-resolved Photoluminesncence Time-resolved photoluminescence (TrPL) decays were acquired on a time-correlated single- photon counting (TCSPC) FL900 spectrometer from Edinburgh Analytical Instruments with a Hamamatsu MCP-PMT R3809U-50, and a PicoQuant LHD-DC-440 pulsed laser diode at lexc = 440 nm (pulsewidth < 80 ps; F = 9.7 nJ cm^{-2}). The instrument response was recorded using Ludox samples. At least 1,000 counts in the peak channel were accumulated for the lifetime determination. The emission decays were analyzed using exponential functions.

S4.3.2 Supplementary figures
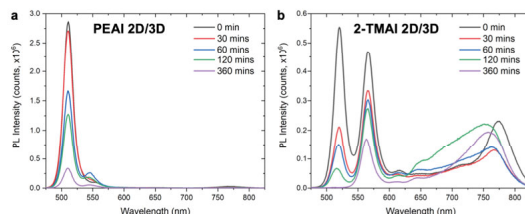
Figure S4.3-3: PL spectra (not normalized) of (a) PEAI 2D/3D and (b) 2-TMAI 2D/3D under thermal aging upon excitation at 450 nm from the front side
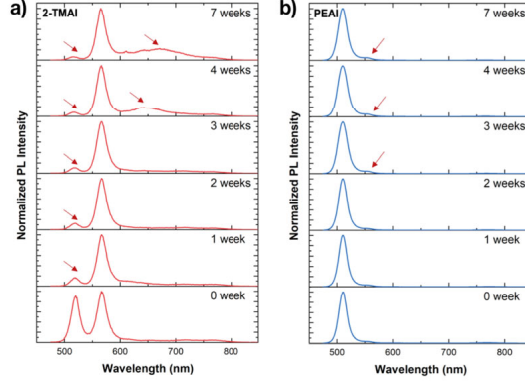
Figure S4.3-4: PL spectra of 2D/3D perovskite films employing (a) 2-TMAI and (b) PEAI as the large cation upon slow aging in dark and dry environment at room temperature.
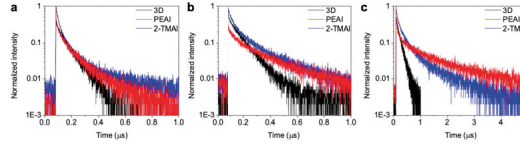
Figure S4.3-5: Normalized TrPL decays ($\lambda_{exc} = 440$ nm; $\lambda_{pl} = 780$ nm) of the 3D control sample (black curves), PEAI (red curves), and 2-TMAI (blue curves) 2D/3D modified perovskite thin films as function of the heat time at T = 50 °C: t= 0 (a), t=15 (b), and t=30 min (c).

S5.1 Exploratory study on the origin of long living photo-excitations in single flakes of MoS$_2$

S5.1.1 Methods

The laser source employed for our experiments setup was an amplified Ti:sapphire laser (Libra from Coherent), with maximum output energy of about 1mJ, 2 kHz repetition rate, central wavelength of 800 nm and pulse duration of about 100-fs. The beam was initially divided into two parts through a Beam Splitter (BS) in order to generate the pair of required pulses. One part was used for generating the excitation (pump) pulses at 400 nm, by frequency doubling in a β-barium borate crystal. Pump pulses were modulated by a mechanical chopper at 1 kHz repetition rate and were delayed in time by means

of a mechanical stage. The pump was focused on a 250 μm diameter spot and the exploited fluence was of 35μJ/cm2. The other part of the beam was used to generate the probe pulses by the white light continuum generation process, by focusing the 800 nm beam into a thin sapphire plate, spanning from 430nm to 770nm as detection range. This configuration was used to perform measurements in the time range between 1ps and 1.5ns. In order to be able to detect signals at longer time delays another approach was used. The laser source employed for generating the pump pulses was a Q-switched Nd:YVO4 laser (Innolas Picolo), with central wavelenght at 1065 nm and pulse duration of 500 ps with externally triggerable repetition rate. It was electronically triggered at 1kHz and synchronised with respect to the femtosecond laser via an electronic delay. Therefore the third harmonic at 355nm was focused on a 300 μm diameter spot and used as pump for delays between 1ns and 100 μs. The pump power of the picosecond laser was adjusted in order to overlap the signal of the femtosecond laser in the range 1-1.5ns and therefore the data taken in the two time regimes were combined together at around 1ns (eventually with the application of a small scaling factor). The probe pulse was focused on the sample non-collinearly with the pump beam and the spectrum of the transmitted probe beam was measured by a high-speed spectrometer (Entwicklungsbuero EB Stresing) working at the full 2kHz laser repetition rate. Thanks to the modulation (mechanical or electronical) of the pump pulse, two consecutive probe pulses are measuring the sample in the excited and in the ground state. By measuring their corresponding intensities (Ion and Ioff) one can calculate the normalized transmission change: δT/T = (Ion/Ioff)-1, both as a function of wavelength (spectrometer detection) and time delay (mechanical/electronical delay). Chirp-free transient absorption spectra were collected by using a dechirping algorithm
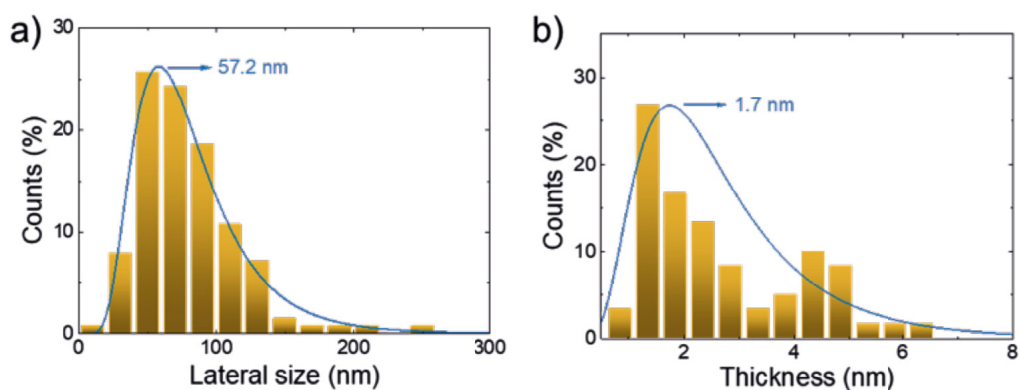
Table S5.1-1: Statistical analyses of a) the lateral size and b) the thickness of the LPE-produced MoS2 nanoflakes.

S6.1 Data Analysis Scripts

S6.1.1 Global anaylsis

```python
#!/usr/bin/env python3
# -*- coding: utf-8 -*-
"""
Global fitting MoS2
"""
###################
#     Header      #
###################

import pandas as pd
import matplotlib.pyplot as plt
import matplotlib.cm as cm
import matplotlib
```

```python
import numpy as np
from scipy import interpolate
from scipy.optimize import curve_fit
from scipy.signal import savgol_filter
from bokeh.plotting import figure, output_file, show
from bokeh.models import ColumnDataSource, Range1d, Span, Button,
    TextInput, Legend, Select, CustomJS, Column, Toggle, Div,
    TextInput, Slider, LinearColorMapper, LogTicker, ColorBar,
    Range1d
from bokeh.io import push_notebook, show, output_notebook, curdoc
from bokeh.layouts import gridplot, row, column, layout
from bokeh.palettes import all_palettes, Viridis5, Viridis3,
    Viridis4
from bokeh import events
import bokeh.palettes as palettes
from bokeh.client import push_session, pull_session
import pandas_bokeh
#pandas_bokeh.output_notebook()
#pd.set_option('plotting.backend', 'pandas_bokeh')
#output_notebook()
from astropy import modeling
output_file("foo.html")
from astropy.modeling.models import custom_model
np.seterr(all='ignore')


#%%
```

```python
################################
#      Usefull functions       #
################################


def find_col(data, values):
    '''return the column of the value '''
    array = np.asarray(data.columns).astype('float')
    col=[]
    for value in values:
        idx=((np.abs(array - value)).argmin())
        col.append(data.iloc[:,idx].name)
    return col




def norm(data, mode='max'):
    '''return the normalized matrix '''
    # if mode =/= max, normalized at seleted time
    data1 = data.copy()
    for col in data1:
        if data1[col].max() > np.abs(data1[col].min()):
            if mode == 'time':
                data1[col]= data1[col]/ data1.iloc[50][col]
            else:
                data1[col]= data1[col]/ data1[col].max()
        else:
            if mode =='time':
                data1[col]= data1[col]/ data1.iloc[50][col]
            else:
```

```python
        data1[col]= data1[col]/ data1[col].min()
    return data1



def plotting(source,data,title='test',x_type='log',xrange
    =(0.1,100000000)):
    '''usefull plotting function for interfacing with Bokeh '''
    fig = figure(title=title,x_axis_label='wavelength (nm)',
        y_axis_label='DT/T (%)',x_axis_type=x_type, plot_width
        =600, plot_height=400,margin = (0,0,0,0),tools="pan,save,
        box_zoom,wheel_zoom,reset")
    for col,color in zip(data,palettes.viridis(data.shape[1])):
        if data.index.name == None:
            index = 'index'
        else:
            index = data.index.name
        if type(col) is not str:
            col = str(col)
        fig.line(index,col,source = source,name=col,legend_label
            =str(round(float(col),1))+'ps', line_width=3,color=
            color)
    fig.x_range=Range1d(xrange[0],xrange[1])

    hline_y = Span(location=0, dimension='width', line_color
        ='black', line_width=1,name='span_y',level='underlay'
        )
    fig.renderers.extend([hline_y])
    fig.legend.visible=True
```

```python
    return fig


palette = [matplotlib.colors.to_hex(x) for x in matplotlib.cm.
    bwr(np.arange(256) / 255)]


def color_map(data1,min_time=0.1,min_nm=450,div_palette=palette,
    title='MoS2'):
    '''plot a colormap of the TA data '''

    f_interp = interpolate.interp2d(data1.columns,data1.index,
        data1.values, kind='linear')
    new_x=np.logspace(np.log10(min_time),np.log10(data1.columns.
        max()),1000).round(3)#min_time # nm
    new_y=np.linspace(min_nm,data1.index.max(),500).round(1) #
        nm
    new_data1 = pd.DataFrame(f_interp(new_x,new_y), columns=
        new_x,index=new_y)

    p = figure(title=title,x_axis_label='wavelength (nm)',
        y_axis_type='log',y_axis_label='time (ps)',plot_width
        =500, plot_height=500)#y_axis_type='log'
    p.x_range.range_padding = p.y_range.range_padding = 0

    max_value = new_data1.values.max()
    source_image=ColumnDataSource(data=dict(image=[new_data1.T.
        values]))
```

```python
color_mapper = LinearColorMapper(palette=div_palette, low=-
    max_value, high=max_value)


p.image('image',source=source_image,x=min_nm,y=min_time, dh
    =10**8-min_time, dw=355, color_mapper=color_mapper, level
    ="image")
p.grid.grid_line_width = 0.1
p.y_range=Range1d(min_time,10000000)
#p_mos2_4.y_range.flipped = True
color_bar = ColorBar(color_mapper=color_mapper,
    label_standoff=12, border_line_color=None,title='DT/T_%',
    location=(0,0), orientation="horizontal")
p.add_layout(color_bar, 'below')
show(p)




def plot_nm(nm=20,power=30,results=results,model=model5,x=x):
    '''plot decay with the fit, usefull to check the result of
        the global fit '''
    plt.semilogx(data[power].T[results.index[nm]],'.k',label=
        round(results.index[nm],0))
    model5.parameters=results.T[results.index[nm]].values
    plt.semilogx(x,model(x),label='fit')
    plt.hlines(y=0,xmin=0.1,xmax=10e8)
    results.index[power]
    plt.legend()


#%%
```

```python
##########################################
#      Data import and fromating     #
##########################################

d_mos2_4 = pd.read_csv('/Users/Valentin/Dropbox/MoS2-Perov/
    DataJoint/d200715_11_10.dat', delimiter='  ', engine='python'
    )
d_mos2_13 = pd.read_csv('/Users/Valentin/Dropbox/MoS2-Perov/
    DataJoint/d200715_07_08.dat', delimiter='  ', engine='python'
    )
d_mos2_30 = pd.read_csv('/Users/Valentin/Dropbox/MoS2-Perov/
    DataJoint/d200715_12_09.dat', delimiter='  ', engine='python'
    )
d_mos2_90 = pd.read_csv('/Users/Valentin/Dropbox/MoS2-Perov/
    DataJoint/d200709_01_02.dat', delimiter='  ', engine='python'
    )


data={} # assambling the multiple dataset in 1 big
    multidimentional set
data[4]=d_mos2_4
data[13]=d_mos2_13
data[30]-d_mos2_30
data[90]=d_mos2_90


power =[4,13,30,90]


for power in data: # renaming the index and smoothing the data
```

```python
    data[power].columns = data[power].columns.astype('float')
    name2 = [col for col in data[power].columns]
    name2[0]= 'nm'
    data[power].columns = name2
    data[power].set_index(['nm'], inplace = True)
    data[power]=data[power].T.apply(savgol_filter, axis = 0,
        args = (11,1))
    data[power]=data[power].T



sources={}
sources_decay={}


for power in data: # preparing the data for plotting
    data[power].columns=data[power].columns.astype('str')
    data[power].index=data[power].index.astype('float')
    sources[power]= ColumnDataSource(data[power])

    data[power].index=data[power].index.astype('str')
    data[power].columns=data[power].columns.astype('float')
    sources_decay[power]= ColumnDataSource(data[power].T)
    data[power].index=data[power].index.astype('float')


#%%
#########################################
#    previsualisation of the data    #
#########################################
```

```
times=[0.1,0.2,0.3,0.5,1,2,5,7,20,100,500,1000]
p=13
list_time=find_col(data[p],times)


nm = [610,620,645,680]
list_nm=find_col(data[p].T,nm)


t = plotting(sources[p],data[p][list_time],xrange=(550,800))


r = plotting(sources_decay[p],data[p].T[list_nm])


show(column(t,r))


#%%
############################
#     model for the fit    #
############################



@custom_model
def sum_of_exp(x, a1=-1., a2=-1., a3=1., t1=1., t2=100., t3
    -10000.,x0-0.):
    return(a1*np.exp(-x/t1) + a2*np.exp(-x/t2) + a2*np.exp(-x/t3
        ))


@custom_model
```

185

```
times=[0.1,0.2,0.3,0.5,1,2,5,7,20,100,500,1000]
p=13
list_time=find_col(data[p],times)


nm = [610,620,645,680]
list_nm=find_col(data[p].T,nm)


t = plotting(sources[p],data[p][list_time],xrange=(550,800))


r = plotting(sources_decay[p],data[p].T[list_nm])


show(column(t,r))


#%%
############################
#     model for the fit    #
############################



@custom_model
def sum_of_exp(x, a1=-1., a2=-1., a3=1., t1=1., t2=100., t3
    -10000.,x0-0.):
    return(a1*np.exp(-x/t1) + a2*np.exp(-x/t2) + a2*np.exp(-x/t3
        ))


@custom_model
```

```python
def model_exp(x, a1=-1.,t1=1.,x0=0.):
    return(a1*np.exp((x0-x)/t1))



fitter = modeling.fitting.LevMarLSQFitter() # initialize fitting
    algo


#%%
#############################
#     first model: 1exp     #
#############################


# initialization of the model
model = sum_of_exp(a1=0.0001,a2=0.001,a3=0.001,t1=0.1,t2=1,t3
    =100,x0=0)


g=4
x=data[g].columns.values[50:] # definition of the X axis


# definition of model to fit with the data used
fitted_model = fitter(model, x, data[4].iloc[250,50:].values,
    maxiter=1000)


print(fitted_model.parameters)


#%%
##################################
#     2nd model: sum of 4 exp     #
```

```python
#######################################

t=30 # time selection
g=30 # power selction
x=data[g].columns.values[t:]


model1= model_exp(a1=+0.302,t1=0.841,x0=0)
model2= model_exp(a1=-0.031,t1=261.057,x0=0)
model3= model_exp(a1=-0.030,t1=6987.210,x0=0)
model4= model_exp(a1=-0.006,t1=383407.727,x0=0)



model1.x0.fixed=True
def tied_x0(model):
    return model.x0_0


model2.x0.tied=tied_x0
model3.x0.tied=tied_x0
model4.x0.tied=tied_x0


model1.t1.bounds=(0.5,1)
model2.t1.bounds=(200,270)
model3.t1.bounds=(1000,10000)
model4.t1.bounds=(200000,500000)



model1.a1.bounds=(-2,2)
model2.a1.bounds=(-1,1)
```

```
model3.a1.bounds=(-1,1)
model4.a1.bounds=(-1,1)


model5 = model1+model2+model3+model4


nm=200
fitted_model = fitter(model5, x, data[g].iloc[nm,t:].values,
    maxiter=2000)



#%%


######################################
#      visualization of the fit      #
######################################


model1.parameters=fitted_model.parameters[0:3]
model2.parameters=fitted_model.parameters[3:6]
model3.parameters=fitted_model.parameters[6:9]
model4.parameters=fitted_model.parameters[9:12]

#g=4
ax=plt.figure(figsize=(12, 4))
plt.plot(x,data[g].iloc[nm,t:])
#plt.semilogx(x,model1(x),label='1')
#plt.semilogx(x,model2(x),label='2')
#plt.semilogx(x,model3(x),label='3')
#plt.semilogx(x,model4(x),label='4')
```

```python
plt.semilogx(x,fitted_model(x),label='fit')
plt.legend()
#plt.xlim(100,10000000)
#plt.ylim(-0.03,0.01)
plt.hlines(y=0,xmin=0,xmax=10e8)
plt.show()
print('a1:_{:.3f},_t1:_{:.3f},_x0:_{:.3f}\n\
a2:_{:.3f},_t2:_{:.3f},_x0:_{:.3f}\n\
a3:_{:.3f},_t3:_{:.3f},_x0:_{:.3f}\n\
a4:_{:.3f}_t4:_{:.3f},_x0:_{:.3f}\n'.format(*fitted_model.
    parameters))


#%%
############################################################
#     fit the best model for all wavelength    #
############################################################
t=30


x=data[g].columns.values[t:]
results=pd.DataFrame(columns=['a1','t1','x0_1','a2','t2','x0_2',
    'a3','t3','x0_3','a4','t4','x0_4'])
for i,curve in enumerate(data[g].T):
    #if i>0:
    #     model5.parameters=fitied_model.parameters

    fitted_model = fitter(model5, x, data[g].T[curve].iloc[t:].
        values,maxiter=1000)
    results.loc[curve]=fitted_model.parameters
```

```python
#%%
###############################################
#     vusualisation  if  the  goba  results  #
###############################################


#results = pd.read_csv('fit_4uW.txt')
#results.set_index(['Unnamed: 0'], inplace=True)
#results.index.name='nm'

plt.plot(results.a1,label='0.3ps')
plt.plot(results.a2,label='168ps')
plt.plot(results.a3,label='3ns')
plt.plot(results.a4,label='209ns')

plt.hlines(y=0,xmin=450,xmax=800)
plt.legend(title='tau_4uw')
```

S6.1.2   TA Visualisation dashboard

```python
import pandas as pd
import matplotlib.pyplot as plt
import matplotlib.cm as cm
import numpy as np
from scipy import interpolate
from scipy.signal import savgol_filter
from bokeh.plotting import figure, output_file, show
from bokeh.models import ColumnDataSource, Range1d,Span,Button,
```

```python
        TextInput, Legend, Select, CustomJS, Column, Toggle, Div,
        TextInput, Slider, LinearColorMapper, LogTicker, ColorBar,
        Range1d
from bokeh.io import push_notebook, show, output_notebook, curdoc
from bokeh.layouts import gridplot, row
from bokeh.palettes import all_palettes, Viridis5, Viridis3
from bokeh import events
from bokeh.client import push_session, pull_session


energies = np.array([80,150,250,400,650])
all_data={}

for value in energies:
    name = 'pea_'+str(value)+'nj.txt'
    data = pd.read_csv(name)
    data.set_index(['time_ps'], inplace=True)
    data.columns = data.columns.values.astype(float)
    data.index.name=None
    all_data[value]=data


# usefull variable
y_min = all_data[80].index.min()
y_max = all_data[80].index.max()
new_y =all_data[80].index.values
x_min = all_data[80].columns.min()
x_max = all_data[80].columns.max()
```

```python
new_x = all_data[80].columns.values
amplitude_min = all_data[650].values.min()
amplitude_max = all_data[650].values.max()


# Top figure
p_top = figure(title='decay',x_axis_label='time_(ps)',
    y_axis_label='DA',x_axis_type='log',plot_width=500,
    plot_height=250,tools="pan,save,wheel_zoom,reset")
p_top.x_range.range_padding = p_top.y_range.range_padding = 0
p_top.y_range = Range1d(amplitude_min,amplitude_max)
p_top.x_range = Range1d(y_min,y_max)


source_top = ColumnDataSource(data=dict(x=new_y, y=all_data
    [650].iloc[:,100]))
top_line = p_top.line('x', 'y',source=source_top,color='red')
hline = Span(location=0, dimension='width', line_color='black',
    line_width=1)
p_top.renderers.extend([hline])


# central figure
p_center= figure(title='map',x_axis_label='wavelength_(nm)',
    y_axis_label='time_(ps)',y_axis_type='log',plot_width=500,
    plot_height=500,tools="pan,save,wheel_zoom,reset")
p_center.x_range.range_padding = p_center.y_range.range_padding
    = 0


source_image=ColumnDataSource(data=dict(image=[all_data[650].
    values]))
```

```python
p_center.image('image',source=source_image,x=x_min,y=y_min, dh=
    y_max-y_min, dw=x_max-x_min, palette = "Viridis256", level="
    image")
p_center.grid.grid_line_width = 0.1
    # color bar
color_mapper = LinearColorMapper(palette="Viridis256", low=
    amplitude_min, high=amplitude_max)
color_bar = ColorBar(color_mapper=color_mapper,label_standoff
    =12, border_line_color=None, location=(0,0), orientation="
    horizontal")


hline_y = Span(location=0, dimension='width', line_color='white'
    , line_width=1,name='span_y')
hline_x = Span(location=0, dimension='height', line_color='white
    ', line_width=1,name='span_x')


p_center.renderers.extend([hline_y,hline_x])
p_center.add_layout(color_bar, 'below')


# righ figure
p_right= figure(title='specra',x_axis_label='nm',y_axis_label='
    DA',plot_width=500, plot_height=500,margin = (0,0,0,0),tools=
    "pan,save,wheel_zoom,reset")
p_right.x_range.range_padding = p_right.y_range.range_padding =
    0


source_right = ColumnDataSource(data=dict(x=new_x, y=all_data
    [650].iloc[100,:]))
```

```python
p_right.line('x', 'y',source = source_right,color='red')
p_right.y_range = Range1d(amplitude_min,amplitude_max)
p_right.renderers.extend([hline])


# power dependent nm
#list_nm = [495,510,524]
def p_dep(list_nm=[495,510,524]):
    power_dep = pd.DataFrame(index=energies,columns=list_nm)
    for nm in list_nm:
        max_point=[]
        for data in all_data:
            max_point.append(all_data[data].iloc[np.searchsorted
                (new_y, 0.4, side='right'),

                                                np.searchsorted
                                                (new_x, nm,
                                                side='right'
                                                )])
        power_dep[nm]=max_point
        power_dep.columns=power_dep.columns.astype(str)
    return power_dep


power_dep=p_dep()
#power_dep.columns=power_dep.columns.astype(str)
source_power = ColumnDataSource(power_dep)


p_power = figure(title='power_dependence',x_axis_label='
    excitation_energy_(nj)',y_axis_label='DA',plot_width=500,
    plot_height=500,tools="pan,save,wheel_zoom,reset")
```

```python
p_power.renderers.extend([hline])
for value in power_dep.columns.astype(str):
    p_power.line(x='index',y=value,source=source_power)


# slider and buttons

nm = Slider(title="nm", value=x_min, start=int(x_min), end=int(
    x_max), step=1,width = 445,margin = (0,0,0,60))
time = Slider(title="time_10^", value=np.log10(y_min),
                start=np.log10(y_min), end=np.log10(y_max),
                step=0.01,height = 380,margin = (10,0,0,0),
                    orientation='vertical',direction='rtl')
#

selected_nm=TextInput(value='495,510,524',title='selected_nm')
show_all_power = Toggle(label='show_all_power')


nm_int=np.array(str.split(selected_nm.value,',')).astype(int)


def legend_plot(fig,label):
    legend_label=[]
    for r,label in zip(fig.renderers[1:],label):
        legend_label.append((label+'nm',[r]))
    return legend_label


legend = Legend(items=legend_plot(p_power,nm_int.astype(str)))
#p_power.add_layout(legend, 'right')
```

```python
energies_str=energies.astype(str).tolist()
power_choice = Select(title="excitation_power_:", value=
    energies_str[0],options=energies_str)
plot_power=Button(label='plot_power_dep')


widget = Column(power_choice,show_all_power,selected_nm,
    plot_power)

# callback function for interactivity

def callback_nm(attr, old, new):
    source_top.data = dict(x=new_y,
                                 y=all_data[int(power_choice.value)].
                                     iloc[:,np.searchsorted(new_x, nm.
                                     value, side='right')])
    p_top.title.text = str(round(nm.value,0))
    p_center.select(name='span_x').location=nm.value


def callback_time(attr, old, new):
    source_right.data = dict(x=new_x, y=all_data[int(
        power_choice.value)].iloc[np.searchsorted(new_y, 10**time
        .value, side='right') ,:])
    p_right.title.text = str(round(time.value,0))
    p_center.select(name='span_y').location=10**time.value


def callback(event):
    p_center.title.text = str(round(event.x,2))+'-'+str(round(
        event.y,2))
```

```python
        nm.value=event.x
        time.value=np.log10(event.y)
        p_center.select(name='span_x').location=event.x
        p_center.select(name='span_y').location=event.y



def callback_power(attr, old, new):
    amplitude_min = all_data[int(power_choice.value)].values.min
        ()
    amplitude_max = all_data[int(power_choice.value)].values.max
        ()
    source_image.data=dict(image=[all_data[int(power_choice.
        value)].values])
    #p_center.image(image=[all_data[int(power_choice.value)].
        values],x=x_min,y=y_min, dh=y_max-y_min, dw=x_max-x_min,
        palette = "Viridis256", level="image")
    p_right.y_range.end = p_top.y_range.end = amplitude_max
    p_right.y_range.start = p_top.y_range.start = amplitude_min


def callback_all_power(event):
    #p_top.title.text = str(show_all_power.active)
    if show_all_power.active:
        p_top.title.text = str(show_all_power.active)
        for value,color in zip(energies,Viridis5):
            source_top_all = ColumnDataSource(dict(x=new_y,
                        y=all_data[value].iloc[:,np.
                            searchsorted(new_x, nm.value, side
                            ='right')]))
```

```python
        p_top.line('x', 'y',source=source_top_all,color=
            color)


        source_right_all = ColumnDataSource(data= dict(x=
            new_x, y=all_data[value].iloc[np.searchsorted(
            new_y, 10**time.value, side='right'),:]))
        p_right.line('x', 'y',source = source_right_all,
            color=color)


    p_top.y_range.end=p_right.y_range.end = all_data[
        energies.max()].values.max()


    else:
        p_top.renderers=[p_top.renderers[0],p_top.renderers[1]]
        p_right.renderers=[p_right.renderers[0],p_right.
            renderers[1]]
        p_top.y_range.end =p_right.y_range.end= all_data[int(
            power_choice.value)].values.max()


def callback_plot(event):
    if p_power.right != []:
        p_power.right=[]

    nm_int=np.array(str.split(selected_nm.value,',')).astype(int
        )
    power_dep=p_dep(nm_int)
    source_power = {'index': power_dep.index.astype(int).to_list
        ()}
```

```python
        source_power.update(power_dep.to_dict(orient='list'))


        p_power.renderers=[p_power.renderers[0]]
        for value,color in zip(power_dep.columns.astype(str),
            Viridis3):
            p_power.line(x='index',y=value,source=source_power,color
                =color)


        legend = Legend(items=legend_plot(p_power,nm_int.astype(str)
            ))
        #p_power.add_layout(legend, 'right')




# event activation
nm.on_change('value', callback_nm)
time.on_change('value', callback_time)
p_center.on_event(events.Tap,callback)
power_choice.on_change('value',callback_power,callback_nm,
    callback_time)
show_all_power.on_click(callback_all_power)
plot_power.on_click(callback_plot)



# layout config
layout = gridplot([[p_top,None,widget],[nm],[p_center,time,
    p_right],[p_power]])
```

```
curdoc().add_root(layout)
```

CHAPTER 11

Curriculum Vitae

vqueloz@bluewin.ch

Valentin **Queloz**

ABOUT ME

Chim. Dipl. EPF, I am currently finishing a PhD in new solar energy materials. My interests revole around chemistry, data analysis, processes optimization, optical instrumentation and new technologies. Through my experiences, I am a quick learner, proficient in analytical work with attention to details and clear communication within an international environement.

PERSONAL

Date of birth	07. May 1993 (27y.o.)
Adresse	4, chemin du sequoia, 1224 Chêne-Bougeries, Switzerland
Phone/email/Socials	+41 78 644 67 11 – vqueloz@bluewin.ch – Skype – Linkedin
Languages	**French:** Mother tongue, **English:** C1, **German:** B1, **Russian:** A1

EXPERIENCES

2019-present

R&D consultant – General Microtechnology and photonic S.A, Switzerland
+ Carried a feasibility study for a cost effective and miniaturized optical instrument.
+ Prototyping said instrument and producing technical documentation.

2017-present

PhD in Chemistry and chemical engineering – EPFL, Switzerland
+ Ultrafast Spectroscopy on new generation solar cell materials, resulting in 18+ papers
+ Streamlined data gathering reducing experimental time by 80% and automated data analysis workflow through Python scripts.
+ Developed visualisation tools and dashboards to enable the analysis of multiple datasets at once thus allowing inter-dataset comparison and modelling.
+ Led scientific projects with international teams of 10+ collaborators.
+ Contact persone for equipment supplyer
+ Development of new optical intruments.
+ Optical Lab manager.
+ Delivered 5+ scientific talks and posters at major international conferences with a diverse audience.

2015-2019

Science communicator – Scientastic, EPFL, Switzerland
+ Communicated complex scientific information to non-scientific audiences in a creative and engaging way.
+ Drove lab presentation tour and run a solar cell demonstrator to inspire children and families about solar energies.

2014-present

Teaching Assistant – EPFL, Switzerland
+ Lead teaching session/labwork with 4 up to 150 students.

2012

Internship – TH_NK digital, London
+ Optimized multi-dataset ingestion with excel macros for the back end of the pottermore.com website (now wizardingworld.com)

STUDIES

2017 – present

PhD in Chemistry and chemical engineering – EPFL, Switzerland
+ **Thesis:** Photoinduced processes in hybrid perovskite for optoelectronics
  o **Directors:** Prof. M.K. Nazeeruddin & Prof. G. Grancini

2015 - 2017

MSc in Molecular & Biological Chemistry – EPFL, Switzerland
+ **Thesis:** Dynamic of photocarriers in lead halide perovskite
  o **Supervisor:** Prof. Jacques Moser
+ **Minor:** Management of Technology & Entrepreneurship

vqueloz@bluewin.ch

2012 - 2015	**BSc in Chemistry & Chemical Engineering**– EPFL, Switzerland

+ **Thesis:** Electrodeposition & Nano-structuration of $CuWO_4$ has a photoanode for the oxygen evolution reaction
  o **Supervisor:** Prof. Xile Hu

2008 - 2012 **MATURITÉ** – CEC Andrée-Chavanne, Geneva – Switzerland

+ **Option:** Math-Physics

SKILLS

IT **Python, Jupyter, Excel, Collaboration tools (GitHub, G suits), SQL, GUI automation, OriginLab, Matlab, LaTex, Unix, Adobe Photoshop & Illustrator.**

Optics **Ultrafast spectroscopy, Pulsed & CW Laser, TCSPC, Absorption, QY, Photo-luminescence.**

OTHERS

Personal Interests **Rock climbing, Ski, Musician, Cooking**

Volunteering **Certified coach for undergrads, Chemistry Student Society**

SELECTED PUBLICATIONS

1. Queloz, V.I.E et al. Spatial Charge Separation as the Origin of Anomalous Stark Effect in Fluorous 2D Hybrid Perovskites. Adv. Func. Mat. (2020).

2. García-Benito, I. et al. Fluorination of Organic Spacer Impacts on the Structural and Optical Response of 2D Perovskites. Front. Chem. (2020). doi:10.3389/fchem.2019.00946

3. Chiara, R. et al. Green-Emitting Lead-Free Cs4SnBr6 Zero-Dimensional Perovskite Nanocrystals with Improved Air Stability. J. Phys. Chem. Lett. 11, 618–623 (2020).

4. Sutanto, A. A. et al. Dynamical evolution of the 2D/3D interface: A hidden driver behind perovskite solar cell instability. J. Mater. Chem. A 8, 2343–2348 (2020).

5. Pisanu, A. et al. Exploring the role of halide mixing in lead-free BZA2SnX4 two dimensional hybrid perovskites. J. Mater. Chem. A 8, 1875–1886 (2020).

6. Kanda, H. et al. Band-bending induced passivation: high performance and stable perovskite solar cells using a perhydropoly(silazane) precursor. Energy Environ. Sci. (2020). doi:10.1039/c9ee02028d

7. Cho, K. T. et al. Perovskite Solar Cells: 18% Efficiency Using Zn(II) and Cu(II) Octakis(diarylamine)phthalocyanines as Hole-Transporting Materials. ACS Appl. Energy Mater. (2019). doi:10.1021/acsaem.9b00637

8. Pantaler, M. et al. Hysteresis-Free Lead-Free Double-Perovskite Solar Cells by Interface Engineering. ACS Energy Lett. 3, 1781–1786 (2018).

9. Tirado, J. et al. Copper sulfide nanoparticles as hole-transporting-material in a fully-inorganic blocking layers n-i-p perovskite solar cells: Application and working insights. Appl. Surf. Sci. (2019). doi:10.1016/j.apsusc.2019.01.289

10. Bouduban, M. E. F. et al. Crystal Orientation Drives the Interface Physics at Two/Three-Dimensional Hybrid Perovskites. J. Phys. Chem. Lett. 5713–5720 (2019). doi:10.1021/acs.jpclett.9b02224

11. García-Benito, I. et al. Fashioning Fluorous Organic Spacers for Tunable and Stable Layered Hybrid Perovskites. Chem. Mater. 30, 8211–8220 (2018).